AFRL-SR-BL-TR-02-

0738

REPORT DOCUMENTATION PAGE

1. AGENCY USE ONLY *(Leave blank)*	2. REPORT DATE January 31, 2002	3. REPORT TYPE AND DATES COVERED Final Report 5/1/98-9/30/01	

4. TITLE AND SUBTITLE EXPERIMENTAL STUDIES OF SHOCK INTERACTION PHENOMENA ASSOCIATED WITH HYPERSONIC AIRBREATHING PROPULSION	5. FUNDING NUMBERS G – F49620-98-1-0445
6.AUTHORS Michael S. Holden, Timothy P. Wadhams, Gregory J. Smolinski, Ronald A. Parker, John K. Harvey	

7.PERFORMING ORGANIZATION NAME(S) AND ADDRESS(ES) Aerothermal Aero-optic Evaluation Center Calspan-UB Research Center 4455 Genesee Street Buffalo, NY 14225	8. PERFORMING ORGANIZATION REPORT NUMBER 3640-1

9. SPONSORING/MONITORING AGENCY NAME(S) AND ADDRESS(ES) Air Force Office of Scientific Research 801 N. Randolph Street, Room 732 Arlington, VA 22203-1977	10. SPONSORING/MONITORING AGENCY REPORT NUMBER

11. SUPPLEMENTARY NOTES

AIR FOR~
NOTIC~
HAS b~
LAW AF~

12a. DISTRIBUTION/AVAILABILITY STATEMENT UNLIMITED **DISTRIBUTION STATEMENT A** Approved for Public Release Distribution Unlimited	**20020419 168**

13. ABSTRACT *(Maximum 200 words)*

Experimental studies were conducted in conjunction with computations in a code validation exercise to examine the ability of DSMC and Navier-Stokes techniques to predict the complex characteristics of regions of shock/shock and shock/boundary layer interactions in hypervelocity flows. In the experimental program, detailed heat transfer and pressure measurements in laminar regions of shock wave/boundary layer interaction, and shock/shock interaction, over hollow cylinder/flare and double cone configurations in hypersonic flow. In the best Navier-Stokes solutions the structure and density of the flowfield was captured exactly over both the hollow cylinder/flare and double cone models. The detailed characteristics of the distribution of pressure and heating through the interaction regions were well predicted. In general, for these relatively high-density flows, the DSMC solutions did not capture the characteristics of well-separated flows. In Part 2 of this program, experimental studies have been conducted in the LENS I shock tunnel to investigate the characteristics and performance of full-scale scramjet engines at fully duplicated flight conditions for a range of dynamic pressures at Mach 7. In this program we obtained detailed heat transfer and pressure measurements together with high speed Schlieren and infrared imagery to determine the characteristics of a generic engine, the flow path of which was configured to be similar to the Air Force Hy-Tech configuration for studies with hydrocarbon and hydrogen fuels.

14. SUBJECT TERMS CFD code validation; laminar shock boundary layer interaction; shock/shock interaction; heat transfer and pressure measurements; flowfield characteristics; scramjet engine	15. NUMBER OF PAGES 80
	16. PRICE CODE

17. SECURITY CLASSIFICATION OF REPORT UNCLASSIFIED	18. SECURITY CLASSIFICATION OF THIS PAGE UNCLASSIFIED	19. SECURITY CLASSIFICATION OF ABSTRACT UNCLASSIFIED	20. LIMITATION OF ABSTRACT UL

Calspan-UB Research Center
4455 Genesee Street
Buffalo, New York 14225

EXPERIMENTAL STUDIES OF SHOCK INTERACTION PHENOMENA ASSOCIATED WITH HYPERSONIC AIRBREATHING PROPULSION

AFOSR Grant No. F49620-98-1-0445

Final Report 3640-1

Prepared by:

Michael S. Holden
Timothy P. Wadhams
Gregory J. Smolinski
Ronald A. Parker
John K. Harvey
Aerothermal Aero-Optic Evaluation Center (AAEC)
Calspan-UB Research Center

EXPERIMENTAL STUDIES OF SHOCK INTERACTION PHENOMENA ASSOCIATED WITH HYPERSONIC AIRBREATHING PROPULSION

AFOSR Grant No. F496020-98-1-0445

Michael S. Holden
Timothy P. Wadhams
Gregory J. Smolinski
Ronald A. Parker
John K. Harvey
Aerothermal Aero-optic Evaluation Center (AAEC)
4455 Genesee Street
Buffalo, NY 14225

Part 1 – Code Validation Studies for Shock/Boundary Layer and Shock/Shock Interaction Regions in Hypervelocity Flows

Abstract

Experimental studies were conducted in conjunction with computations in a code validation exercise to examine the ability of DSMC and Navier-Stokes techniques to predict the complex characteristics of regions of shock/shock and shock/ boundary layer interactions in hypervelocity flows. In the experimental program, detailed heat transfer and pressure measurements were made in laminar regions of shock wave/boundary layer interaction and shock/shock interaction over hollow cylinder/flare and double cone configurations in hypersonic flow. The experimental studies were conducted for a Mach number range from 10 to 12 with Reynolds numbers from 1×10^4 to 5×10^5 and stagnation temperatures from 2,000°R to 5,000°R. Miniature high-frequency thin-film and piezoelectric instrumentation were employed to obtain the high spatial resolution required to accurately define the distribution of heat transfer and pressure in the strong gradients which occur in regions of shear layer reattachment and shock/shock interaction. The program reported here was conducted in two phases. In the first phase of the code validation study, measurements and "blind" computations were made over complete hollow cylinder/flare and double cone configurations in high-temperature flows at Mach 10 and 12 for a range of freestream Reynolds numbers. In the second phase of the program, detailed heat transfer and pressure measurements were made over an extensive range of Reynolds number and total enthalpy conditions using only the hollow cylinder and the 25° conical segment of the models tested earlier in Phase I. The selection of the freestream conditions employed in this second phase of the program was performed in conjunction with computations of the contoured nozzle flows and the flows over the two simple model configurations. Based on the results of the latter studies, we validated the computational schemes used to predict the properties of the freestream developed in the test section of the tunnel. Using these validated calculations, we have re-evaluated the comparisons made earlier between measurements on the double cone and hollow cylinder configurations and the predictions made independently with Navier-Stokes and DSMC predictive schemes. These studies demonstrate that correctly calculating the effects of vibrational nonequilibrium in the freestream properties improve the already excellent agreement between the prediction techniques and experimental data.

Introduction

The increased stability of a laminar boundary layer under hypersonic flow conditions results in a situation where extensive regions of laminar flows will occur over hypersonic re-entry and air-breathing vehicles. Therefore, it is possible to obtain accurate predictions of the laminar aerothermal loads with Navier-Stokes and DSMC calculations. However, these methods must be employed carefully in describing regions of separated flows induced by shock/boundary layer interaction and in the strong gradients generated in regions of shock/shock interaction. Here the accuracy of the predictions can be strongly influenced by the differencing schemes and gridding techniques employed in the computation of regions of strong pressure gradients and recirculating flows. However, to describe such regions in hypervelocity flows, it is necessary to introduce models of the flowfield internal energy exchange and chemistry and the flow surface interaction in regions close to the leading edge. This is true even for nitrogen hypervelocity flows where vibrational nonequilibrium can influence both the properties of the freestream and flow over the model.

During the past decade, there have been significant efforts in Europe and America to validate the prediction techniques employed in the new classes of re-entry and air-breathing vehicles. Extensive code validation activities were conducted in conjunction with European space activities in the 1990s, and similar activities were conducted in the United States, in support of space vehicle design including those developed in the NASP program. A combined American/European code validation exercise was promoted by the NATO Research Technology Organization (RTO) under Working Group 10. Also working with the support of the Air Force Office of Scientific Research (AFOSR), a number of experimental and numerical studies were conducted to examine complex viscous/inviscid interaction regions developed over simple model configurations in laminar hypersonic flows. During these studies, two model configurations – a hollow cylinder flare and a double cone configuration – emerged as simple configurations over which complex interacting flows are developed which can provide a stringent test to the numerical schemes that are employed in the Navier-Stokes and DSMC computations. Early experimental studies using a hollow cylinder/flare configuration were conducted in France by Chanetz et al (Ref. 1), and were compared with extensive series of computations employing Navier-Stokes and DSMC methods. These studies revealed that the extent of the separated region was highly sensitive to grid selection, and discrepancies were also found between the measured and predicted pressure in the interaction regions. Similar comparisons between the computations of Olejnieczak and Candler (Ref. 2) and Gnoffo (Ref. 3) with measurements over a double cone configuration (Holden, Ref. 4) also revealed significant numerical problems can be encountered when predicting the strong gradients generated in regions of shock/shock interaction and boundary layer separations where the differencing schemes can be prone to oscillation and the mesh generation and refinement schemes must be handled with care.

To investigate such problems further, a new set of experimental studies was initiated employing models similar to those used in the hollow cylinder/flare and the double cone experimental studies. The hypersonic low-density conditions were selected to avoid problems associated with boundary layer transition and provide an opportunity for both DSMC and Navier-Stokes techniques to be employed in predicting these flows. While the model configuration of the basic hollow cylinder cone geometry was preserved, experiments were conducted with an extended flare configuration to provide well-defined downstream boundary layer conditions for comparison with prediction schemes. For the double cone experiments, a 25°/55°

2

configuration was selected to avoid the potential of flow unsteadiness over the model; and again these studies were conducted at Reynolds numbers low enough to ensure that the flow was laminar downstream of the interaction over the second cone.

The results of these experimental studies were presented at the 2001 AIAA Reno meeting in a session dedicated to code validation. In this session, the predictors were given only information on the freestream conditions and the model geometry to determine the aerothermal properties over the models tested. In this "blind" code validation study, the predictors first presented their data, with the comparisons between theory and experiment presented independently at the conclusion of the session (see Refs. 5 and 6). In general, the comparisons between theory and experiment were excellent. For example, the comparisons shown in Figure 1 demonstrate that the size of the separated region and the magnitude of the heat transfer and pressure distributions through the separated and reattachment region were in excellent agreement with the experimental measurements. Likewise, comparisons between the density contours obtained from the Schlieren photographs over the double cone configuration compared in Figure 2 with Candler's predictions demonstrate almost perfect agreement. With the exception of the forebody flows the DSMC methods have not yielded as good an agreement as the Navier-Stokes method, which in part may be attributed to the high density of the flowfield in the reattachment region. Also, for complex dense flows, there are questions on the level of convergence of the solutions. The Navier-Stokes methods consistently overpredicted the heating rates over the forebody ahead of separation, potentially as a result of vibrational nonequilibrium and slip effects. Similar conclusions can be made for the comparisons between prediction and experiment over the hollow cylinder flare model. There again, questions arose concerning the modeling of the vibrational nonequilibrium in the freestream and slip effects near the leading edge of the models, which resulted in a second experimental measurement and numerical program to select the most effective techniques and analyses to determine the properties of the freestream in the presence of vibrational nonequilibrium.

In this section we discuss an additional set of experimental studies, conducted in conjunction with computations made by Candler (Ref. 7). to evaluate the effects of vibrational nonequilibrium of nitrogen in the freestream, thereby providing a more accurate definition of the freestream properties employed in the validation experiment. To validate the accuracy of the freestream properties deduced from the computational techniques employed at the Aerothermal and Aero-optic Evaluation Center (AAEC), and by Candler, measurements were made over the hollow cylinder detached from the flare and the $25°$ cone detached from the $55°$ conical second section of the model. Measurements were made over a large range of stagnation temperature and Reynolds numbers to obtain conditions that varied from rarefied to continuum in the region of the leading edges, and conditions where vibrational nonequilibrium was excited $(T_0 = 5,000°R)$ as in the earlier experiments and unexcited $(T_0 = 2,000°R)$ in colder flows in the freestream. The heat transfer and pressure measurements made in these studies were compared with detailed Navier-Stokes calculations and correlated in terms of the parameters used in simple predictive techniques. Also in these studies we examine the effect of levels of water vapor in the freestream on the calculations and on the experimental measurements. From this study, we validated the detailed and simple techniques, which are employed to describe the freestream conditions around the model in the presence of vibrational nonequilibrium of the test gas. Armed with these improved freestream conditions, we re-evaluated the comparisons between theory and experiment which were presented in Reno in 2001 (Refs. 5 and 6).

3

MEASUREMENTS MADE IN THE EXPERIMENTAL PROGRAM

Design of the Experimental Program

This experimental program was designed to obtain sets of surface heat transfer and pressure measurements and Schlieren photographs of the flowfield in complex shock/boundary layer and shock/shock interaction regions over simple model configurations. From these, an experimental database is derived at low enough densities to evaluate the performance of Navier-Stokes and DSMC methods in predicting these stressing flows. Two model configurations, a hollow cylinder/flare and a double cone model, were selected for these studies based on the experience obtained in earlier experimental studies and code validation exercises. The interest in the flow over the hollow cylinder/flare configuration stems from earlier computational difficulties which arose from rarefaction and shock interaction effects near the leading edge, and the complexity of the flow in the recirculation region. The short flare length selected for these earlier studies (see Ref. 1) did not allow a well-defined attached boundary layer to be developed downstream of the attachment and there is a possibility of forward propagation of disturbances from the base region. The configuration does not provide an optimal set of boundary conditions, and the flow is not ideal for comparison with computation. In the current studies we chose to move the end of the flare well downstream of the reattachment, thereby providing a well-defined boundary condition, which would anchor both experimental and theoretical measurements.

Earlier studies with double cone configurations, which were conducted principally to assess the accuracy of the models of flowfield chemistry, employed cone angles that could potentially lead to oscillations in the flow over the model. Such instabilities were observed in numerical computations and their sources were not fully understood. To avoid these instabilities in the current studies, we lowered the second cone angle to 55°, and validated this configuration with computations by Gnoffo (Ref. 8). Again, the length of the second cone was selected to ensure that a region of near constant pressure existed downstream of the interaction region at the junction between the cones and the shear layer impingement resulting from shock/shock interaction. Measurements were made for both sharp and blunted configurations that would introduce significant flowfield chemistry effects if testing were to be conducted in air. We used nitrogen as the driven gas to avoid significant dissociation effects. However, at the highest enthalpies, vibrational nonequilibrium can influence the heating rate to the surface of the model. Measurements over the cylinder flare and double cone configurations were made for a range of Mach and Reynolds numbers in order to obtain well-defined attached flows upstream and downstream of the corner interaction regions, and to examine the flow for any evidence of boundary layer transition at the back of the flare of the second cone.

In the second set of experimental studies, we examine vibrational nonequilibrium effects that were performed over 40 runs with just the hollow cylinder and the 25° section of the double cone model. These studies were conducted over a much larger range of Reynolds numbers (because we were no longer concerned with boundary layer transition) and total temperatures than the earlier studies with the complete configurations. This was done to vary independently the levels of vibrational nonequilibrium in the freestream and the leading edge interaction effects.

Models and Instrumentation

The Hollow Cylinder/Flare Configurations

A photograph of the hollow cylinder flare model employed in our studies is shown in Figure 3. As illustrated in Figure 4, a section of the flare is removable to turn this model into a configuration of the exact geometry of the model originally tested by Chanetz et al (Ref. 1). The length of the "extended flare" was selected based on calculations by Gnoffo to ensure that a well-defined length of constant pressure was obtained downstream of the interaction for the conditions of our experimental studies. The dimensions of the two models employed in our two studies are shown in Figure 4. Both models were highly instrumented with pressure and thin film heat transfer gages and positioned as illustrated in Figure 5. Instrumentation was also placed around the circumference of the flare to check for model alignment and any flow asymmetries. The test conditions were selected to ensure that flow over the entire extended flare configuration remained fully laminar with sufficient measurements upstream and downstream of the interaction to define the boundary conditions.

In the studies to examine vibrational nonequilibrium effects, we replaced the flare section of the model with a cylindrical extension incorporating the model support system. The cylindrical section of the model was equipped with similar instrumentation employed with the cone/flare model. This model is shown installed in the calibration rake alongside the forebody of the double cone model in Figure 6.

Sharp and Blunt Cone and Double Cone Configuration

The sharp 25°/55° double cone model shown in Figure 7 was selected as the principal configuration to be employed in our studies. This was based on evidence from our earlier experimental studies and numerical computations performed by Gnoffo that indicated that the flow would be fully stable for all the freestream conditions at which the model was tested. A series of blunt nosetips were fabricated for the 25° cone to investigate the effects of bluntness on the size and character of the interaction region. Diagrams showing the dimensions of the four configurations tested are shown in Figure 8. Limited studies were performed with the 25°/60° double cone configurations principally as a link to our earlier studies. Measurements were made with configurations shown in Figure 9, and again these flows were stable; however, only for the sharp configuration tested at our largest Mach number and lowest Reynolds number conditions did we obtain sufficient lengths of attached flow to meet our selection criteria.

The double cone model was highly instrumented with heat transfer and pressure instrumentation as shown in Figure 10. The additional heat transfer instrumentation was placed in the 25° cone for the studies that we conducted with only this section of the model. A second cone was fabricated and also instrumented with heat transfer gages. The two cones were tested together and in some cases, a blunt nose was placed on one of these cones. A photograph of the two cones mounted on the calibration rake for the "vibrational nonequilibrium studies" is shown in Figure 11.

Instrumentation Used in Survey Rakes

A photograph of a survey rake containing pitot-, static-, and cone-pressure probes, together with thin-film and Medtherm instrumented heat transfer probes, are shown in Figure 12. We

employed Cornell Aeronautical Laboratory (CAL)-designed piezoelectric pressure transducers, and Endevco and Kulite strain gage transducers, in our pitot pressure static pressure, and cone pressure probes. Under high enthalpy conditions, we used specially developed heat shields ahead of the piezoelectric transducers used in the pitot pressure rake. Miniature Endevco and Kulite pressure gages are mounted close to the surface in our static pressure probes. The low-pressure piezoelectric instrumentation is capable of measuring pressures down to 10^{-4} psia with accuracy of $\pm 10\%$, and we have obtained similar accuracy with the low-pressure Kulite and Endevco transducers. Stagnation point heat transfer measurements are made with both platinum thin-film and thermocouple coaxial heat transfer gages. We also make measurements around the hemispherical stagnation point heating probes. In these studies, we also added a small cylindrical stagnation point heat transfer gage depicted in Figure 12. In our studies radiation measurements were employed to determine the level of water vapor in the airflow. A photograph of the measurement head of one of these instruments is shown in Figure 13.

High-Speed Schlieren Imagery with High Speed Video System

The low-densities of the flowfields generated in these studies mandated that a double pass Schlieren system be employed. Schlieren images were obtained through the use of a pulsed copper vapor laser as the light source, and a high-speed video camera as the recording instrument. Since laser coherence effects are not desired in this application, the Oxford Lasers LS-20 copper vapor laser was operated without mirrors. Its light output was then delivered through 10 meters of fiber optic cable to further minimize coherence. The high-speed Kodak *Ektapro* camera was operated at the laser pulse frequency of 4,500 pulses per second. Thus, images were obtained throughout the complete run sequence, detailing flow start up, stable operation, and flow breakdown. Another distinct advantage for low-density measurements was the high intensity available from the laser source. The laser intensity was controlled through a variable neutral density filter. To achieve high Schlieren sensitivity, the knife-edge cut-off could be increased without fear of losing image illumination. In this way, the recorded contrast could be optimized for these flow density flow disturbances. Finally, because of the digital nature of the recorded images, simple software enhancement of the image contrast was utilized to produce the final images.

Test Facilities and Determination of Freestream Conditions

Introduction

The capability to obtain accurate measurements in fully laminar regions of shock/shock and shock/boundary layer interaction in hypervelocity flows requires the use of wind tunnel facilities capable of generating high-quality, high-temperature, low Reynolds number flows. Over the past 40 years, since the development of the shock tunnel at CAL, a concerted effort has been made in our laboratory to develop and use these facilities and the associated tunnel and model instrumentation in fundamental studies in low Reynolds number shock/boundary layer interacting flows, with and in the absence of flowfield chemistry for the purpose of developing and validating the prediction techniques. The 48-inch tunnel developed at CAL has been proven over its 40-year history to generate high-quality low Reynolds number flows, and the measurements made in the facility have been validated by flight tests from the Gemini to the space shuttle as well as in comparisons with well-established prediction techniques. The design of the LENS I facility incorporates many of the key features learned from our earlier facility development, as well as improvements in the tunnel components and a significant increase in the

high-pressure, high-enthalpy (2,000 atm/12 MJ/kg) and test time performance of the tunnels. These tunnels are being employed in our Verification, Validation and Analysis (VV&A) programs for both facility and code validation, with the effort centered initially on comparing measurements in complex regions of shock wave/laminar boundary layer interaction and separated flows developed on models tested in these facilities with the most current sophisticated prediction techniques.

Experimental Facilities

48-inch Shock Tunnel

We employed the 48-inch shock tunnel first in the studies with the double cone model configurations and subsequently in the studies with the hollow cylinder and 25° cone model. A photograph of the double cone model mounted in the test section of the 48-inch tunnel is shown in Figure 14. Shown in Figure 6 is a photograph of the hollow cylinder/flare and 25° cone model supported in the survey rake for the vibrational nonequilibrium studies. A schematic diagram of the operation is shown in Figure 15. The 48-inch shock tunnel (and the LENS facility discussed below) is basically a "blow-down tunnel" with a shock-compression heater. The flow through the tunnel is initiated by rupturing a double diaphragm, permitting high-pressure gas in the driver section to expand rapidly into the driven section. This generates a normal shock, which propagates through the gas in the driven tube, where it is heated and compressed. A region of high-temperature, high-pressure air is produced between this normal-shock front and the gas interface (often referred to as the contact surface). When the incident shock strikes the end of the driven section, it is reflected, leaving a region of almost stationary, high-pressure, heated air. This reservoir gas is then expanded through a nozzle to the desired freestream conditions in the test section. The duration of the flow in the test section is controlled by the interactions between the reflected shock, the driver/driven-gas interface, and the leading expansion wave generated by the non-stationary expansion process occurring in the driver section. We control the initial conditions of the gases in the driver and driven sections so that the gas interface becomes transparent to the reflected shock, which is referred to as operating under "tailored-interface" conditions. In preparation for the double cone studies flowfield calibrations were performed for the specific test points at which the experimental studies were conducted. A typical distribution of Mach number across the exit plane of the 48-inch "D" Nozzle obtained in the earlier calibration run is shown in Figure 16, which demonstrates excellent flow uniformity across the model width.

LENS I Shock Tunnel

We employed the LENS I facility in the studies of both the double cone and hollow cylinder/flare programs. We began our studies in the LENS I tunnel by repeating several sets of measurements made earlier in the 48-inch tunnel with the 25°/55° double cone configuration, as part of our facility-to-facility validation program. A photograph of the test section, nozzle and driven sections of the LENS I and II shock tunnels are shown in Figure 17. We then used a model with temperature-sensitive paint to evaluate the symmetry of the flow in the separated region. All the hollow cylinder/flare studies were conducted in the LENS I facility. A photograph of the hollow cylinder/flare model with the total pressure and heat transfer rakes supported below it are shown in Figure 18. The layout of facilities supporting Legs I and II of the LENS facility are shown schematically in Figure 19. Nitrogen, helium and hydrogen can be employed as driver gases allowing tailored interface operations up to a velocity of 14,000 ft/sec. The LENS I facility

has two contoured nozzles allowing it be operated over a range from Mach 7 to 18 (see Figure 20). Test times of up to 24 milliseconds can be obtained at velocities from 3,000 to 15,000 ft/sec, respectively in this tunnel. Both LENS Leg I and Leg II are operated under tailored interface conditions by carefully controlling the operating parameters and the gases employed in the driver and driven tubes. The Mach 8 and 14 nozzles for LENS Leg I have exit plane diameters of 44 and 48 inches, respectively, which allow the installation of models of up to 24 inches in diameter and 12 feet long.

Measurement of Tunnel Stagnation and Freestream Conditions

The facility test conditions are established and validated by a combination of measurements in the reservoir region and test section of the tunnel. The stagnation pressure and enthalpy are obtained directly from pressure measurements in the driven tube behind the reflected shock, and measurements of the incident and reflected shock Mach number are made with thin-film high frequency heat transfer gages. Conditions in the freestream are obtained from survey rakes (similar to those shown in Figure 21) containing pitot pressure, cone pressure, and static pressure probes, stagnation heat transfer probes (hemispherical and two-dimensional cylinders containing platinum thin film resistance thermometers and coaxial thermocouple gages), and total temperature measurements with vented thermocouple probes (where applicable). From these probes, we can determine the freestream dynamic pressure with an accuracy of $\pm5\%$, the stagnation point heating with an accuracy of $\pm7\%$, and the freestream Mach number with an accuracy of $\pm1.5\%$. A typical distribution of Mach number from a flow field survey conducted just prior to the beginning of the cylinder/flare studies in LENS I is shown for the conditions in Figure 22.

PRESENTATION OF EXPERIMENTAL MEASUREMENTS

Measurements with the Hollow Cylinder and with the 25°Cone Model to Examine Effects of Freestream Vibrational Nonequilibrium

Introduction

The experiments conducted in this second phase of the program were designed to provide us with a better understanding of the contribution of vibrational nonequilibrium on the properties of the freestream and on the heating and pressure levels of the model. Vibrational nonequilibrium effects have been extensively researched particularly at the Cornell Aeronautical Laboratory, predecessor of CUBRC, where the classic work of Treanor (Ref. 9) has defined the basic mechanisms involved in these flows. However, despite the relatively extensive theoretical studies there has been little direct confirmation from measurements made in wind tunnels in hypervelocity airflows. It has been generally been accepted that the effects of air chemistry on the freestream properties overwhelm the vibrational nonequilibrium effects for hypersonic airflows at velocities of 9,000 ft/sec and above. At these velocities, the energy exchange between vibration and the reacting components of the airflow is rapid enough to bring the vibrational temperature of nitrogen close to the translation temperature of the flow. For nitrogen flows, in a similar velocity range, the situation is somewhat different. For totally pure nitrogen flows, for which the vibrational relaxation rates are low, the freezing of energy in the vibrational mode at or just downstream of the throat can result in a significant amount of energy locked in the flow through the test section. However, in the presence of impurities such as water vapor, there is significant debate as to whether these impurities accelerate the vibrational relaxation process in the nozzle. If the relaxation is enhanced, energy is returned to the flow in the form of increased

8

velocity as the vibrational temperature drops towards the translational levels. Evidence to suggest this might happen has been presented by Boudreau (Ref. 10) on studies in Hotshot facilities (which in fact can contain more impurities than just water vapor) with measurements indicating that vibrational "thawing" occurs where the vibrational temperature relaxes more quickly to the translational temperature than would be predicted with the standard relaxation rates. There is a generally held belief that, in many nitrogen tunnels, the vibrational temperature is closer to that of translation than the calculations suggest. However, in most hypersonic facilities, the stagnation temperature of the flow is designed to be just sufficient to prevent condensation and cluster formation in the test section. Hence stagnation temperatures under these conditions are well below levels where there is a significant amount of energy in vibration in the reservoir. However, when true hypervelocity flows (more representative of flight conditions) are developed in a high enthalpy facility, vibrational nonequilibrium is an important consideration. This is particularly true for high-purity shock tunnels similar to the ones used in these experimental studies. For our studies, we filled the driven tube with nitrogen from bottles containing nitrogen, which was certified to be of high purity. However, for low-density flows, where the pressure in the driven tube is below an atmosphere, water vapor adsorbed on the walls of the tunnel can be drawn into the test gas, and although these amounts are extremely small, they potentially can influence the vibrational relaxation rates. In the first part of the study, we investigated the effects of the levels of water vapor in the driven tube by conducting studies where a hard vacuum was applied to the driven tube for over three days to eliminate as much water as possible. To the other extreme, water was introduced in the tube in order to saturate the flow. We compared the heat transfer measurements to the cone and cylinder for these conditions as well as for the conditions developed during a normal testing cycle where the driven tube was subjected to a vacuum for a relatively short time. Shown in Figure 23 are the heat transfer measurements made for the three levels of water vapor in the facility. It can be seen that there is virtually no difference between the measurements made for the two cases where we do not introduce water into the flow. For the case when water is added, the heating levels are indeed smaller, which almost certainly results from the energy absorbed in water vapor. For standard tests in which high purity gas is used, we believe that it is a reasonable assumption that the flows can be computed accurately using the classical rates suggested by Millikan and White (Ref. 11) for vibrational nonequilibrium. The flows in the test section for the experiments discussed below and for the test cases employed in the validation study (Ref. 5) were recomputed using our 2D nonequilibrium airflow code (NETCON) and the full Navier-Stokes computation incorporating flowfield chemistry developed by Graham Candler for the expansion down the contoured nozzle used in the experimental studies. Although different assumptions are made to describe the development of the boundary layer down the nozzle, the two sets of computations were found to be in excellent agreement with predicted differences in the freestream velocity of less than 1%. (Ref. 12).

Survey Rake Measurements to Define Freestream Properties

Flowfield surveys were made at each of the test conditions for which code validation measurements were made on the double cone and the hollow cylinder/flare model. The survey rake (which was similar to that shown in Figure 21) contained a full complement of pitot pressure gages as well as heat transfer instrumentation to measure the heating in the stagnation region and around the hemispherical probes. We also employed cone probes, which, in conjunction with the pitot probes, can be used to provide measurements of the static pressure in the freestream. As discussed previously, the freestream properties are derived in our non-

equilibrium nozzle code (Ref. 13) from measurements of the pressure and enthalpy in the tunnel reservoir and pitot pressure in the test section; the stagnation point heating and cone pressure data provides additional validation of the test conditions. Examples of the Mach number distributions across the core flow are shown in Figures 16 and 22. The model support system and survey rake assembly employed in the studies with the hollow cylinder and the 25° cone are shown in Figures 6 and 12 respectively. With the models placed in the core of the flowfield, the pitot probes and supporting survey probes were positioned to include also measurements of the structure of the outer flow and nozzle boundary layer. This information was then available to evaluate the effectiveness of the models employed by Candler (Ref. 14) to compute the turbulent boundary layer growth along the walls of the contoured "D" nozzle. Examples of the comparisons between the rake measurements and the predicted distribution of Mach number are shown in Figures 24 and 25. The good agreement shown in this figure provides strong support for the models used in the codes.

Studies to Examine Vibrational Nonequilibrium Effects on the Heating and Pressure Distribution to the 25°Cone.

In this segment of the experimental program, we made detailed measurements of heat transfer on two 25° cones and surface pressure measurements were made on one cone, for a large range of reservoir enthalpies and pressures. From this, it was possible to examine how the heating levels were influenced by the magnitude of the energy frozen in vibration in the flow through the test section. The flow conditions at which the studies were conducted are listed in Table 1-I, which shows that the measurements were made for stagnation temperatures of 5,000°R (at which the double cone studies were conducted), down to temperatures 2,000°R where nitrogen vibration is only weakly excited. Measurements were also made for a range of stagnation pressures to vary the strength of the viscous interaction at the tip of the cone.

The measurements were examined by (i) comparing with directly with Navier-Stokes calculations performed by Candler (Ref. 7), and (ii) correlating the measurements in terms of parameters which characterize the viscous interactions close to the tip of the cone. Three comparisons between Candler's calculations and the heat transfer measurements over the cone are presented Figures 26, 27 and 28; these correspond to reservoir temperatures of 3,000°R, 4,000°R and 5,000°R respectively. For the low enthalpy flow (Run 15) where nonequilibrium effects are small and slip effects diminish at the rear of the cone, all the solutions (shown in Figure 26) are in good agreement with the measurements. From Figure 27 it can be seen that at the intermediate stagnation temperature, high-pressure condition, at which Run 12 was conducted, the measured data are in good agreement with the calculations made by incorporating only the effects associated with vibrational nonequilibrium. For the high enthalpy low Reynolds number conditions for Run 8, Candler found that in order to obtain good agreement with the experiment, he must account for the effects of both vibrational nonequilibrium and surface slip. The heat transfer measurements made on the cone for the large range of test conditions were correlated in terms of heat transfer coefficient C_H

$$C_H = q/(\rho_e U_e [H_R - H_w])$$

$$\text{Where } H_R = C_p T_e + \sqrt{P_r} \, U^2/2$$

and the viscous interaction parameter

$$\overline{\chi}_L = M^3 \sqrt{C^*/Re_L}$$

where C^* is evaluated at the reference temperature $T^* = T_0 (1+3T_w/T_0)/6$

Comparisons have been made for the range of freestream conditions listed in Table 1-I. The sensitivity of the heat transfer coefficient to Mach number has been removed empirically by multiplying it by the cube of the Mach number. This product, plotted against $\overline{\chi}_L$ is presented in Figure 29. Although it is difficult to see because the measurements obscure the lines, small values of $\overline{\chi}_L$ the measured data are in are in relatively good agreement with Cheng's (Ref. 16) empirical prediction methods and Candler's Navier-Stokes computations. At more rarefied conditions, the heating is less than predicted by either method. This effect is more easily observed by plotting only the measurements obtained at the highest enthalpy conditions, where, as shown in Figure 30, Candler's predictions including slip are seen to be in good agreement with the measurements except for the data at the most rarefied values of $\overline{\chi}_L$. Plotting the measurements for the largest unit Reynolds number, as shown in Figure 31, we observe good agreement with the empirical methods and the Navier-Stokes predictions. Figure 32 shows a correlation of the pressure measurements and the semi-empirical and Navier-Stokes predictions. This demonstrates good agreement and is indicative of the cone pressures being only very weakly influenced by vibrational nonequilibrium.

Examination of Effects of Reservoir Pressure and Enthalpy on the Pressure and Heating on the Hollow Cylinder Model.

The studies with the hollow cylinder followed the cone study; however in this segment of the program, we also obtained measurements on one of the cone models positioned on the rake as shown in Figure 6. Measurements of heat transfer and surface pressure distributions were again made for a large range of reservoir enthalpies and pressures, (see Table 1-IIA and 1-IIB) to examine how the heating and pressure levels were influenced by the energy frozen in vibration in the flow through the test section, and to vary the characteristics of the viscous interaction over the leading edge of the cylinder.

Again we compared our measurements with Candler's computations, correlating them in terms of similarity parameters. Comparisons between experiment and predictions for Runs 26 and 43 are shown in Figures 33 and 34 respectively. Both have similar freestream velocities but Run 26 was conducted at a larger reservoir pressure. In this latter case the slip effects are smaller and this is reflected in the calculations. However to predict the data for Run 43 most accurately, nonequilibrium vibration and slip must both be included in the calculation. We again correlated the heat transfer and pressure measurements to the cylinder in terms of the same heat transfer and viscous interaction parameters used for the cone measurements. Figure 35 shows the result for all the heat transfer measurements on the cone together with semi-empirical and Navier-Stokes predictions. At large values of χ_L we again see evidence of decreased heating resulting from slip effects. This is more easily observed by plotting the measurements taken at the highest enthalpy condition for a range of Reynolds numbers as shown in Figure 36. Finally, we see that (as shown in Figure 37) the measurements are in good agreement with predictions at the highest Reynolds number conditions. Figure 38 shows the correlation of pressure over the cylinder flare model. Here we see that the weak interaction theory is in relatively good agreement with the measurements as are the predictions of Candler.

Measurements on the Double Cone Models and Comparison with Predictions

Introduction

The studies with the double cone configuration were initially conducted as part of an investigation sponsored by AFOSR to examine and model real-gas effects in hypersonic flows. During the course of these studies, researchers at CUBRC and Cal-Tech decided that one approach to evaluating the models of air thermal nonequilibrium and chemistry employed in the Navier-Stokes prediction techniques was to perform experiments with model configurations the flows over which were calculated to be sensitive to real-gas effects. The studies performed at Cal-Tech concentrated on a double wedge configuration, while those employed in the experiments at CUBRC employed an "indented nose" or double cone configurations similar to those investigated earlier in studies of idealized ablated nose shapes. The flowfields over these configurations involved both separated regions induced by shock/boundary layer interaction and regions of shock/shock interaction resulting from the intersection of the forebody shock with the shock generated by the second compression surface. Calculations by Candler (Ref. 7) showed that these flows were extremely sensitive to the models of air thermal nonequilibrium and chemistry employed in the calculations.

On the basis of earlier indented nose studies, we selected a 25°/60° double cone configuration for our initial studies. Measurements were made in both air and nitrogen flows, and these studies indicated that there were significant real gas effects on the size and properties of the interaction regions (Holden, Ref. 4). However, the flowfield configurations coupled with limited instrumentation did not allow us to draw a conclusion that the flow remained fully laminar throughout the interaction region, and therefore, these experiments did not meet the requirements of a study with well-defined boundary conditions with the avoidance of uncertainties that arise due to transition somewhere within the flow. In addition, first Candler and then Gnoffo (Ref. 18) found that they could not obtain stable flowfields over these configurations, suggesting that the flow may be intrinsically unsteady or that the differencing schemes were unsuitable for these flow configurations. Based on this experience, we decided to build a new series of models with significantly more instrumentation and to conduct experiments for conditions where the flows would remain laminar over the complete model and well-defined regions of attached flow were generated both upstream and downstream of the shock/boundary layer and shock/shock interaction regions.

The run matrix for the studies on the double cone configurations is listed in Table 1-IIII. Although the major studies were conducted with a 25°/55° configuration, we began our studies with the 25°/60° double cone configuration to examine in more detail whether these flows were unstable, as predicted by the numerical codes. Measurements were made for a range of freestream conditions and nosetip bluntnesses with these combinations being selected so that well-defined attached laminar boundary layers were obtained both upstream and downstream of the interaction regions. We then selected tests from this series conducted in the 48-inch tunnel and repeated these in the LENS I facility to establish facility-to-facility validation of the measurements. Studies were also conducted in the LENS I facility with fast-response temperature sensitive paint to confirm the axisymmetric nature of the flow over the body. The facility validation studies as well as those conducted with 25°/60° double cone configuration are discussed in Reference 5. Only details of the tests on the 25°/55° cone are included in this report.

Measurements with the 25°/55° Double Cone Configuration and Comparisons with Predictions

Introduction

In this experimental series, we obtained measurements first with a sharp nosetip for a single condition at Mach 12 and then for a series of Reynolds numbers at Mach 10. These studies were followed by a similar series with the 0.25"-nose radius. Finally we obtained measurements at the lowest Reynolds numbers with nose radii of 0.29" and 0.6". From the measurements made in this segment of the program, we selected four specific flow configurations for comparison with numerical predictions. The cases chosen were ones where the flow well upstream and downstream of the interaction regions exhibited well-defined regions of constant pressure.

Comparison with Measurements for Run 35

The first set of such measurements (Run 35) for a Mach number of 12.50 and a Reynolds number of 6.7×10^4 is shown in Figures 39 and 40. Figure 39 shows a comparison between the experimental measurements and Candler's Navier-Stokes based computations given in References 7 and 9. Both predictions describe the pressure and heat transfer distribution through the separated and shock/shock interaction regions with remarkable accuracy. The computed values of heating rate ahead of the separation are, however, consistently a little below the measurements. By incorporating the effects of vibrational nonequilibrium and vibrational slip, Candler's predictions for the forebody heating and length of the interaction region are slightly improved. Boyd's predictions (Ref. 15) with the DSMC code for Run 35 are shown in Figure 40. These predictions clearly underestimate the length of the separated region and although the heating to the forebody is slightly underpredicted, there is good agreement between theory and experiment for the pressures and the heat transfer downstream of the shock/shock interaction on the second cone.

Comparison with Measurements for Run 28

The measurements at Mach 10.5 at a similar Reynolds number of 5.8×10^4 are compared with numerical predictions by Candler (Ref. 7), Gaitonde (Ref. 17), and Gnoffo (Ref. 18) using Navier-Stokes code (Figures 41, 42, 43 respectively), and by Moss (Ref. 19) and Boyd (Ref. 15) (Figures 44 and 45) using DSMC code. For the solutions obtained by Candler, again we observe (Figure 41) excellent agreement between the predictions and experimental data for both the theoretical predictions. Adding vibrational nonequilibrium improved forebody heating prediction without changing the size and properties in the recirculation and reattachment regions.

The solution obtained by Gaitonde for Run 28 (Figure 42) is in close agreement with Candler's earlier predictions, giving excellent predictions of the length of the separated region and the heating in and downstream of the region of shock/shock interaction on the second cone. Adding vibrational nonequilibrium effects should improve the heat transfer predictions on the forebody.

Similar comments can be made for the solutions of Gnoffo for Run 28 (Figure 43). Again the agreement between the theory and experiment and the different computational schemes is remarkable in the complex flows in the regions of shock/shock interaction. These calculations come the closest to predicting the exact length of separated region and the heating and pressure in the reattachment region.

The next two solutions, which were obtained with the DSMC method, again significantly underpredict the scale of the interaction region and the position and magnitude of the properties in and downstream of the region of shock/shock interaction. Moss' calculations shown in Figure 44 indicate that the predicted separated region is approximately 25% of the length measured in the experiment. Downstream of the interaction regions the pressure and the heating levels are relatively well predicted. Boyd's solution for Run 28 also significantly underpredicts the length of the separated region, and unlike Moss's calculation, the heat transfer rates both ahead and downstream of the interaction and underpredicted. It is doubtful if incorporating vibrational nonequilibrium effects would significantly improve these calculations.

Comparisons with Measurements for Run 31

Predictions for Run 31 (a Mach number of 12.4 and a Reynolds number of 6.1 x 10^4) were made by Roy (Ref. 20) using the Navier-Stokes solver, and Gallis and Bartel (Ref. 21) using the DSMC method. The measurements for this case were made for a blunted cone with a 0.5" nose radius. Roy's solution which is compared with the measurements of heat transfer and pressure in Figure 46 are in excellent agreement with the size and properties of the separated region, and the flow in and downstream of the reattachment compression process. The pressure distribution over the entire model is predicted almost exactly. We anticipate that the differences between the measurements and prediction would be improved by incorporating vibrational nonequilibrium effects, as they pointed out earlier. The DSMC solution by Gallis and Bartel for Run 31 again illustrates that the DSMC method significantly underpredicts the size of the separated region (see Figure 47). However, the predicted pressure levels upstream and downstream of the interaction region are in good agreement with the experiment. The heating levels throughout the interaction region are generally overpredicted. The lack of agreement between the predicted and measured separated length is surprising, since these DSMC solutions were performed with an extremely powerful computer, giving a highly resolved and converged solution.

The reason for the trend seen in all of the DSMC computations to underpredict the separation length should be the focus of further study. The Gallis and Bartel computations in particular appear to be highly resolved and fully converged. The DSMC solutions advances in real time from an impulsive start, and it is possible that although an apparent quasi-steady state has been established, insufficient time has elapsed for the recirculating flow in the bubble to reach a final solution. The quasi-steady state could be established through the transmission of acoustic velocity perturbations within the solution, whereas the real flow will evolve also through a mechanism involving the transportation of fluid around the separation bubble. This process is likely to be slower and may not have been captured correctly in the DSMC solutions.

Comparison with Measurements of Run 24

Finally we compare the measurements in Run 24 at a Mach number of 10.4 and a Reynolds number of 10.4 x 10^4 with solutions obtained by Gnoffo using the Laura Navier-Stokes code (Figure 48). Although the solutions slightly overpredict the length of the separated region, the pressure levels through the entire interaction region are well predicted, as are the heating levels in the separated and reattachment regions. Again, incorporating vibrational nonequilibrium into the solution could lead to more accurate predictions of the forebody heating.

Measurements for Run 26

Although we did not receive predictions for Run 26, the sharp double cone configuration run at Mach number of 10.4 and a Reynolds number of 8.0 x 10^4, the well-defined flowfield

generated under these conditions could well be used for code validation. As in the earlier test cases, there are well-defined regions of constant pressure both upstream and downstream of the interaction region and the peak pressure and heat transfer in the shock/shock interaction region are well defined. The Schlieren photograph in Figure 49 shows well-defined features of the separation and afterbody shocks including a Type IV interaction induced by the interaction between the separation shock and the afterbody shock.

Measurements for Blunt Nose Configurations

Runs 32, 36, 33 and 38

For completeness we have included three additional measurements for which we did not receive predictions (Figures 50-53). These cases, which were run at a nominal Mach number of 10, illustrate that the separated region increases significantly with increased unit Reynolds number as would be anticipated for fully laminar interaction regions. An examination of the variation of the heating at the end of the second cone with Reynolds number shows no evidence of boundary layer transition. Increasing the Mach number from 10 to 12 holding the same Reynolds number as Run 32 has remarkably little influence on the size of the separated region, a result which was unexpected. For Run 38, well-defined characteristics of this flow would make it suitable for comparison with prediction.

Measurements and Comparison with Hollow Cylinder/Flare Models

Introduction

The experimental program with the hollow cylinder/flare configurations was conducted in two phases – the first sets of measurements were obtained with the extended flare configuration. Then, when we had selected the freestream conditions that gave interaction regions with the best-defined characteristics, we conducted the second phase of the program at these conditions, with the original French cone/flare configuration. The run matrix for the measurements on the hollow cylinder/flare configuration with the extended flare and the basic flare configuration are listed in Table IIA and IIB respectively. These studies were preceded by detailed flowfield calibrations at each of the freestream conditions selected for the experiments. For the "blind" calibration study reported in Reference 6, 15 computations for the hollow cylinder/flare model were submitted covering seven test cases. A major number of solutions (11) were for the extended flare configuration. Almost all the predictions gave excellent results for the density contours over the model when compared with the Schlieren photographs. Figure 54 shows the density contours predicted by Gnoffo superimposed on the Schlieren photograph of the flow. The characteristics of the separated region as well as the shock waves developed over the leading edge and in the reattachment compression surface are well predicted by the Navier-Stokes solution.

Measurements for Hollow Cylinder/Extended Flare Models and Comparison with Predictions

Comparison with Measurements for Run 14

We received the most predictions for Run 14 which is an extended flare case conducted at a Mach number of 10.3 and an intermediate Reynolds number of 7.8×10^4. We have received two solutions from Candler, one with calculations for the original set of conditions and a second, where vibrational nonequilibrium was computed along the nozzle and in the test flow. Figure 55 shows these two predictions compared with the measurements of heat transfer and pressure obtained over the model. While the flows in the recirculation and reattachment compression

region were computed with roughly equal accuracy with and in the absence of vibrational nonequilibrium, the pressure and heat transfer measurements over the hollow cylinder ahead of the interaction region are calculated well with and without including vibrational nonequilibrium effects.

Gnoffo's calculations (Figure 56) for this test case are in almost perfect agreement with the length of the interaction regions and the pressure and heat transfer measurements.

Surprisingly, the calculations of Tannehill (Ref. 22) (Figure 57) underpredict the length of separated region and the pressures but heat transfer in the forebody and reattachment region of the flow are well predicted.

Comparison with Measurements for Run 9

Run 9 was conducted under the highest Reynolds number, (10.9×10^4) Mach 12.5 condition and for this case, the "blind" calculations of Gnoffo are almost in total agreement with the measurements. As shown in Figure 58, the length of separated region and the peak pressure and peak heating at the end of the reattachment and compression process are calculated almost exactly.

Not surprisingly, the predictions with the DSMC calculations obtained by Moss (Figure 59) follow the generally observed trend and underpredict the length of the separated region although the pressure and heating levels through and downstream of the interaction agree quite well with the measurements.

Comparison with Measurements for Run 11

The flow conditions for Run 11 (Mach Number 12.2 and Reynolds number of 6.3×10^4) were such that the flow was close to incipient separation and a very small recirculation region was present. As shown in Figure 60, while Candler's prediction of the forebody flow achieves reasonable agreement with experiment when vibrational nonequilibrium effects are included, the predicted length of separated region also increases. Likewise, as shown in Figure 62, Gnoffo's Navier-Stokes calculation also overpredicts the size of the recirculation region although the values for heat transfer and pressure are in relatively good agreement everywhere except the recirculation region. Tannehill's (Ref. 22) calculations (Figure 61) are in good agreement with the size of the separated region and the pressure level through the interaction region.

Moss's (Ref 19) calculations using the DSMC method shown in Figure 63 also predict closely the small size of the interaction region and the heating and pressure distribution of the entire flow are well predicted. This appears to confirm that the basic problem with the DSMC computations rests in an inability to fix the length of the separation region, for the case very close to incipient separation where this is not an issue, the method is quite successful in determining the remainder of the flowfield.

Boyd's DSMC computations shown in Figure 64 are in agreement with the measured scale of the separated region and although the pressure predictions are in good agreement with the experiment, the method tends to underpredict the heating both ahead and downstream of the interaction region.

Comparison with Measurements for Run 8

The high Reynolds number test conditions for Run 8 (Mach 12.5 and Reynolds number 14.6 $\times 10^4$) produced the largest separated region over the cylinder flare model and again Gnoffo's

calculations shown in Figure 65 are almost in exact agreement with the experimental data, even capturing the peak pressure and peak heating levels at the end of the reattachment compression process.

Measurements for Hollow Cylinder/Original Flare Models and Comparison with Predictions

Introduction

The dimensions of the hollow cylinder/short flare model were exactly those of the model tested earlier by Chanetz et al (Ref. 1). Computations of the flow over this configuration made earlier at the Antibes Workshop held in France in 1989 demonstrated that the solutions were extremely sensitive to the modeling of the flow over the leading edge, the gridding of the recirculation region and the differencing schemes used in this region of the flow. While in this flow configuration measurements made in the current studies suggest that reattachment occurs at the tip of the flare, the separated region is smaller than if the expansion fan were well downstream, as is in the case of the expanded flare. Again, as shown in Figure 66, the computation of density contours over the model computed by Gnoffo for Run 18 are in excellent agreement with experiment.

Comparison with Measurements for Run 18

For this test case, which was at the largest Reynolds number (14.3×10^4) at Mach 12.5, we obtain the large separated region. Gnoffo's predictions for this condition shown in Figure 67 again are in good agreement with the experimental data, almost capturing the length of the interaction region and the magnitude of heat transfer and pressure throughout the flow. Clearly the lessons from the Antibes and subsequent code validation studies have been learned.

Comparison with Measurements for Run 19

With DSMC computation for the short-flare case, at an intermediate Reynolds number of 7.92×10^4, the calculations made by Moss are in relatively good agreement with the measurements of heat transfer and pressure. Moss predicts a shorter interaction region and this results in a peak in the pressure and heat transfer before the end of the flare as shown in Figure 68.

CONCLUSIONS

In this section of the RTO/AVT activity, we examined the capabilities of the Navier-Stokes and DSMC prediction techniques to accurately describe the aerothermal characteristics of complex laminar viscous flows generated in regions of shock wave/boundary layer interaction and shock/shock interaction in hypervelocity flows. Two simple axisymmetric body shapes were selected for these studies, a hollow cylinder/flare configuration, and double cone configuration, each of which has been shown to generate flow, which can stress the computation techniques. Experimental studies in which detailed heat transfer and pressure measurements were made in hypervelocity flows at Mach numbers of 10 and 12 over a range of Reynolds numbers low enough to ensure the flows remained laminar over the models, and that both Navier-Stokes and DSMC methods could be employed to calculated the flows. The measurements from these experimental studies was first released in a "blind validation study" where the predictors were given only the model geometry and the conditions in the freestream so, other than conferring with each other, they had no knowledge of the results. Based on their earlier experience the participants expressed misgivings about the accuracy of the predictions, particularly for the

double cone cases where both the gridding and the selection of the differencing schemes proved to be of critical importance. This blind validation exercise demonstrated that sound decisions can be made by the best computationalist, and the accuracy of the predictions can be truly impressive. In the best Navier-Stokes solutions the structure and density of the flowfield was captured exactly over both the hollow cylinder/flare and double cone models. The detailed characteristics of the distribution of pressure and heating through the interaction regions were well predicted. In general, for these relatively high-density flows, the DSMC solutions did not capture the characteristics of well-separated flows. The slight disagreement with the heating on the forebody of the double cone models stimulated in a second experimental investigation to examine the effects of vibrational nonequilibrium on freestream conditions and on the forebody heating. This study was performed in concert with numerical analysis of the flow in the nozzle and over the cylinder and cone models using both simple and detailed Navier-Stokes modeling. The combined set of flowfield and model measurements were then used to validate the calculations of the freestream conditions in the presents of vibrational non-equilibrium. Comparisons between the computations and the experimental data evaluated with the updated freestream conditions improved the already good agreement between prediction and experiment.

Table 1-I										
Vibrational Nonequilibrium Studies										
Run	Po	Ho	Po'	Uinf	Rhoinf	Pinf	Tinf	Tvinf	M	Re/ft
	psia	(ft/sec)^2	psia	ft/sec	slugs/ft^3	psia	deg. R	deg. R		
44	3618	3.59E+07	2.83	8.03E+03	6.86E-06	1.28E-02	1.52E+02	3.76E+03	13.08	4.54E+05
12	2529	3.70E+07	2.003	8.13E+03	4.73E-06	9.18E-03	1.57E+02	3.98E+03	13.01	3.05E+05
31	1747	3.76E+07	1.47	8.16E+03	3.45E-06	6.90E-03	1.62E+02	4.18E+03	12.87	2.17E+05
11	1195	3.59E+07	1.002	7.95E+03	2.48E-06	4.62E-03	1.51E+02	4.25E+03	12.97	1.63E+05
27	802	3.90E+07	0.964	8.23E+03	2.22E-06	5.18E-03	1.89E+02	4.59E+03	12.01	1.20E+05
26	599	3.72E+07	0.557	8.04E+03	1.35E-06	2.65E-03	1.60E+02	4.59E+03	12.77	8.46E+04
43	469	3.66E+07	0.435	7.95E+03	1.07E-06	2.11E-03	1.59E+02	4.61E+03	12.65	6.70E+04
25	412	3.89E+07	0.398	8.19E+03	9.26E-07	1.96E-03	1.71E+02	4.82E+03	12.55	5.51E+04
40	1759	2.32E+07	1.332	6.43E+03	5.03E-06	5.97E-03	9.63E+01	3.19E+03	13.15	4.44E+05
38	907	1.79E+07	0.689	5.70E+03	3.32E-06	3.05E-03	7.46E+01	2.65E+03	13.23	3.52E+05
35	775	1.63E+07	0.598	5.45E+03	3.14E-06	2.66E-03	6.88E+01	2.45E+03	13.20	3.53E+05

Table 1-IIA										
Extended Flare Configuration										
Run	Po	Ho	Po'	Uinf	Rhoinf	Pinf	Tinf	Tvinf	M	Re/ft
	psia	(ft/sec)^2	psia	ft/sec	slugs/ft^3	psia	deg. R	deg. R		
14	251	3.36E+07	0.625	7.56E+03	1.71E-06	4.57E-03	2.17E+03	4.44E+0.3	10.30	7.38E+04
13	366	3.87E+07	0.896	8.13E+03	2.11E-06	6.51E-03	2.50E+02	4.50E+03	10.32	8.59E+04
3	422	3.73E+07	1.11	7.98E+03	2.72E-06	8.33E-03	2.48E+02	4.57E+03	10.16	1.09E+05
2	667	4.07E+07	1.68	8.39E+03	3.73E-06	1.24E-02	2.70E+02	4.55E+03	10.24	1.45E+05
11	432	3.80E+07	0.46	8.10E+03	1.10E-06	2.38E-03	1.76E+02	4.75E+03	12.23	6.25E+04
12	709	3.81E+07	0.713	8.14E+03	1.68E-06	3.57E-03	1.73E+02	4.57E+03	12.44	9.86E+04
9	749	3.69E+07	0.745	8.01E+03	1.81E-06	3.70E-03	1.66E+02	4.48E+03	12.49	1.09E+05
8	1150	3.98E+07	1.14	8.36E+03	2.55E-06	5.69E-03	1.81E+02	4.48E+03	12.46	1.46E+05

Table 1-IIB										
Short Flare Configuration										
Run	Po	Ho	Po'	Uinf	Rhoinf	Pinf	Tinf	Tvinf	M	Re/ft
	psia	(ft/sec)^2	psia	ft/sec	slugs/ft^3	psia	deg. R	deg. R		
21	448	3.73E+07	1.11	7.99E+03	2.71E-06	8.17E-03	2.44E+02	4.57E+03	10.26	1.11E+05
22	604	3.90E+07	1.5	8.19E+03	3.49E-06	1.10E-02	2.56E+02	4.52E+03	10.27	1.39E+05
23	650	3.91E+07	0.675	8.23E+03	1.55E-06	3.41E-03	1.78E+02	4.68E+03	12.38	8.93E+04
18	1140	3.95E+07	1.11	8.33E+03	2.50E-06	5.56E-03	1.80E+02	4.45E+03	12.44	1.43E+05
19	772	3.71E+07	0.763	8.04E+03	1.84E-06	3.83E-03	1.68E+02	4.48E+03	12.42	1.10E+05

Table 1-III Cone/Cone Test Conditions												
Run	Po	Ho	Po'	Uinf	Rhoinf	Pinf	Tinf	Tvinf	M	Re/ft	Nose	Cone/Flare
	psia	(ft/sec)^2	psia	ft/sec	slugs/ft^3	psia	deg. R	deg. R				
28	275	4.02E+07	0.619	8.27E+03	1.41E-06	4.35E-03	2.50E+02	4.93E+03	10.50	5.83E+04	Sharp	25° /55°
26	407	4.19E+07	0.975	8.47E+03	2.12E-06	7.06E-03	2.70E+02	4.86E+03	10.34	8.35E+04	Sharp	25° /55°
24	531	4.26E+07	1.25	8.57E+03	2.66E-06	8.98E-03	2.74E+02	4.75E+03	10.38	1.04E+05	Sharp	25° /55°
35	547	4.12E+07	0.541	8.45E+03	1.18E-06	2.69E-03	1.84E+02	4.88E+03	12.49	6.74E+04	Sharp	25° /55°
32	298	4.18E-07	0.669	8.44E+03	1.47E-06	4.65E-03	2.57E+02	5.00E+03	10.53	6.01E+04	0.25" Radius	25° /55°
36	415	4.20E+07	0.993	8.48E+03	2.15E-06	7.19E-03	2.70E+02	4.86E+03	10.34	8.48E+04	0.25" Radius	25° /55°
33	512	4.34E+07	1.2	8.65E+03	2.50E-06	8.67E-03	2.81E+02	4.79E+03	10.35	9.71E+04	0.25" Radius	25° /55°
31	526	4.27E+07	0.521	8.60E+03	1.10E-06	2.62E-03	1.93E+02	4.99E+03	12.43	6.08E+04	0.25" Radius	25° /55°
37	415	4.14E+07	0.995	8.42E+03	2.19E-06	7.19E-03	2.67E+02	4.82E+03	10.35	8.67E+04	0.288" Radius	25° /55°
38	409	3.76E+07	0.405	8.05E+03	9.76E-07	2.02E-03	1.68E+02	4.73E+03	12.47	5.83E+04	0.288" Radius	25° /55°
6	251	4.00E+07	0.565	8.24E+03	1.30E-06	3.97E-03	2.48E+02	4.95E+03	10.50	5.39E+04	0.6" Radius	25° /55°
39	526	4.07E+07	0.52	8.39E+03	1.15E-06	2.58E-03	1.82E+02	4.86E+03	12.50	6.61E+04	Sharp	25° /60°
40	522	4.18E+07	0.514	8.51E+03	1.12E-06	2.57E-03	1.87E+02	4.93E+03	12.48	6.30E+04	0.25" Radius	25° /60°

Part 2 – Experimental Studies of Jet and Shock Interaction Phenomena Associated with Ramjet and Scramjet Propulsion in Hypervelocity Flows

Abstract

Experimental studies have been conducted in the LENS I shock tunnel to investigate the characteristics and performance of full-scale scramjet engines at fully duplicated flight conditions for a range of dynamic pressures at Mach 7. In this program we employed a generic engine, the flow path of which was configured to be similar to the Air Force Hy-Tech configuration for studies with hydrocarbon and hydrogen fuels. In this section of the final report, we first discuss some of the key flow phenomena, which must be correctly replicated in the experimental studies of scramjet engines to obtain accurate results. We then review a number of experimental programs conducted in our tunnels to investigate boundary layer transition, shock/shock and shock/boundary interaction, surface cooling and mixing and combustion associated with scramjet performance. We also describe the operation and performance of the LENS I and II hypervelocity test facilities with emphasis on their application to scramjet testing for fully duplicated flight conditions. Measurements are presented from calibration and validation studies conducted under extremely high pressure and high enthalpy conditions required for scramjet testing at Mach 12. We then present results from an experimental program conducted to examine hydrogen and hydrocarbon-fueled scramjet engine performance for a velocity of 7,000 ft/sec and dynamic pressures up to 3,000 psf. In this program we used a new generic engine, the flow path of which has been configured to represent the Mach 7 configuration of the Air Force Flight Dynamics Laboratory's Hy-Tech engine, which was highly instrumented with heat transfer and pressure gages on the compression ramp, isolator, combustor, and nozzle sections to provide detailed aerothermal, aero-acoustic and propulsion measurements. High-speed Schlieren and infrared imagery were employed to examine the structure of the flowfield through the engine. Here, we discuss the general results from these studies. The detailed measurements made in this program will be presented under more restricted conditions at the JANNAF April 2002 meeting.

Introduction

The flow over a scramjet powered hypersonic vehicle is replete with flow phenomena, which have proven to be extremely difficult to describe and model in the prediction schemes used in engine and vehicle design. Some of these fluid dynamic, real-gas and combustion phenomena are illustrated in Figure 69. To predict the performance of the engine inlet compression ramp it is necessary to model the effects of flowfield chemistry, surface pressure gradients and surface temperature on the structure of the transition region. Because boundary layer trips will be employed to obtain turbulent flow into the isolator, it is important to understand how to design trips that will not significantly distort the flow into the engine, or introduce "hot spots" on the engine cowl or sidewalls. It is also of key importance to obtain detailed information on the shock/shock and shock/boundary layer interaction regions on the cowl lip and engine

sidewalls to develop prediction techniques to calculate the large aerothermal loads generated in these regions. We also need to understand how the turbulent boundary on the compression ramp influences the transition front developed on the engine sidewalls and the cowl, for this information is critical in predicting the structure of the shock interaction regions, which occur on these sections of the engine. However, the principal task in an experimental study of scramjet performance is to obtain detailed measurements of the mixing and combustion of the fuel in the injector and combustor section of the engine to be used to validate injector design methods and assess engine performance. It is critical to obtain measurements that accurately describe the nonequilibrium flow chemistry and relaminarization effects, where the nonequilibrium expansion over the nozzle is, of course, of key importance in developing the propulsive thrust. In order to obtain these measurements, it is essential to employ advanced hypervelocity testing facilities that can operate at high pressures and energy levels that produce clean, high quality and well-defined airflows. To replicate the intrinsic characteristics of nonequilibrium air chemistry coupled with turbulent mixing and combustion, it is important to conduct studies of flow phenomenology and engine performance at duplicated flight conditions with full-scale vehicle components. The geometry of the Generic Scramjet Engine (GSE) can be adapted to closely match the of contemporary scramjet designs for the Hyper-X and ARRMD vehicles (Figure 70) where, fortunately, these engines can be tested full scale in the LENS facilities at duplicated flight conditions.

During the NASP program a number of important experimental studies were conducted in our shock tunnel facilities to obtain measurements of fundamental flow phenomena associated with scramjet performance for the purpose of providing data with which to construct and evaluate prediction techniques employed in the design of hypersonic air-breathing vehicles. Detailed studies were performed to examine the aerothermal characteristics of the NASP vehicles, its forebody compression surfaces, and the scramjet engine (Ref. 23) with models shown in Figure 71. "Building Block" studies were also conducted (Refs. 24 to 31) to examine the characteristic regions of: shock/shock and shock/boundary layer interaction; film and transpiration cooling techniques; boundary layer transition on compression ramps leading edges and in regions of high cross flow; and relaminarization in regions of strong expansion. The models employed in these later studies are shown in Figure 72. These programs have provided valuable insight into the important problems that must be addressed in scramjet-powered vehicle design and form a valuable base for the current studies.

In one of the studies referred to above, the NASP engine was tested in a semi-direct mode as illustrated in Figures 73 and 74. A photograph of the engine installed in the test section of the LENS I facility is shown in Figure 75. The engine was highly instrumented with high frequency pressure and heat-transfer instrumentation as illustrated in Figure 76. High-speed Schlieren photography was employed to observe the structure of the flowfield inside the engine through ports in the injector and combustor section of the model. These photographs provide graphic evidence of the unsteady shock structure generated in the injector and combustor regions in the engine. We found that holograph interferometry producing interferograms (similar to that shown in Figure 77) can be

21

successfully employed to visualize these flows. Heat transfer and pressure records through the engine, similar to those shown in Figure 78, demonstrated that the flow was fully-established within two milliseconds from flow initiation through the combustor. Comparisons between measurements and calculations by Dash et al shown in Figure 79 (from Ref. 32) suggest that the computation captured many of the important features of the flow in the engine. The measurements made in this test series provide one of the most important sets of data to examine scramjet engine performance at the Mach 12 conditions produced during the NASP program.

In the following section, we review the design and performance of the LENS I and II facilities and their capability to generate high-quality, hypervelocity flows for scramjet testing at speeds from 4,000 to 14,000 ft/sec. We then describe the models and instrumentation that are being employed in an experimental program to examine the characteristic performance of a generic scramjet engine configured to provide measurements for hydrogen-fueled designs at Mach 10 and hydrocarbon-fuel configurations at Mach 7. The measurements made in the first phase of this program to investigate the aerothermal characteristics of the tripped and untripped flow over the compression ramp, closed cowl plate and engine sidewalls of the closed cowl Hyper-X configuration are then presented.

Hypervelocity Facilities For Scramjet Studies

Facility Requirements

As discussed previously, evaluating scramjet engines designed for operation at hypersonic speeds requires the use of facilities with clean airflows in which the velocity, density and temperature in the engine are fully duplicated flight conditions. Nonequilibrium flowfield chemistry is an intrinsic feature of these flows, as illustrated in Figure 80, for temperatures approaching 8,000°R, which will be generated in stagnation regions and in the boundary layer close to the wall at the Mach 12 conditions. It is clear from Table 2-I that currently only in shock tunnels is it possible to obtain clean uncontaminated air at the temperatures and pressure required for scramjet testing above Mach 8. Additional requirements for full-scale testing, besides the size of the facility, are a large uniform test core generated by a well-designed contoured nozzle, and test times which will produce at least three flow lengths over the entire vehicle and ten flow lengths through the engine that are required to stabilize the complex shock/boundary layer interaction regions occurring in the engine. The 8 mS test time available in the LENS I facility at Mach 12 provides a flow length of close to 100 ft; equivalent to 30 engine lengths, or eight vehicle lengths of flow – easily sufficient to satisfy these requirement. Although testing at large reservoir pressures has its advantages in decreasing the levels of freestream dissociation (O of less than 1% in LENS facility at Mach 12), as discussed below, these large pressures result in turbulent flow and large aerothermal loads in the reservoir and throat section of the tunnel .The velocity/altitude map for the LENS I and II facilities are shown together with those from conventional blowdown facilities in Figure 20. While AEDC-9 comes the closest to simulating hypervelocity conditions, it cannot be used for real-gas and combustion studies because N_2 is employed as the test gas. For the more restricted situation where only Mach number/Reynolds number simulation is

required, the high-pressure capabilities of the LENS facilities are reflected in high unit Reynolds number, as shown in Figure 81.

LENS I and II Hypervelocity Facilities

The layout of facilities supporting Legs I and II of the LENS Facility are shown schematically in Figure 19. Both facilities share a common control room, compressor system, vacuum system, ballast tank, and data recording and analysis systems. A photograph of the test section, nozzle and driven sections of the LENS I and II shock tunnels are shown in Figure 17. The LENS Leg I shock tunnel has a 60-foot, 13-inch OD driven tube and a 25-foot long driver section, which is electrically heated. Nitrogen, helium and hydrogen can be employed as driver gases allowing tailored interface operations up to a velocity of 14,000 ft/sec. The LENS I facility has two contoured nozzles allowing it be operated over a range from Mach 7 to 18. Test times of 24 and 4 milliseconds can be obtained at velocities from 3,000 to 15,000 ft/sec, respectively. LENS Leg II has a 30-inch ID driven tube, which is 90 feet in length, coupled to a heated driver section of 40 feet in length through a large double diaphragm valve. This facility currently has a single nozzle that operates at Mach numbers between 4 and 5; however, it is designed to operate over a Mach number range from 2.5 to 7 under duplicated enthalpy conditions. LENS Leg II can fully duplicate the flow at altitudes from 30 km down to sea level. Test times of up to 50 milliseconds can be obtained when the facility is operated as a shock tunnel or close to 1/10 second when the facility is operated as a Ludweig Tube. Both LENS Leg I and Leg II are operated under tailored interface conditions by carefully controlling the operating parameters and the gases employed in the driver and driven tubes.

A schematic diagram of the operation is shown in Figure 15. Flow is initiated through the tunnel by venting the center section of the double diaphragm valve. A strong shock generated by this sudden opening travels down the driven tube and is reflected from the end wall. As the reflected shock travels back down the driven tube, it creates a reservoir of high-pressure, high-temperature gas. We operate the tunnels such that when the reflected shock strikes the interface between the driver and driven gases the contact surface is brought to rest, with absence of reflected expansion or compression waves. The reservoir of hot stationary gas between the end wall and the contact surface is then exhausted through the throat into the test section in a manner similar to that which occurs in conventional blowdown tunnels. In both LENS I and II, the steady test time is limited by the return of the expansion fan from the driver section. The flow through the tunnel is terminated in the tunnel when a valve closes the throat of the tunnel.

The Mach 8 and 14 nozzles for LENS Leg I have exit plane diameters of 44 and 48 inches, respectively, which allow the installation of models of up to 24 inches in diameter and 12 feet long. LENS Leg II, as shown in Figure 17, is equipped with a Mach 4.5 contoured nozzle that has an exit plane of 44 inches in diameter. This all-metal nozzle has typical throat diameters of 10 inches. The LENS Leg II is also capable of duplicating flight conditions up to Mach 7, and it is planned to add a Mach 6 to 7 nozzle with an exit plane of 72 inches for future tests of missile performance. As illustrated in Figure 82, by operating at reservoir pressures of up to 2,000 atms, the LENS I can duplicate flight

conditions up to Mach 12 in the freejet testing mode. One of the first high-enthalpy programs conducted in the LENS I test facility was scramjet testing with an engine configuration similar to that used in the NASP program. This work was preceded by an extensive facility development program to provide a test capability that could operate cleanly at reservoir pressures of up to 2,000 atm and stagnation temperatures of over 12,000°R. These conditions generated very large heating rates on the reservoir end wall and throat region of the tunnel, principally because the boundary layers there were turbulent. This demanded the use of high temperature/high conductivity materials in the reflected shock and throat region of the tunnel, as well as the use of a fast-acting valve to close the throat at the end of the useful test time. Only with the extensive application of sophisticated materials and construction techniques was burning prevented in these sections of the tunnel. It may be extremely difficult to obtain clean airflows for much longer than 10mS at these stagnation temperatures and pressures. We were successful in generating clean Mach 12 test conditions with test times of over 8 milliseconds.

Our earlier scramjet testing was preceded by flowfield calibration measurements and computations employing the GASP code. The development of diagnostic instrumentation to provide accurate measurements in this high enthalpy environment also presented a significant challenge. Figure 83 shows comparisons between our measurements of Mach number and density distribution and computations with the GASP code. Here the experimental values were deduced from survey rakes containing pitot pressure, total heat transfer and static pressure cone probes, and clearly at these conditions the free-stream density is a highly sensitive quantity. Additional flowfield predictions are shown in Figure 84 for our "D nozzle". Measurements of the reservoir and static pressure traces for full duplication at Mach 8,10 and 12 test conditions are shown in Figures 85, 86, and 87 which illustrate that we have up to 10 mS of steady test flow in which to evaluate scramjet performance.

Summary of Results from Mach 7 Scramjet Studies

Introduction

In this part of the program, we examined shock interaction phenomena associated with the performance of the hydrocarbon-fueled scramjet engine at Mach 7 for dynamic pressures between 1,000 and 2,000 psf. The model configuration selected for these studies (see Figure 88) was based on the Hy-Tech engine configuration as employed in studies at Wright-Patterson Air Force Base by Gruber and Jackson (Ref. 33). We selected the cavity configuration (shown in Figure 89) from these studies. We also employed flush-mounted wall injectors (Figure 89) with injection angles of 15° as employed at Wright Field in earlier studies. The specific injector spacings and geometry of the combustor were arrived at in consultation with Joe Schetz (Ref. 34) and members of the Wright Field Propulsion Branch. In our studies, however, we employed three hydrogen-oxygen fueled igniters spaced across the rear face of the step and angled into the shear. The overall flow configuration shown in Figure 90 is significantly longer than the hydrogen-fueled engine tested earlier to accommodate the slower burning hydrocarbon fuel. In these studies, however, we employed both ethylene and hydrogen in order to

24

examine the relative performance of these fuels and assess the relative performance of the mixing/combustion characteristics of these fuels.

Measurements in Shock Interaction Regions on Engine Inlet

Schlieren photographs of the flow on the third ramp just ahead of the inlet for tests with and in the absence of boundary layer trips are shown in Figure 91. Here we observe for the flow in the absence of the trips the laminar boundary layer is beginning to transition just downstream of the beginning of the third ramp. In contrast, in Figure 91b, we see that the boundary layer is fully turbulent on the second ramp when trips are employed. This photograph also shows that the boundary layer trips introduce shock waves into the flowfield just above the shock from the junction between the first and second ramps. The difference in flow structure between the tripped and untripped flows is shown more vividly in pulsed holograms of the flow presented in Figures 92a and b. Here it is clear that the transition process is generating a series of traveling instabilities which form large scale eddies in the flows on the third ramp in the absence of boundary layer trips. A well-developed turbulent boundary layer is evidenced by the well-defined structures for the inlet flow with trips as shown in Figure 92b. Infinite fringe holograms of the flowfield which enable us to determine the distribution of density through the flowfield entering the engine are shown in Figures 93a and b, again for the flows with and in the absence of boundary layer trips. Here it is clear that the trips significantly thicken the boundary layer and generate a different density distribution near the wall.

During the initial running we positioned pitot pressure and total temperature rakes at the inlet to the engine as shown in Figure 94. A comparison between the measured pitot pressure distributions just ahead of the engine inlet and Navier-Stokes calculations of the forebody flow are shown in Figure 95 demonstrates good agreement in the outer inviscid flow for both the tripped and untripped engine configurations (Ref. 35). However, possibly as a result of the complex flow generated in and above the viscous layer by the trip shocks, the agreement with predictions are not as good in this region. Employing these measurements together with the density distributions determined from the interferograms, we can estimate the mass capture to the engine. Also, since the shock from the leading edge passes very close to the cowl lip as shown in Figure 95, we can also easily determine mass capture from simple inviscid flow relationships.

Shock Interaction Phenomena Occurring in the Engine

A typical Schlieren photograph obtained from a sequence of high-speed video through the flow of the engine is shown in Figure 96. Both the high-speed Schlieren photograph and surface measurements demonstrated that the flow through the engine was fully established in 2 milliseconds and the flow through the engine for the remaining 7 milliseconds of the run was extremely stable. The Schlieren photographs show that the flowfield is dominated by oblique shocks, which have been transmitted through the isolator section from the forebody.

As in the earlier studies, we employed pressure and heat transfer measurements throughout the engine to provide information on the detailed characteristics of the performance of each section of the engine and integrated these measurements to provide

indications of the thrust of these engines. Infrared photography and spectrograph measurements were also employed to provide qualitative and quantitative measurements of the size and properties of the combustion region. This data was obtained by looking obliquely up from the rear of the combustor from windows in the side of the engine. A typical infrared photograph of the burning around a specific injector is illustrated in Figure 97.

Typical distribution of heat transfer for the combustion and tare runs through the engine is shown in Figure 98. Here we see that when combustion occurs there is a significant increase in heating and this increase continues all the way into the nozzle. Likewise, combustion is observed in the pressure distribution by a rapid increase which is again maintained through the combustor and into the nozzle. In order to assess the performance of the engine, we examined the pressure and skin friction drag and the thrust for each component of the engine sectioned in the manner shown in Figure 99. From the detailed measurements of heat transfer obtained through the engine and employing a Reynolds analogy factor suggested from computations, we can construct a thrust/drag balance similar to that shown in Figure 99. Here we see that the engine developed positive thrust and a contribution of the thrust resulting from the injected fuel is of importance.

CONCLUSIONS

During the past five years, we have developed two new powerful ground test capabilities and their associated models and instrumentation, to examine scramjet engine performance at duplicated flight conditions from Mach 4 to 12 at altitudes from 10 kft to 120 kft for full scale interceptor engines. This capability has been used to investigate key aerothermal, aero-acoustic, and air-combustion chemistry phenomena which are associated with the design and performance of a generic scramjet engine configured with a flowpath similar to those for the Hy-Tech engine which was tested at Mach 7 with hydrocarbon and hydrogen fuels. In this program we obtained measurements to quantify the characteristics of the transitional flow, mixing and combustion, and unsteady shock interaction phenomena associated with scramjet performance and to aid in the construction of the models employed in the codes to predict the aerothermal and aero-acoustic loads and combustion efficiency. These studies were built on our earlier investigations of scramjet engine performance from Mach 8 to 12; fundamental studies of boundary layer transition, shock/shock and shock/boundary interaction, and film- and transpiration-cooling during the NASP and Hyper-X programs. This work provided important experimental data and correlations with which to evaluate scramjet engine design and the associated numerical prediction tools. In the current program, we investigated complete engine performance for an engine configured with wall injectors and cavity flame holders similar to those employed in the fundamental test programs conducted at ARL during the Hy-Tech program. Detailed measurements of heat transfer and pressure were obtained on the inlet, isolator, combustor, and nozzle sections of the full-scale complete engine configuration. High-speed Schlieren and infrared imaging were employed to examine the flow structure through the engine. During this program we also investigated the effects of fuel temperature and the addition of xylene. This program

26

yielded fundamental measurements with which the semi-empirical and full-scale Navier-Stokes computations can be compared. By employing the detailed measurements of heat transfer and pressure throughout the engine, coupled with analysis to determine the skin friction from these measurements, we were able to determine the drag and thrust levels throughout the engine to estimate the total thrust of the engine.

TABLE 2-1 – GROUND TEST WIND TUNNEL FACILITIES FOR HYPERSONIC VEHICLE RESEARCH

	Continuous Time ~ 1 min	Intermittent Time ~ 1 – 20 sec	Short Duration Time ~ 5 – 100 mS	Pulse Less than 1 mS
	Heat Exchanger	Visciated or Pebble-Bed Heated Gas	Ludweig/Shock Tunnels	Piston-Driven Shock Tunnels
Maximum Reynolds Number at Mach 8	10^6	10^7	10^8	10^6
Stagnation Temperature/ Velocity	2,000° R/ 2,000 ft/sec Electrical	4,000°R/ 5,000 ft/sec Electrical/ Combustion	15,000°R 14,500 ft/sec Shock Heated	25,000°R 28,000 ft/sec Shock Heated
Test Gas	Air	N_2/Visciated Air	Air / N_2	N_2 / Components Of Air
Boundary Layer Condition	Laminar/ Transitional	Transitional/ Turbulent → Mach 10	Turbulent → Mach 13	Laminar/Transitional
Combustion and Reacting Jet	No	For Visciated Air Facilities	Yes	Yes
Test Section Dimension	3 ft	8 ft	8 ft	2 ft

References

1. Chanetz, B., R. Benay, J-M. Bousquet, R. Bur, T. Pot, F. Grasso, and J.N. Moss, "Experimental and Numerical Study of the Laminar Separation in Hypersonic Flow," Aerospace Science and Technology, No. 3, 1998, pp. 205-218.

2. Olejniczak, J., Candler, G.V., "Computation of Hypersonic Shock Interaction Flow Fields," 7th AIAA/ASME Joint Thermophysics and Heat Transfer Conference, AIAA Paper 98-2446, June 1998.

3. Gnoffo, Peter, private communication, 1999.

4. Holden, Michael, "Shock Interaction in Hypersonic Flows," AIAA Paper 98-2751, presented at 29th Plasmadynamics and Laser Conference, Albuquerque, NM, June 15-18, 1998

5. Holden, Michael S. and Wadhams, Timothy P., "Code Validation Study of Laminar Shock/Boundary Layer and Shock/Shock Interactions in Hypersonic Flow, Part A: Experimental Measurements", AIAA 2001-1031, 39th Aerospace Sciences Meeting & Exhibit, January 8-12, 2001, Reno. NV.

6. Harvey, John K., Holden, Michael S., and Wadhams, Timothy P., "Code Validation Study of Laminar Shock/Boundary Layer and Shock/Shock Interactions in Hypersonic Flow, Part B: Comparison with Navier-Stokes and DSMC Solutions," AIAA 2001-1031, 39th Aerospace Sciences Meeting & Exhibit, Reno, NV, January 8-12, 2001.

7. Candler, Graham V., Nompelis, Ioannis, Druguet, Marie-Claude, Boyd, Iain D., Wang, Wen-Lan, Holden, Michael S., "CFD Validation for Hypersonic Flight: Hypersonic Double-Cone Flow Simulations," AIAA 2002-0581, presented at 40th Aerospace Sciences Meeting & Exhibit, January 13-17, 2002, Reno, NV.

8. Gnoffo, Peter, Private Communication, 2001.

9   Hall, J.G., and Treanor, C.E., "Non-equilibrium Effects in Supersonic Nozzle Flows," CAL Report No. CAL-163, March 1968.

10. Boudreau, Albert H., "Characterization of Flow Fields in Hypersonic Ground Test Facilities," Methodology of Hypersonic Testing, Lecture Series 1993-03, von Karman Institute for Fluid Dynamics, pp. 4-1 –4-15.

11 Millikan, R.C. and White, D.R, "Systematics of Vibrational Relaxation," Journal of Chemical Physics, Vol. 39, 1963, pp. 3209-3213.

12. Lordi, John, private communication, 2001-2002.

13. Lordi, J.A., Mates, R.E. and Moselle, J.R., "Computer Program for the Numerical Solution of Nonequilibrium Expansions of Reacting Gas Mixtures," Cornell Aeronautical Report No. AD-1689-A-6, NASr-109, October 1965

14. Candler, G.V., Nompelis, I., Druguet, M-C., "Navier-Stokes Predictions of Hypersonic Double-Cone and Cylinder-Flare Flow Fields," AIAA Paper No. 2001-1024, January 2001, AIAA 39th Aerospace Sciences Meeting & Exhibit, Reno, NV, January 8-12, 2001.

15. Boyd, I.D., and Wang, W-L, "Monte Carlo Computations of Hypersonic Interacting Flows," AIAA Paper No. 2001-1029, 39th Aerospace Sciences Meeting and Exhibit, Reno, NV., January 8-12, 2001.

16. Cheng, H.K., Hall, J. Gordon, Golian, T.C., and Hertzberg, A., "Boundary Layer Displacement and Leading Edge Bluntness Effects in High-Temperature Hypersonic Flow," *Journal of the Aerospace Sciences,* Vol. 28, No. 5, May 1961. Also presented at Hypersonic Phenomena Session, IAS 28th Annual Meeting, NY, Jan. 25-27, 1960.

17. Gaitonde, Datta V., "Evaluation of Flux-Split Schemes in Laminar Hypersonic Flows," oral presentation, Reno, NV, January 2001.

18. Gnoffo, Peter, "CFD Validation Studies for Hypersonic Flow Prediction," AIAA 2001-1025, 39th Aerospace Sciences Meeting and Exhibit, Reno, NV, January 8-12, 2001.

19. Moss, James, "DSMC Computations for Regions of Shock/Shock and Shock/Boundary Layer Interaction," AIAA 2001-1027, 39th Aerospace Sciences meeting and Exhibit, Reno, NV, January 8-12, 2001.

20. Roy, Christopher J., Gallis, Michael A., Payne, Jeffrey L., and Bartel, Timothy J., "Navier-Stokes and DSMC Simultions for Hypersonic Laminar Shock/Shock Interaction Flows," presented at the AIAA 40th Aerospace Sciences Meeting and Exhibit, Reno, NV, January 14-17, 2002.

21. Gallis, M., Roy., C., Payne, J. and Bartel, T., "DSMC and Navier-Stokes Predictions for Hypersonic Laminar Interacting Flows," AIAA 2001-1030, 39th Aerospace Sciences Meeting and Exhibit, Reno, NV., January 8-12, 2001.

22. Kato, H. and Tannehill, J., "Computation of Hypersonic Laminar Separated Flows using an Iterated PNS Algorithm," AIAA 2001-1028, 39th Aerospace Sciences Meeting and Exhibit, Reno, NV, January 8-12, 2001.

23. Holden, M.S., Chadwick, K.M., and Kolly, J.M., "Hypervelocity Vehicle and Combustion Studies in the LENS Facility," paper presented at the 1995 JANNAF Airbreathing Propulsion Subcommittee Meeting, MacDill Air Force Base, Tampa, FL, December 5-8, 1995.

24. Holden, M.S., "Heat Transfer and Pressure Measurements in Transitional and Turbulent Hypersonic Flows Over Curved Compression Surfaces," Report Number 2610-2, Contract F33601-89-D-0045, prepared for University of Dayton Research Institute, May 1994.

25. Holden, M.S., "Experimental Studies of Transpiration Cooling With Shock Interaction in Hypersonic Flow," Final Report Part B, Grant Number NAG 1-790, prepared for NASA Langley Research Center, May 1994.

26. Holden, M.S., Bower, D.R., and Chadwick, K.M., "Measurements of Boundary Layer Transition On Cones at Angle of Attack for Mach Numbers from 11 to 13," Report Number 2610-4, Contract F33601-89-D-0045, prepared for University of Dayton Research Institute, May 1994.

27. Holden, M.S. and Sweet, S. J., "Studies of Transpiration Cooling With Shock Interaction in Hypersonic Flow," AIAA-94-2475, Paper presented at the 18th AIAA Aerospace Ground Testing Conference, Colorado Springs, CO, June 20-23, 1994.

28. Holden, M.S., Kolly, J.M., and Bower, D.R., "Attachment-Line Transition Studies on Swept Cylindrical Leading Edges at Mach Numbers From 10 to 12," Report Number 2610-6, Contract F33601-89-D-0045, prepared for University of Dayton Research Institute, July 1994

29. Holden, M.S., and Chadwick, K.M., "Experimental Studies of Relaminarization in Highly Expanding Hypersonic Flows," Report Number 2610-7, Contract F33601-89-D-0045, prepared for University of Dayton Research Institute, July 1994.

30. Holden, M.S., Bower, D. R. and Chadwick, K.M., "Measurements of Boundary Layer Transition on Cones at Angle of Attack for Mach Numbers from 11 to 13," AIAA 95-2294, paper presented at the 26th AIAA Fluid Dynamics Conference in San Diego, CA, June 19-22, 1995.

31. Holden, Michael, Sweet, Shirley, Kolly, Joseph, and Smolinski, Gregory, "A Review of the Aerothermal Characteristics of Laminar, Transitional and Turbulent Shock/Shock Interaction Regions in Hypersonic Flows," AIAA 98-0899, presented at the 36th Aerospace Sciences Meeting and Exhibit, Reno, NV, January 12-15, 1998.

32. Dash, S.M., Perrell, E.R., Hosangadi, A., Ungewitter, R., Cavallo, P.A., Kenzakowski, D.C., Seiner, J., and Holden, M., "Missile Flowfield Modeling Advances and Data Comparisons," paper presented at the 38th Aerospace Sciences Meeting & Exhibit, Reno, NV, AIAA 2000-0940, January 10-13, 2000.

33. Mathur, T., Streby, G., Gruber, M., Jackson, K., Donbar, J., Donaldson, W., Jackson, T., Smith, C. and Billig, F., "Supersonic Combustion Experiments with a Cavity Based Fuel Injector," Paper AIAA 99-2102, presented at the 35th AIAA/ASME/SAE/ASEE Joint Propulsion Conference and Exhibit, Los Angeles, CA, June 20-24, 1999.

34. Private Communication, Joseph Schetz, 2001

35. Private Communication, Paul Ferlemann, 2001

Publications:

Holden, M.S. and Walker, B.J., "A Review of Recent Development, Testing and Code Validation Studies in the LENS Facility," AIAA 96-4598, presented at the 7th

International Space Planes and Hypersonic Systems and Technologies Conference, Norfolk, VA, November 18-22, 1996.

Holden, Michael S., "Measurements in Laminar Regions of Shock/Shock and Shock/Boundary Layer Interaction over Cylindrical Leading Edges, Cone/Cone and Hollow Cylinder Flare Configurations for DSMC/Navier-Stokes Code Validation," presented at the 22nd International Symposium on Rarefied Gas Dynamics, Sydney, Australia, July 9-14, 2000.

Holden, Michael S., "Studies of Scramjet Performance in LENS Facilities," Paper 2000-3604, presented at the 36th AIAA/ASME/SAE/ASEE Joint Propulsion Conference, July 17-19, 2000, Huntsville, AL.

Holden, Michael S., "Studies of Scramjet Performance in the LENS Facilities," presented at the Joint-Army-Navy-NASA-Air Force (JANNAF) CS/APS/PSHS Joint Meeting, Monterey, CA, 13-17 November, 2000.

Holden, Michael S. and Wadhams, Timothy, P., "Code Validation Study Of Laminar Shock/Boundary Layer And Shock/Shock Interactions In Hypersonic Flow Part A: Experimental Measurements," AIAA Paper 2001-1031, presented at the 39th AIAA Aerospace Sciences Meeting and Exhibit, Reno, NV, January 8-12, 2001.

Harvey, John K., Holden, Michael S., and Wadhams, Timothy P., "Code Validation Study of Laminar Shock/Boundary Layer and Shock/Shock Interactions in Hypersonic Flow. Part B: Comparisons with Navier-Stokes and DSMC Solutions," AIAA Paper 2001-1031, presented at the 39th AIAA Aerospace Sciences Meeting and Exhibit, Reno, NV, January 8-12, 2001.

Holden, Michael S., Wadhams, Timothy P., Harvey, John K., and Candler, Graham V., "Comparisons Between DSMC and Navier-Stokes Solutions on Measurements in Regions of Laminar Shock Wave Boundary Layer Interaction in Hypersonic Flows," AIAA Paper 2002-0435, presented at the 40th AIAA Aerospace Sciences Meeting and Exhibit, Reno, NV, January 14-17, 2002.

Acknowledgment / Disclaimer
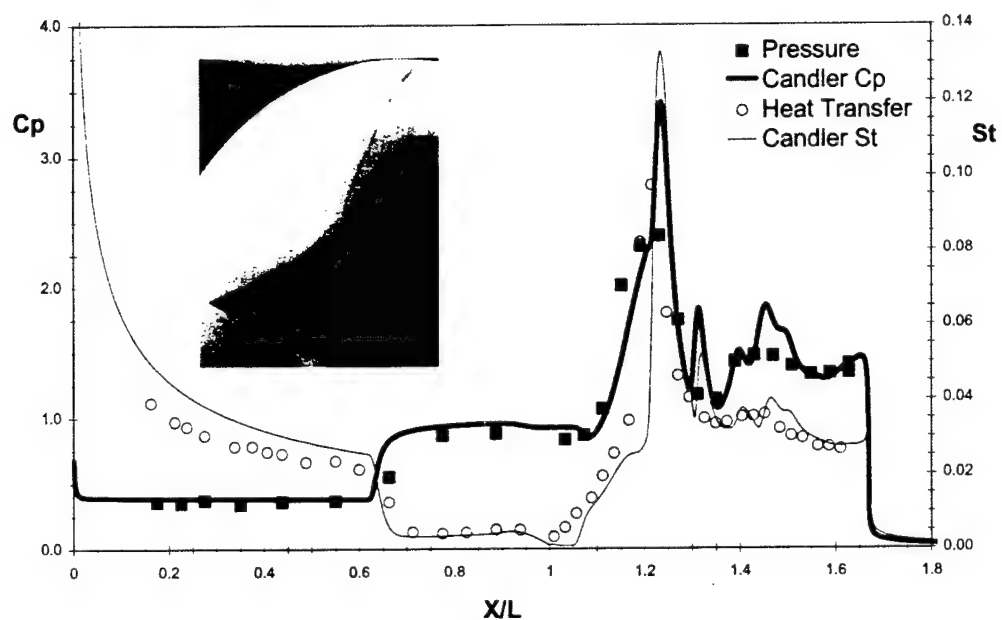
Figure 1   Comparison between Heat Transfer and Pressure Measurement on Double Cone Model and Navier-Stokes predictions by Candler (Ref. 7)

Figure 2   Composite Picture Showing Density Contours from Candler's Solution for the Biconic Model Superimposed on a Schlieren image. (Run 24)
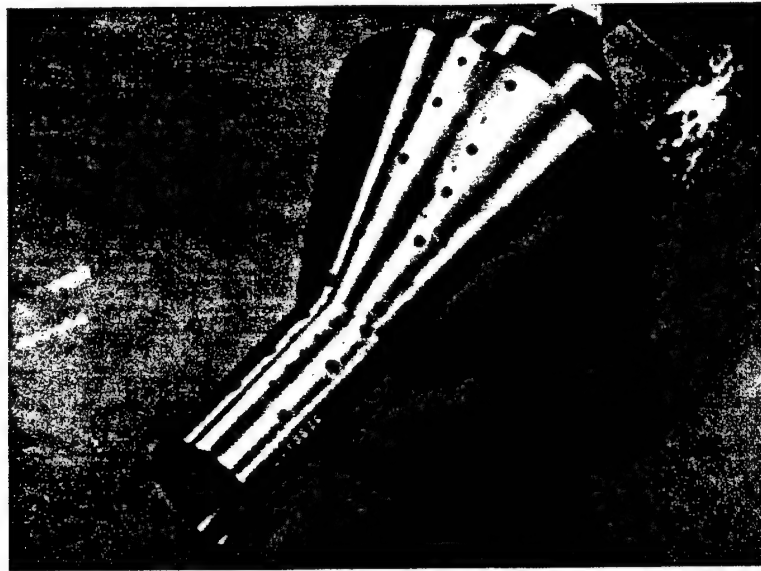
Figure 3 Photograph of the Cylinder/Extended Flare Model
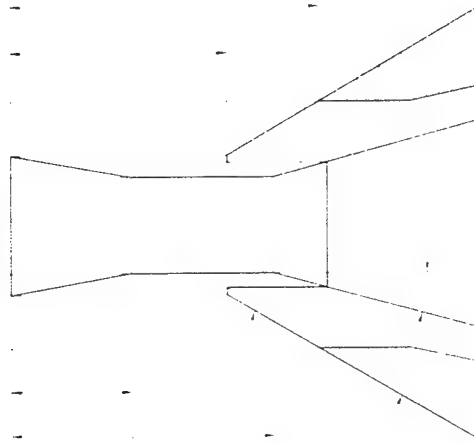
Figure 4   Dimensions for Two Cylinder Flare Configurations employed in the Experimental Studies

Heat Transfer

Pressure
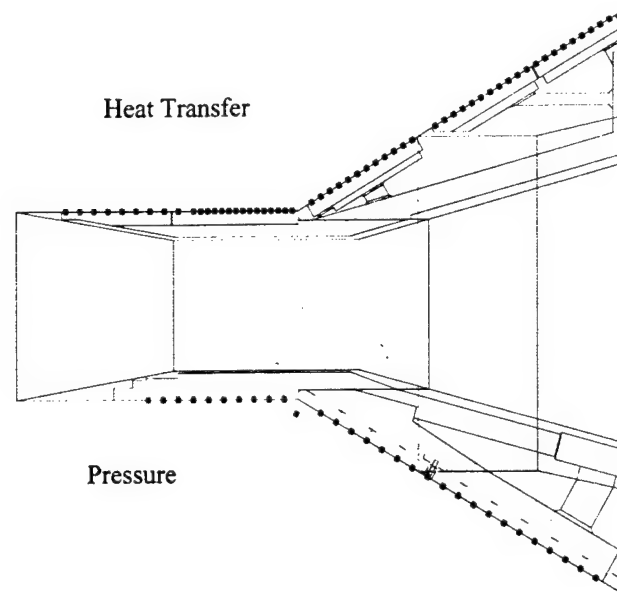
Figure 5 Instrumentation Layout on Cylinder/Flare Models
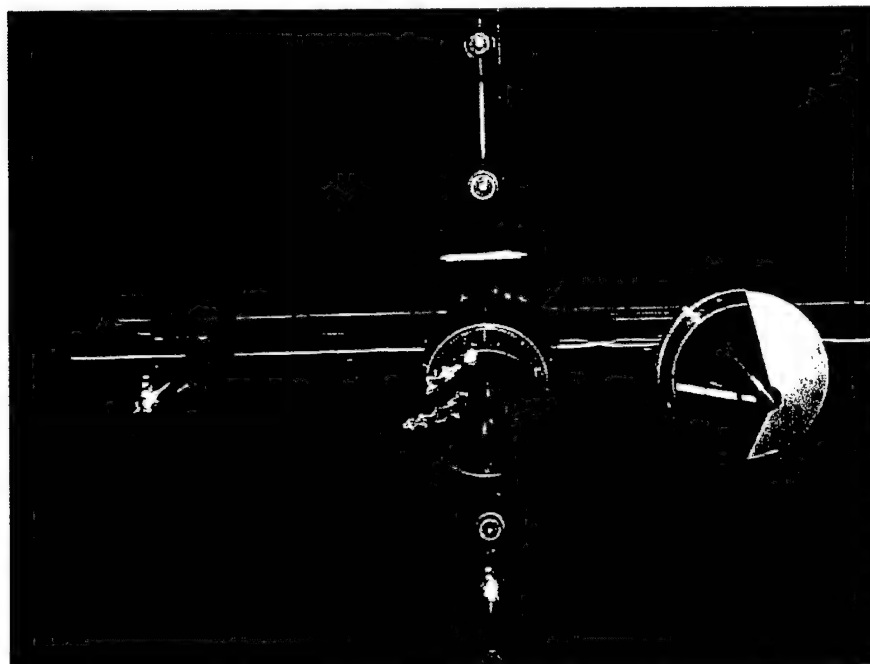
Figure 6 Hollow Cylinder Model supported in Flowfield Rake Assembly
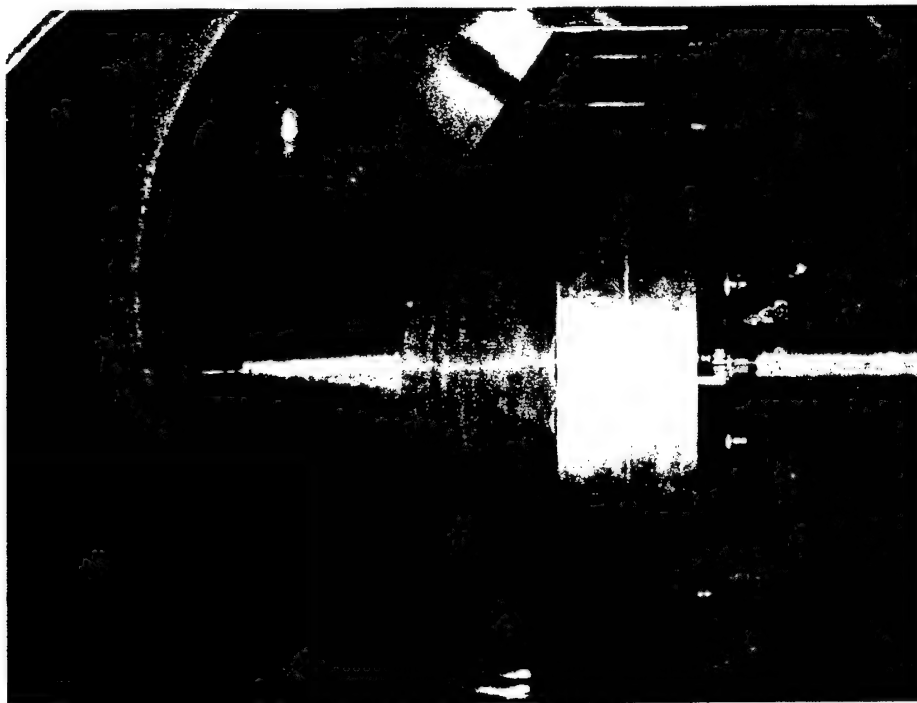
Figure 7   Photograph of Double Cone Model in LENS I Tunnel
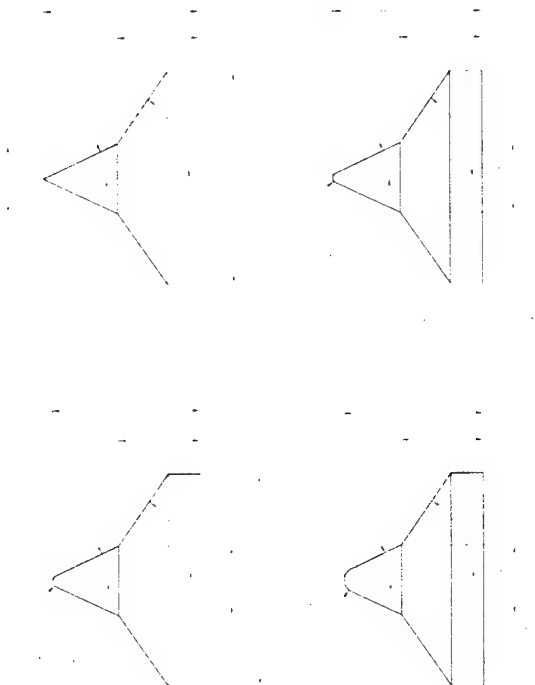
Figure 8   Sharp and Blunt 25°/55° Double Cone Configurations
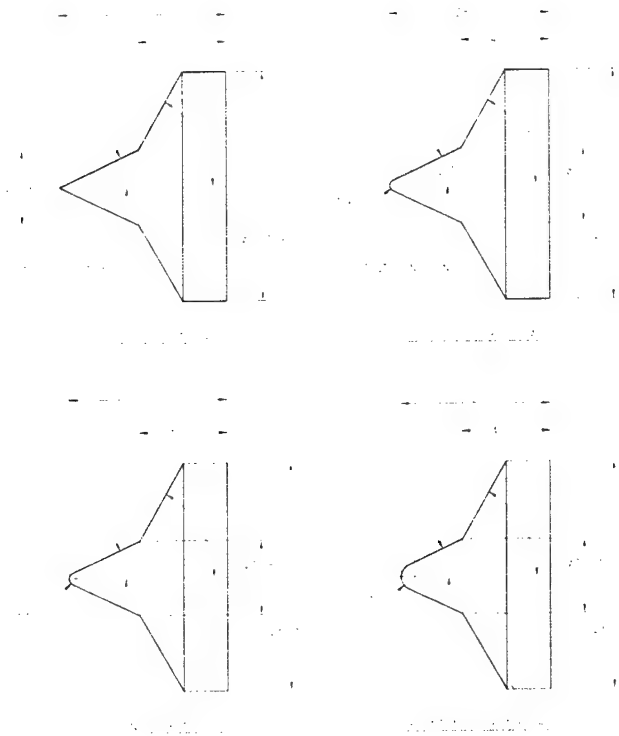
Figure 9 Sharp and Blunt 25°/60° Double Cone Configurations

55° FLARE HEAT TRANSFER GAGES
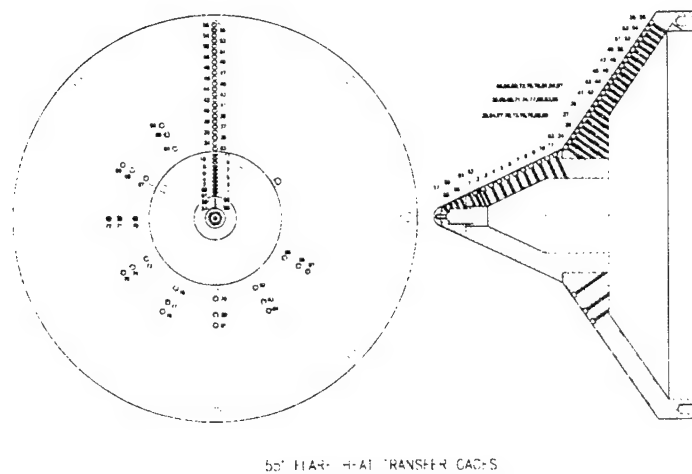
Figure 10 Distribution of Heat Transfer Gages on Double Cone Model
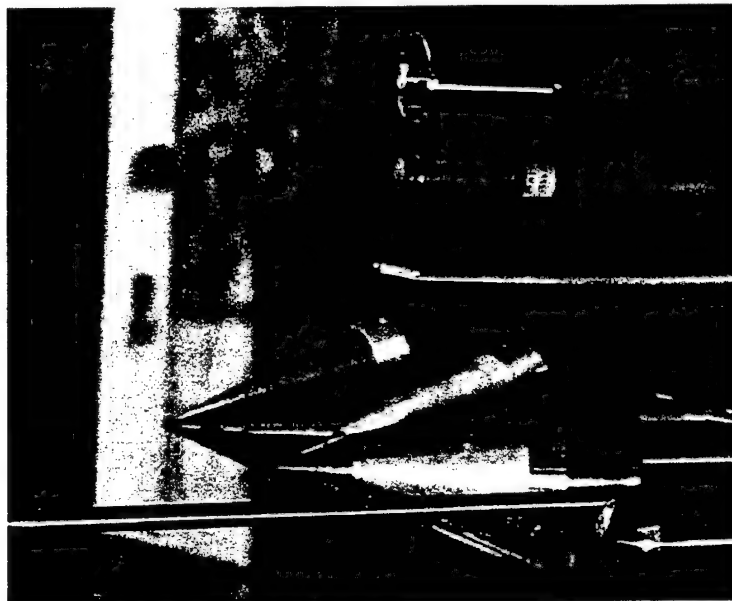
Figure 11 Two 25° Cone Models in Survey Rake for "Vibrational Nonequilibrium" Studies
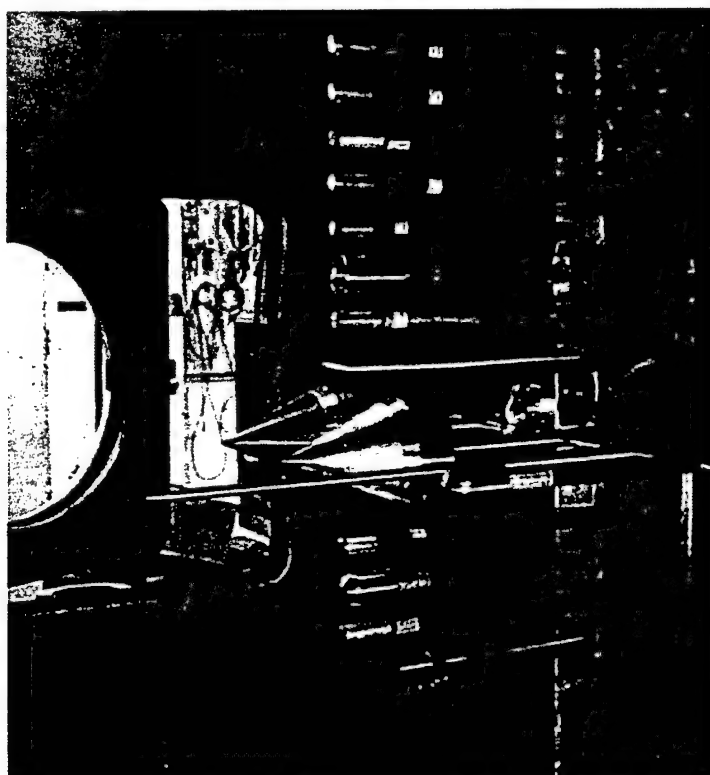
Figure 12 Survey Rake containing Pressure, Heat Transfer and Radiation Instrumentation
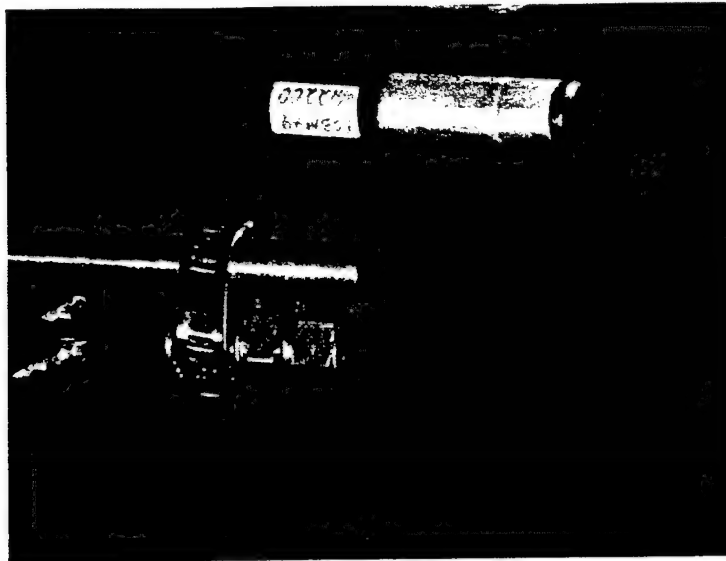
Figure 13 Water Vapor Measurement Sensor
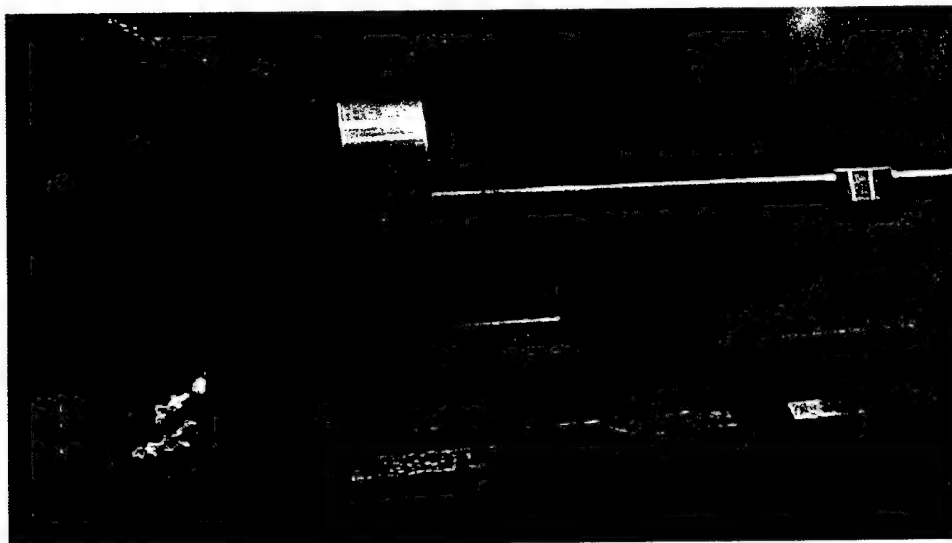
Figure 14 Photograph of Double Cone Model and Test Condition Rake Installed in 48" Tunnel
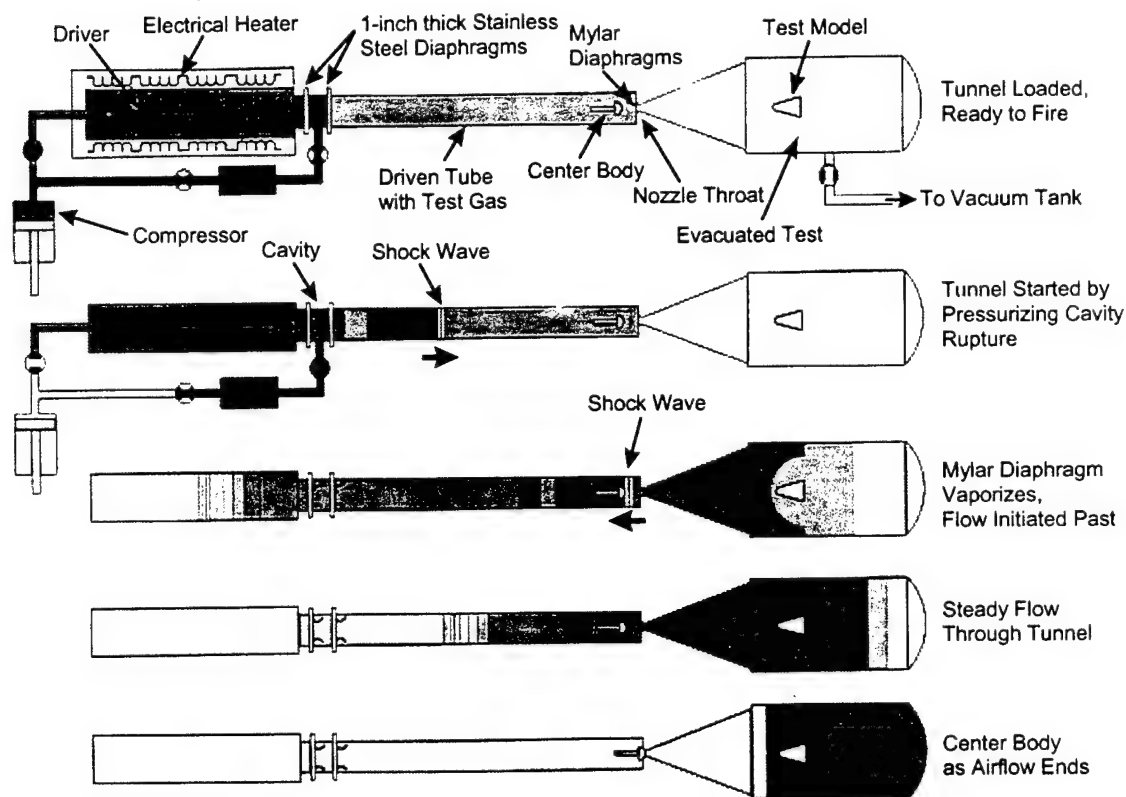
Figure 15   Schematic Diagram Illustrating the Operation of the 48" and LENS Shock Tunnels
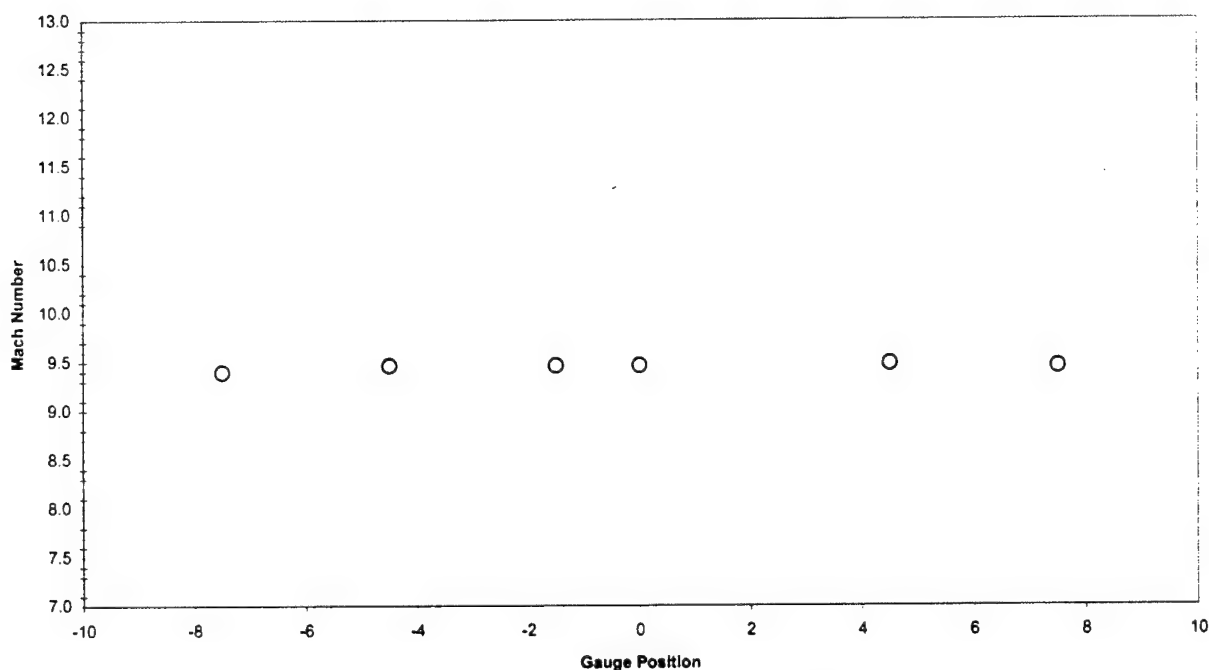
Figure 16   Mach Number Distribution Across Exit Plane of "D" Nozzle from Survey Rake Measurements
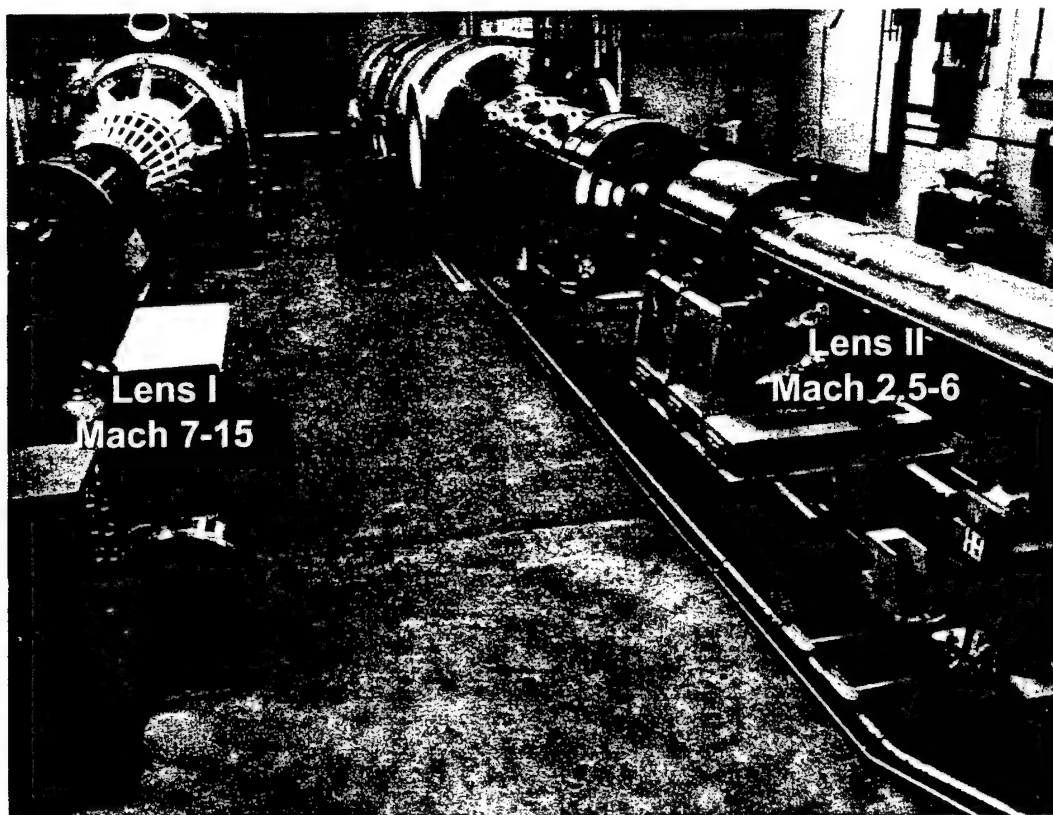
Figure 17 Photograph of LENS I and II Test Facilities
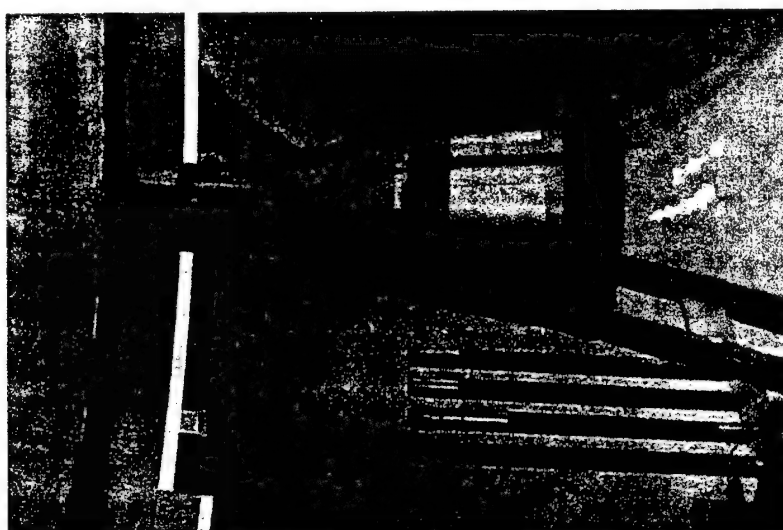
Figure 18 Hollow Cylinder Flare and Test Condition Rake Installed in LENS Shock Tunnel
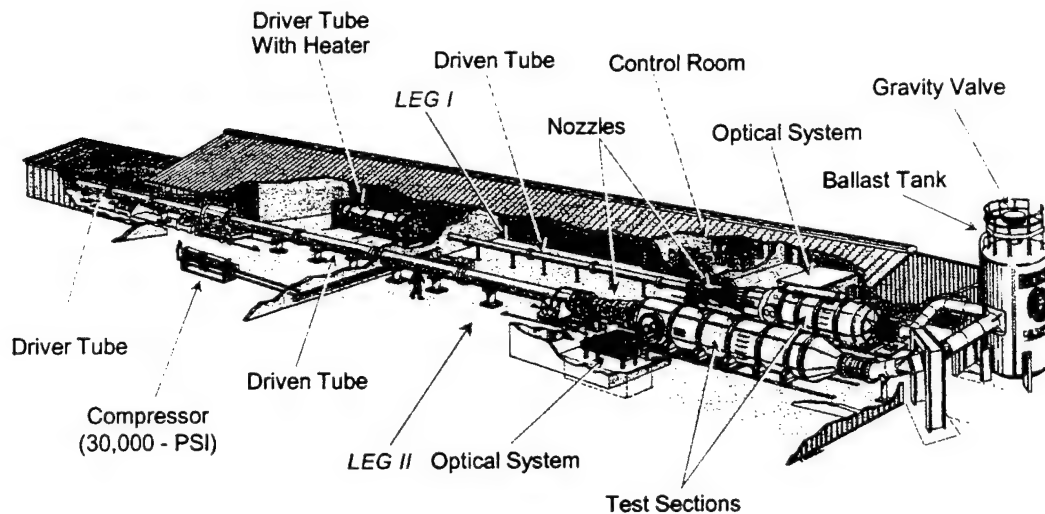
Figure 19 Schematic of Large Energy National Shock Tunnels (LENS)
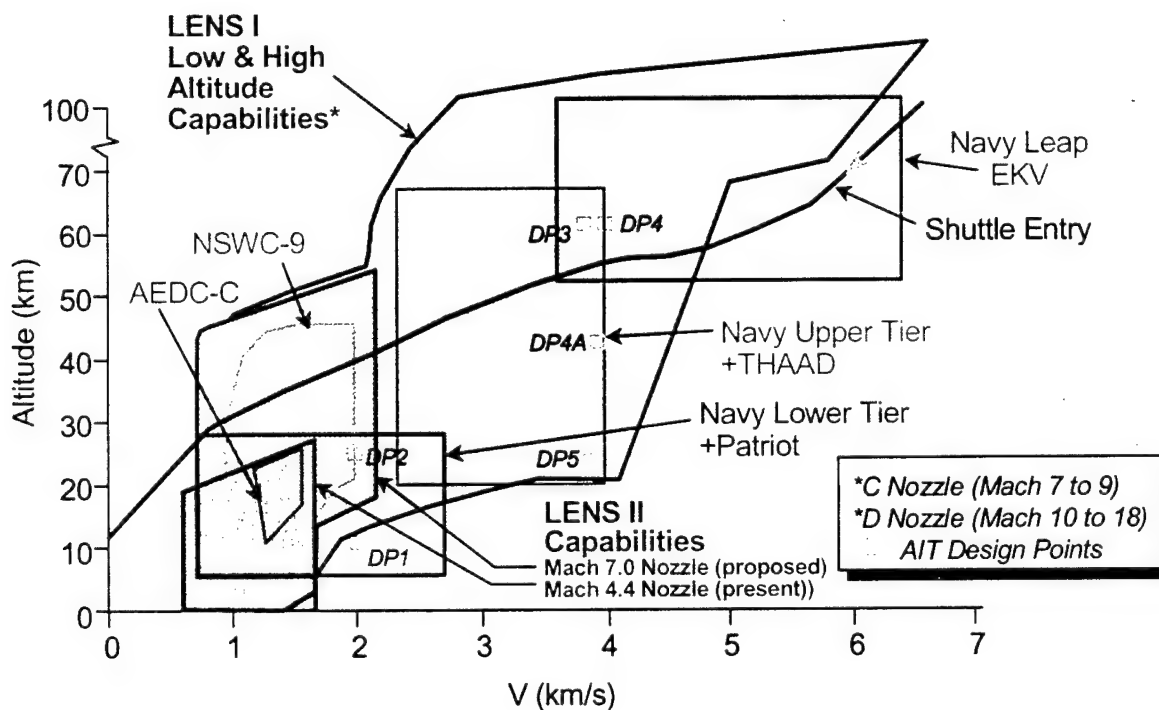
Figure 20 Velocity/Altitude Performance of the LENS I and II Test Facilities
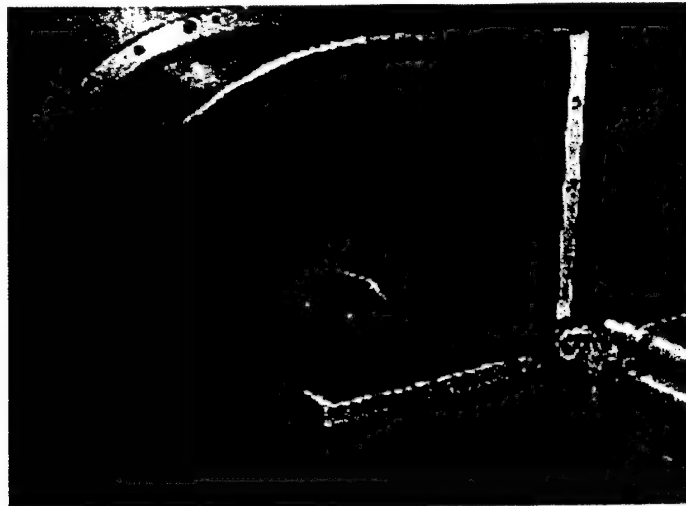
Figure 21 Rake Installed in LENS I Shock Tunnel
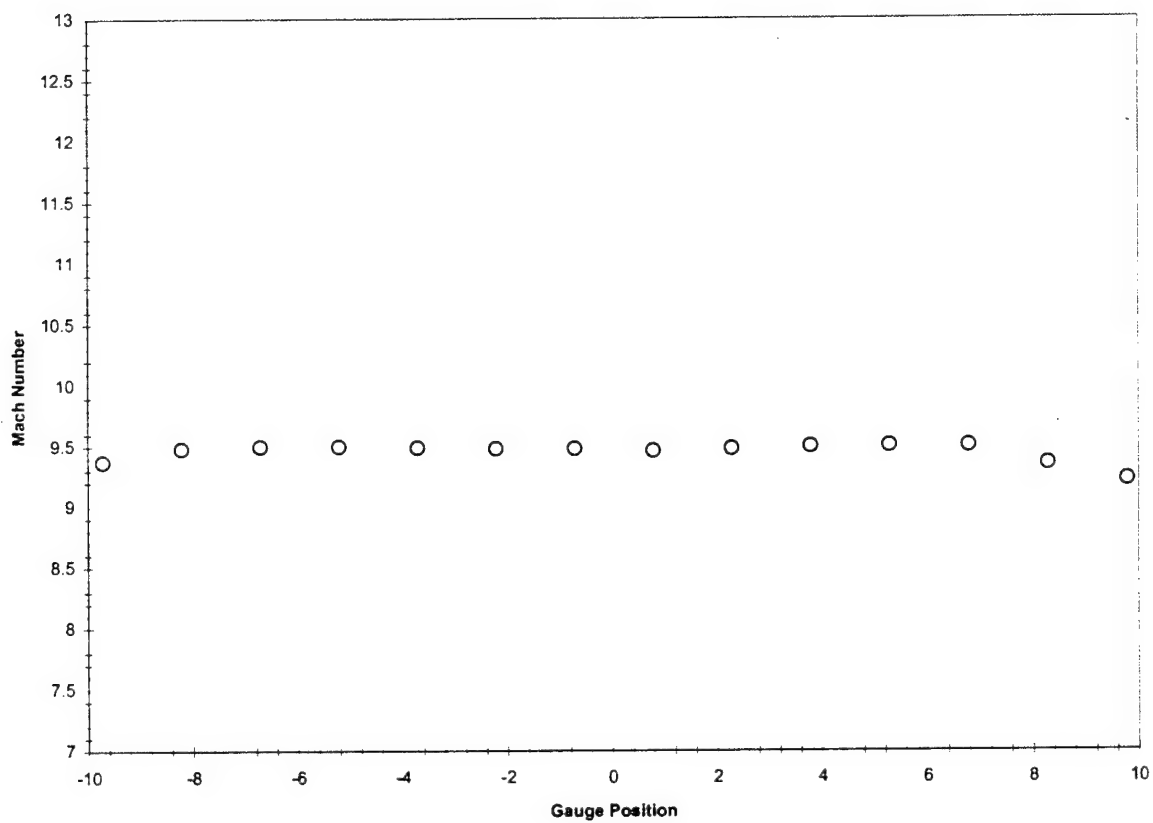
Figure 22 Mach Number Distribution across Test Core from LENS Leg I Indented Cone Tunnel Calibration Airflow – Calibration Measurements prior to the Double Cone Studies
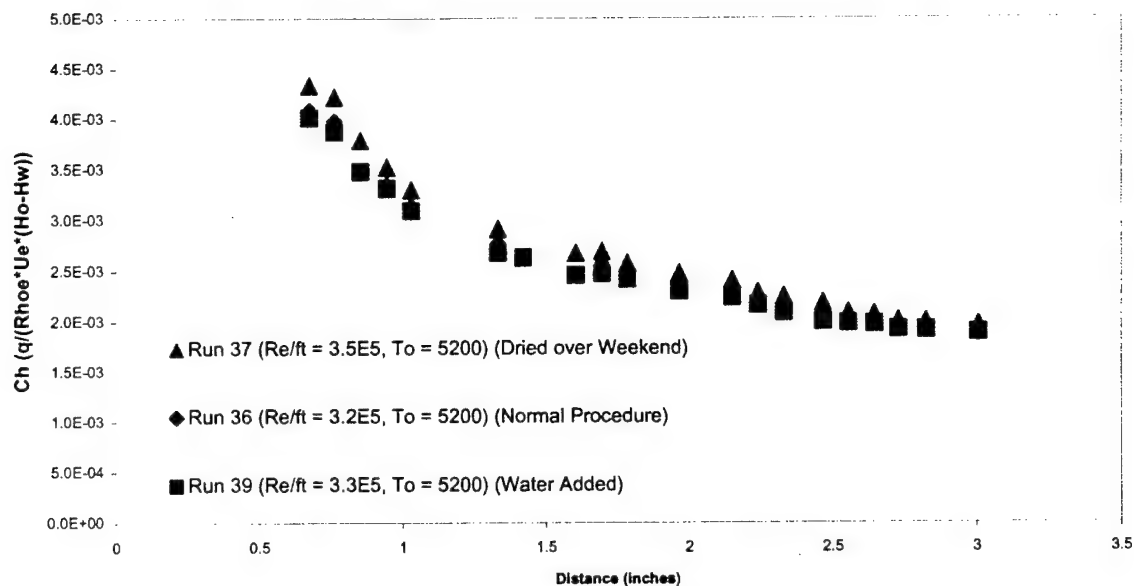
Figure 23   Results of Studies to Evaluate the Effects of Water Vapor in the Test Gas on the Heating Rates along the Cone
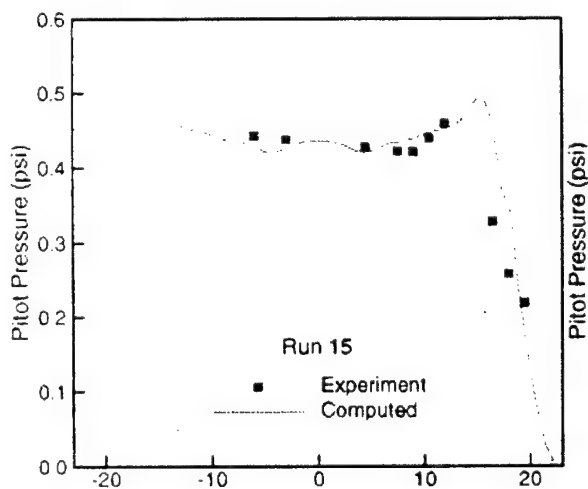
Figure 24 Comparisons between measured and predicted pitot distribution for Run 15 to validate model of viscous layer in nozzle code
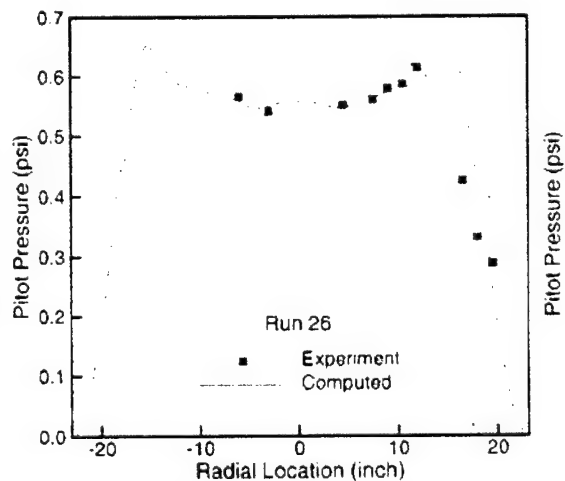
Figure 25 Comparisons between measured and predicted pitot pressure for Run 26 to validate model of viscous layer in nozzle code

42
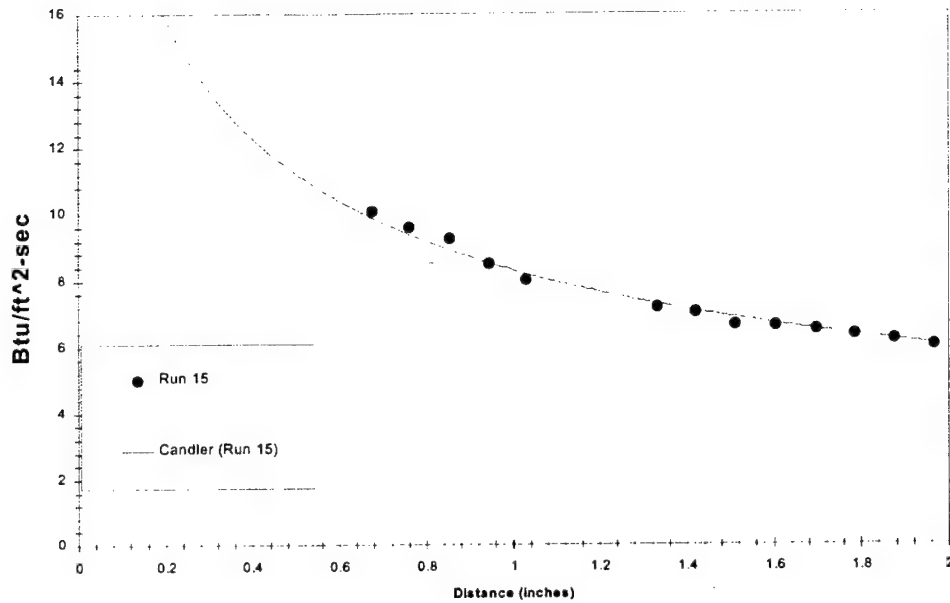
Figure 26 Comparison between Cone Heat Transfer Measurements and Candler's Navier-Stokes Prediction for Run 15
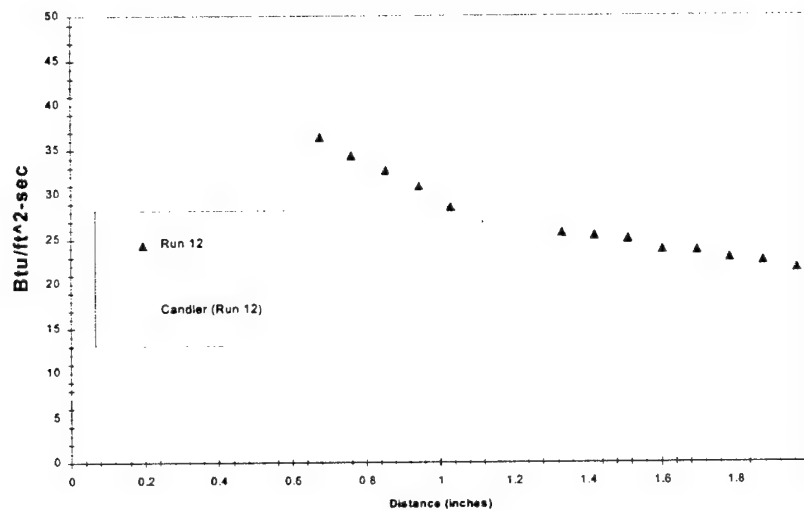
Figure 27 Comparison between Cone Heat Transfer Measurements and Candler's Navier-Stokes Prediction for Run 12

43
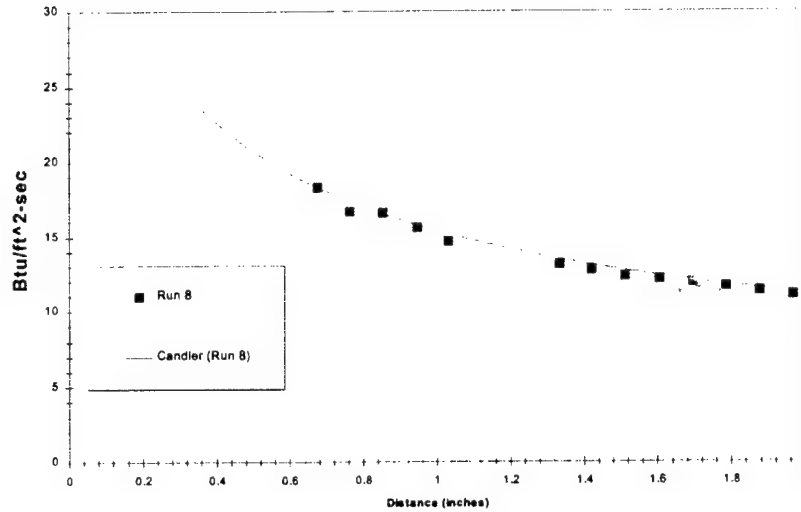
Figure 28 Comparison between Cone Heat Transfer Measurements and Candler's Navier-Stokes Prediction for Run 8
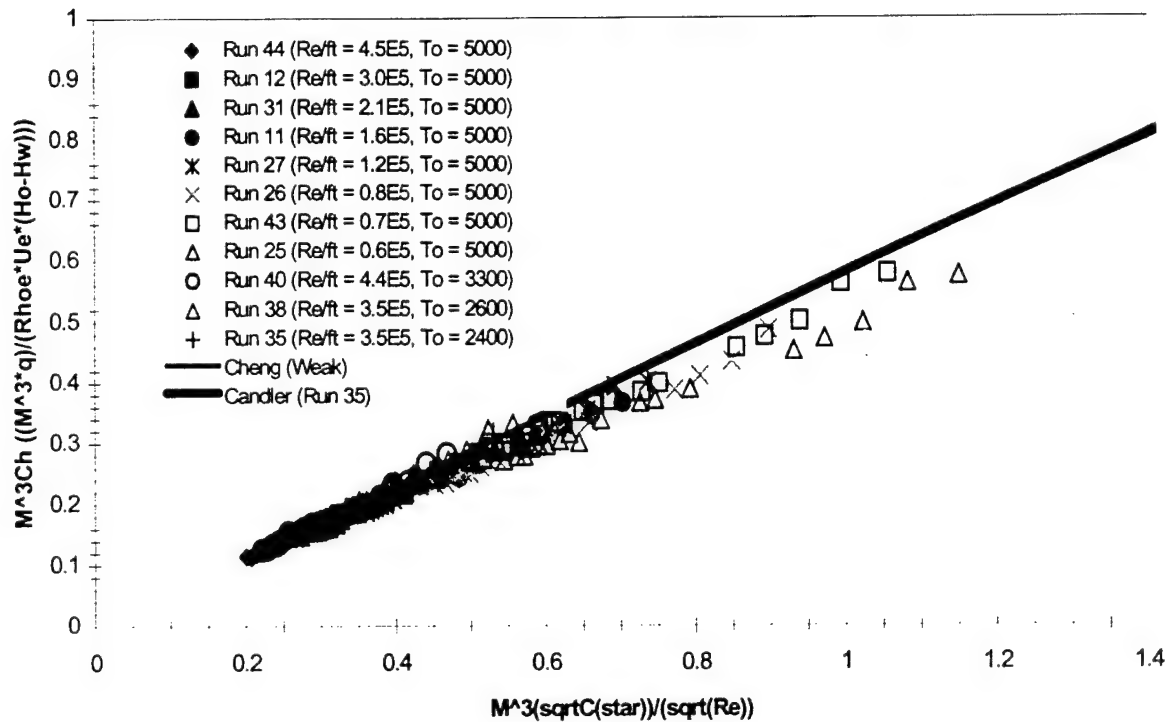
Figure 29 Correlation of All Cone Heating Measurements and Comparison with Simple Navier-Stokes Prediction Methods

Nondimensional Heat Transfer Cone Data (M^3Ch vs Chi(bar))
Reynolds Number Sweep (T₀ = 5000 Nominally)
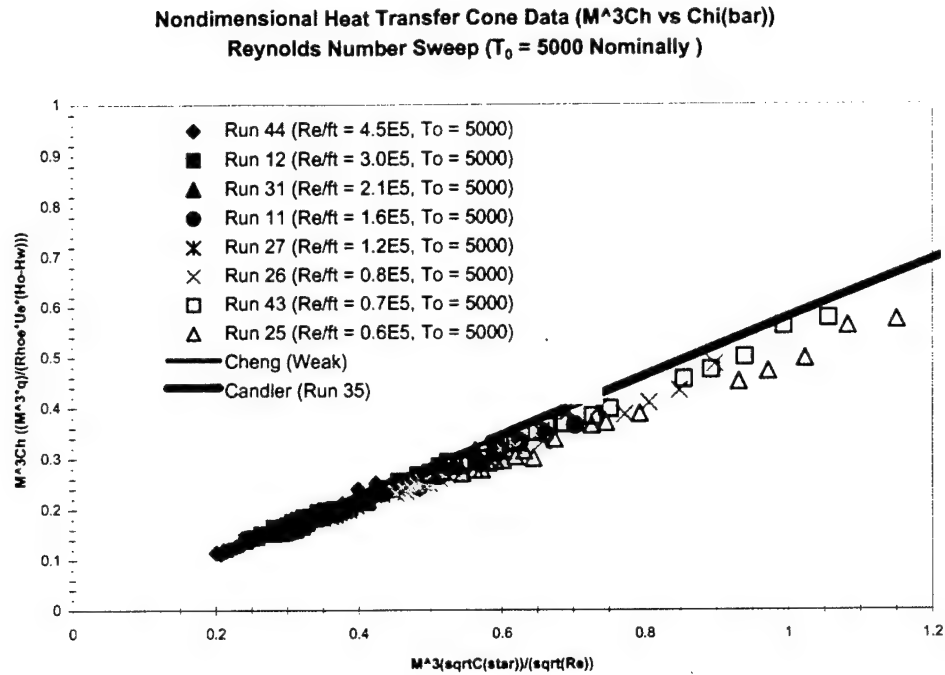
Figure 30   Correlation of Cone Heating Measurements and Comparison with Prediction Methods for High Stagnation Temperature Conditions Only

Nondimensional Heat Transfer Cone Data (M^3Ch vs Chi(bar))
T₀ Sweep (Re = 3.5E5 Nominally)
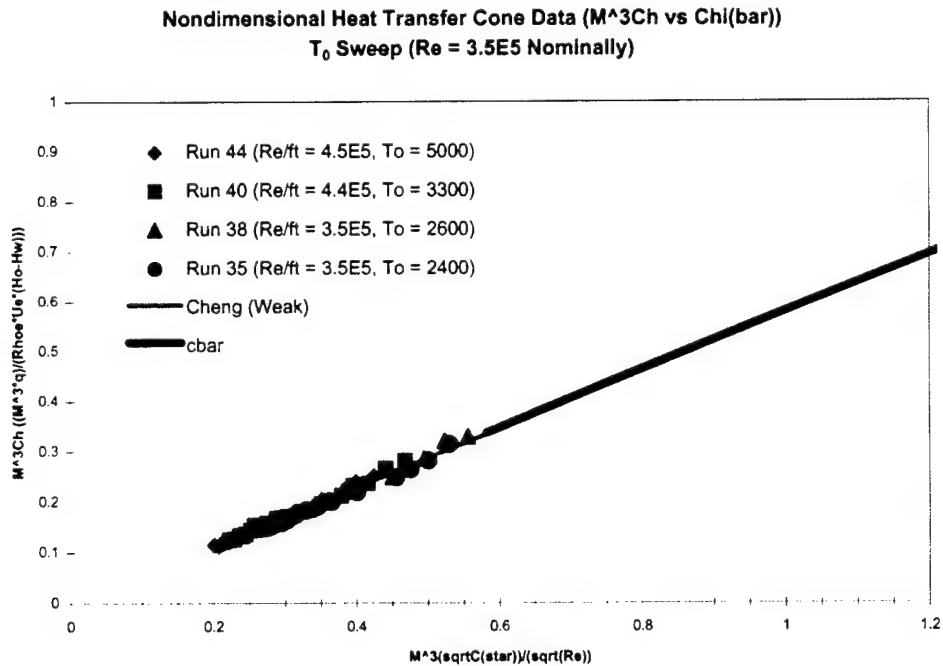
Figure 31 Correlation of Cone Heating Measurements and Comparison with Prediction Measurements for High Reynolds Number Conditions Only

45
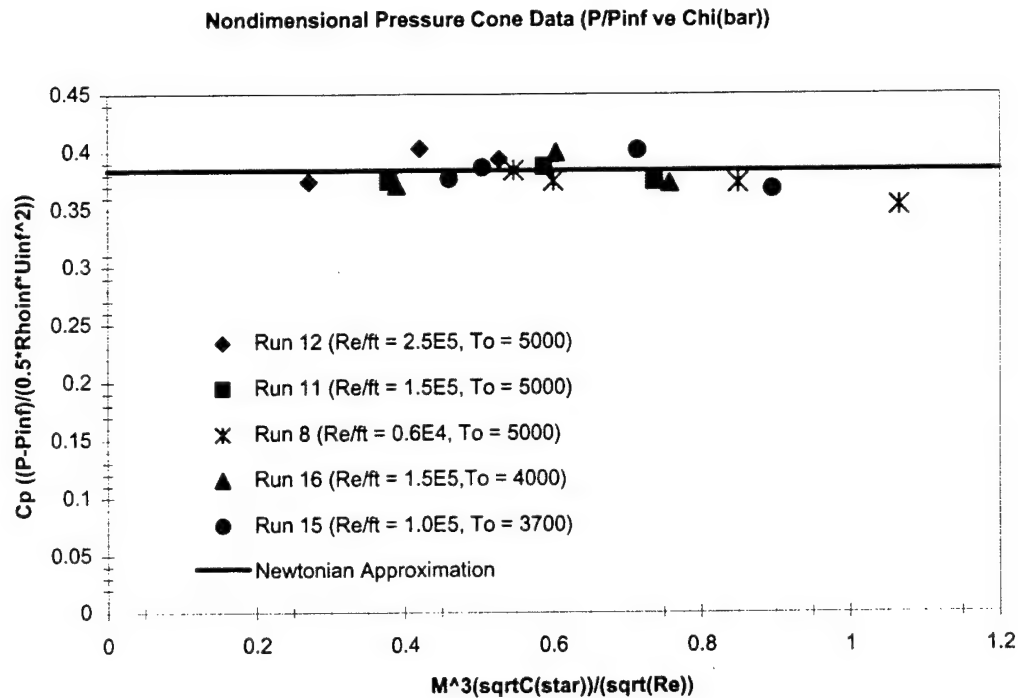
Figure 32 Comparison of Measurement of Cone Pressure and Predictions from Newtonian and Navier-Stokes Codes
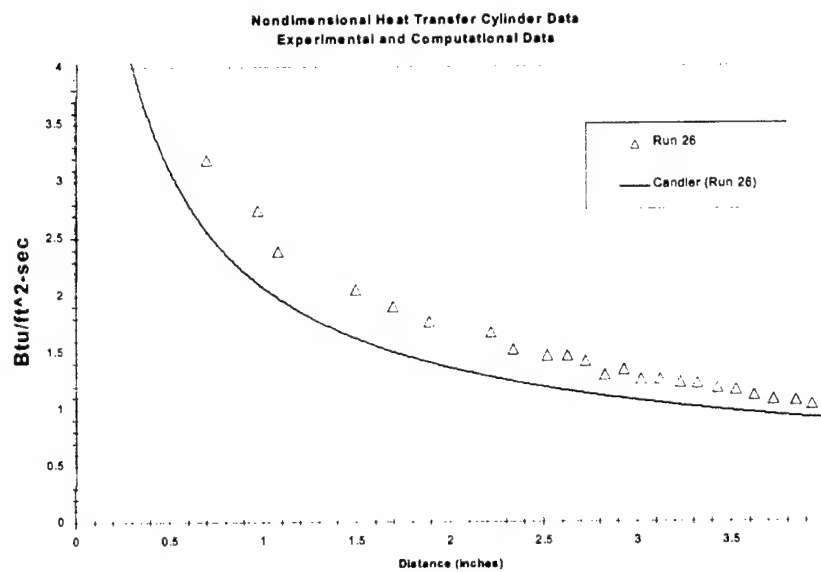
Figure 33 Comparison of Measurements of Heat Transfer on Cylinder and Candler's Predictions with Slip for Run 26

Nondimensional Heat Transfer Cylinder Data
Experimental and Computational Data
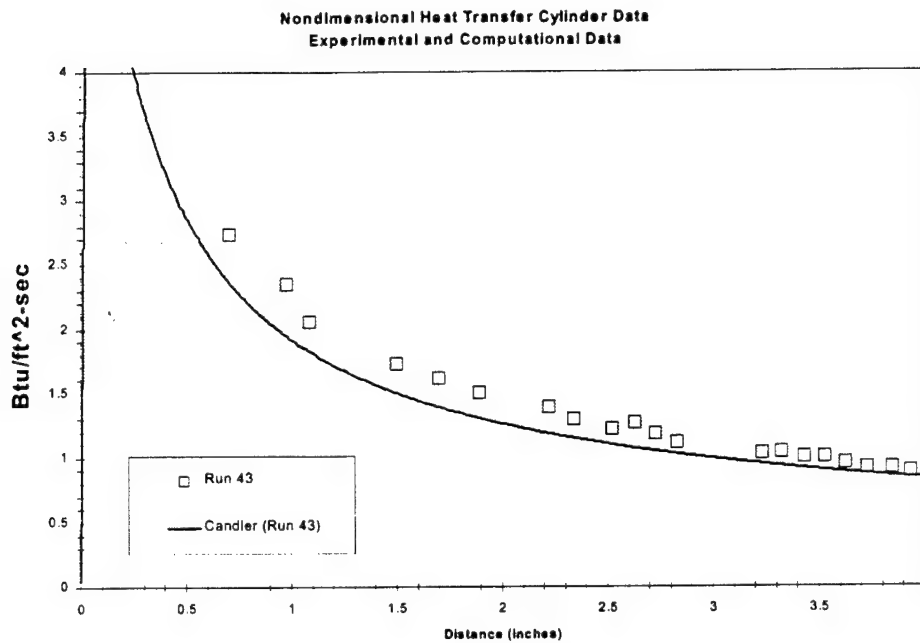
Figure 34 Comparison of Measurements of Heat Transfer on Cylinder and Candler's Predictions with Slip for Run 43

Nondimensional Heat Transfer Cylinder Data (M^3Ch vs Chi(bar))
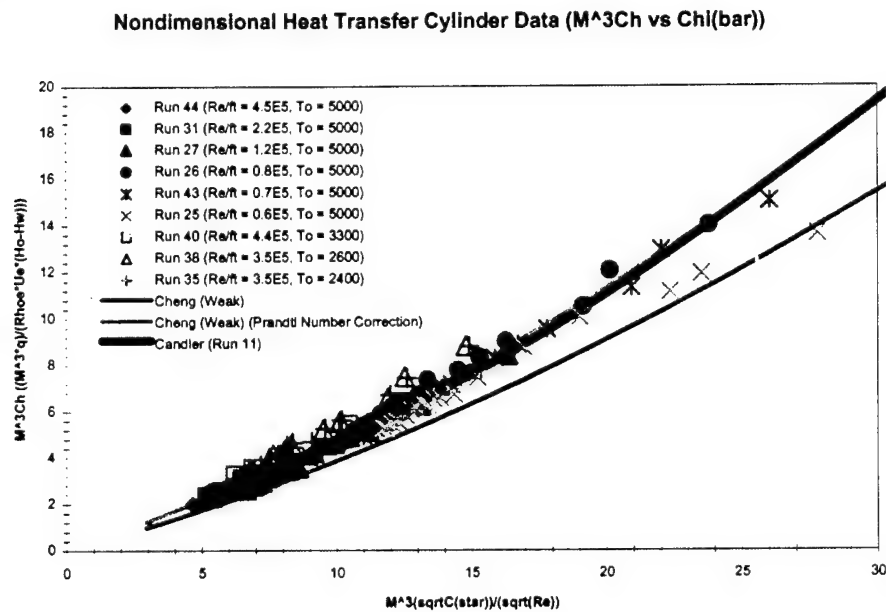
Figure 35 Correlation of All Cylinder Measurements and Comparison with Simple and Navier-Stokes Prediction Methods

47
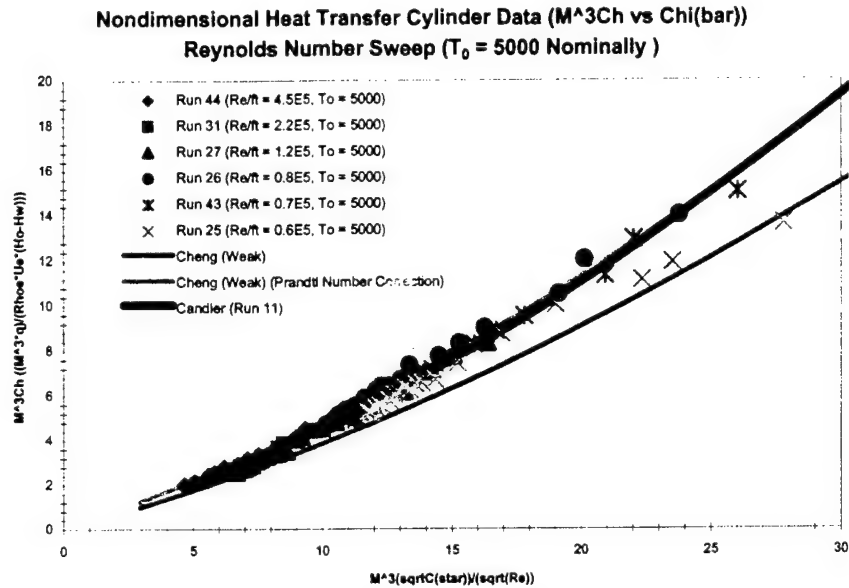
Figure 36 Correlation of Cylinder Heating and Comparison with Simple and Navier-Stokes Predictions
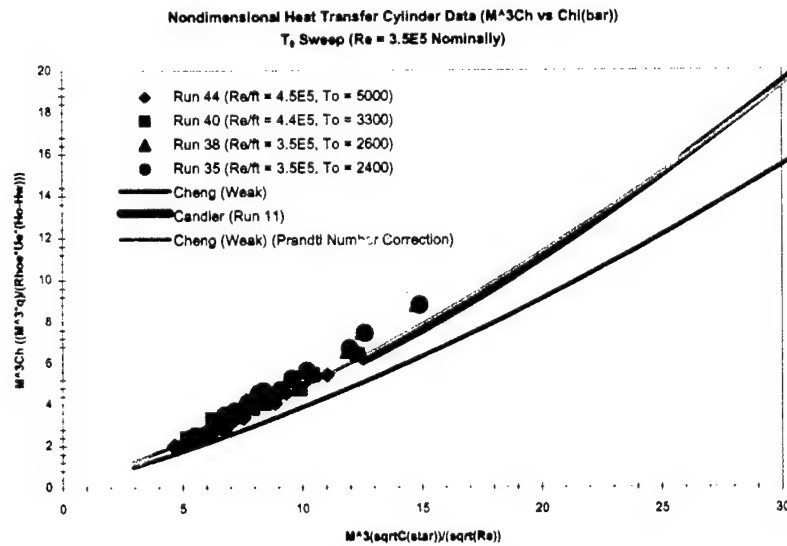
Figure 37 Correlation of Cylinder Heating and Comparison with Predictions for Only High-Temperature Flows

Nondimensional Pressure Cylinder Data (P/Pinf ve Chi(bar))
Reynolds Number Sweep (T_0 = 5200 Nominally)

Legend:
- Cheng (Weak)
- Run 44 (Re/ft = 3.5E5, To = 5000)
- Run 31 (Re/ft = 1.6E5, To = 5000)
- Run 27 (Re/ft = 1.0E5, To = 5000)
- Candler (Run 11)

Y-axis: P/Pinf
X-axis: M^3(sqrtC(star))/(sqrt(Re))
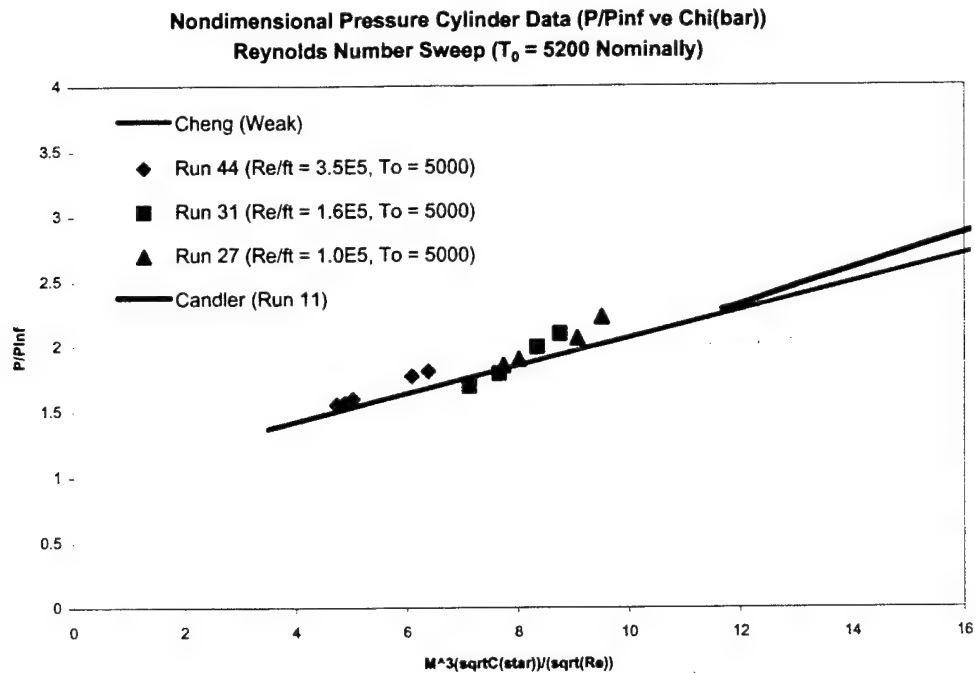
Figure 38 Correlation of Cylinder Heating Measurements and Comparison with Prediction Methods for High Reynolds Number Data Only

Legend:
- ■ Pressure
- Candler Cp
- ○ Heat Transfer
- Candler St
- Candler St (Noneq. CFD Slip)

Y-axis left: Cp
Y-axis right: St
X-axis: X/L
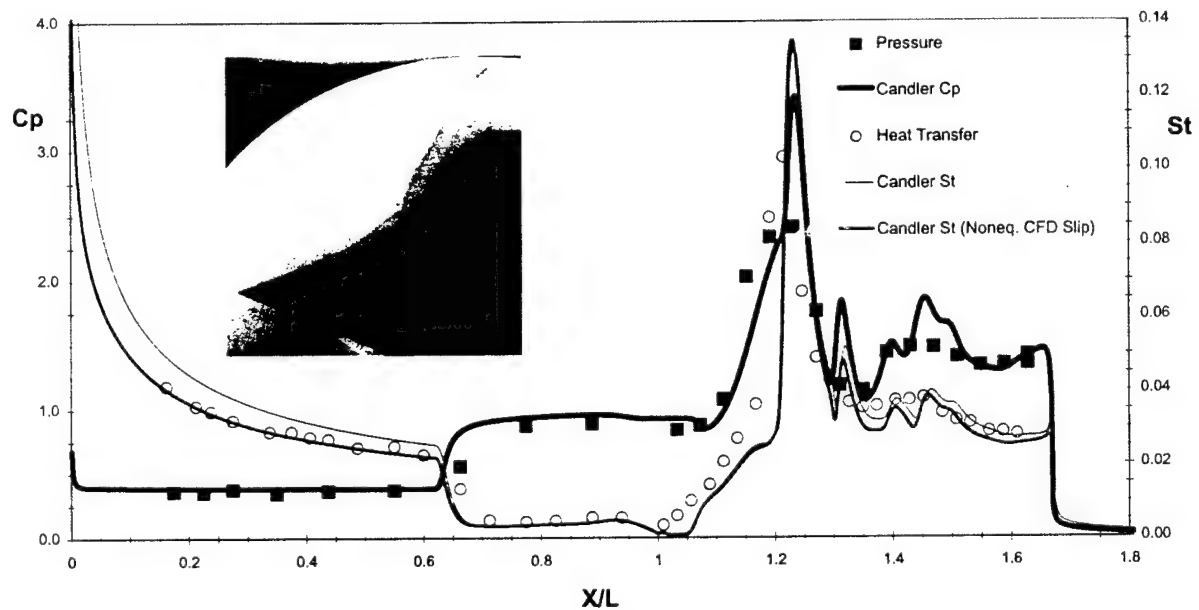
Figure 39   Candler's Predictions of Pressure, Heat Transfer and Schlieren Photograph For Run 35 (M = 12.5, Re#/ft = 6.74E+04)
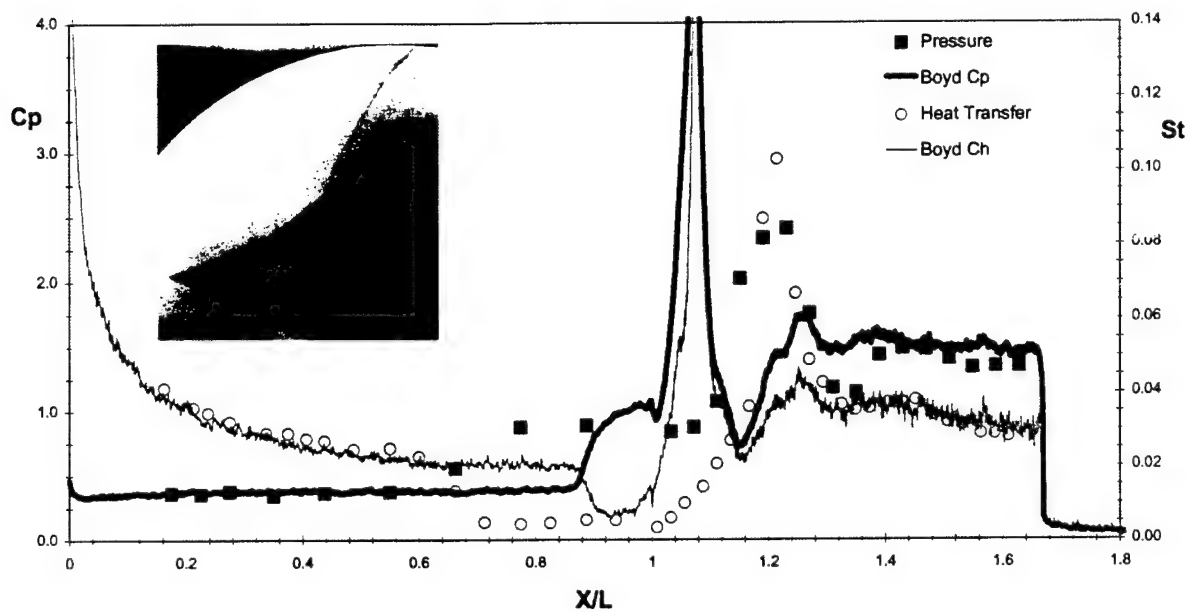
**Figure 40 Pressure, Heat Transfer and Schlieren Photo
Run 35 (M = 12.5, Re#/ft = 6.74E+04) : Boyd**
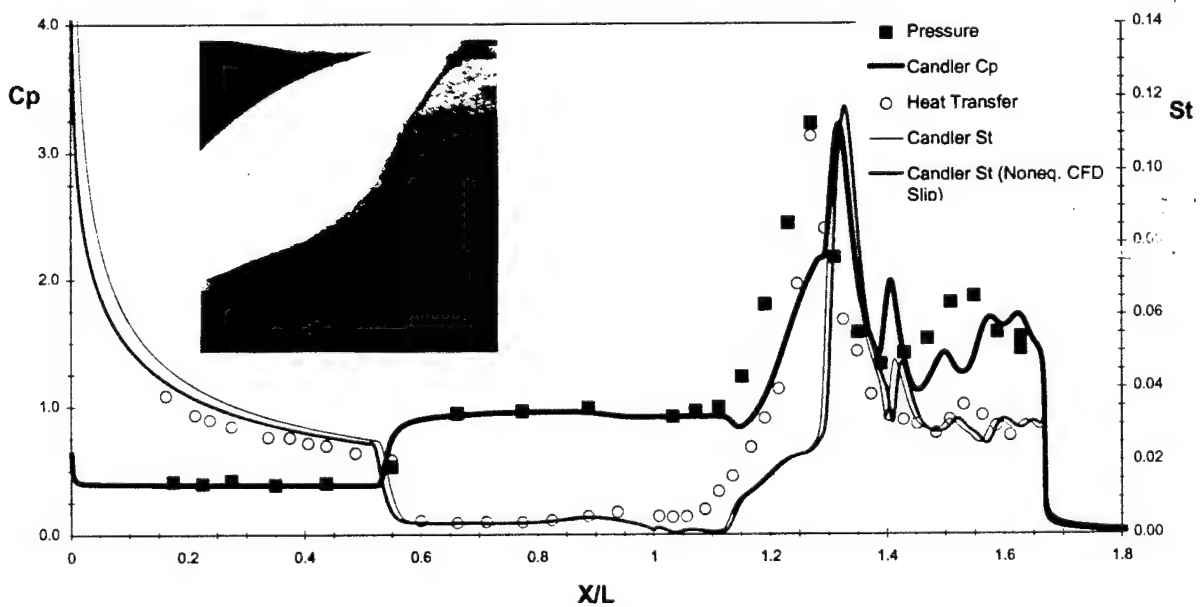
**Figure 41 Pressure, Heat Transfer and Schlieren Photo
Run 28 (M = 10.49, Re#/ft = 5.83E+04) : Candler**

50
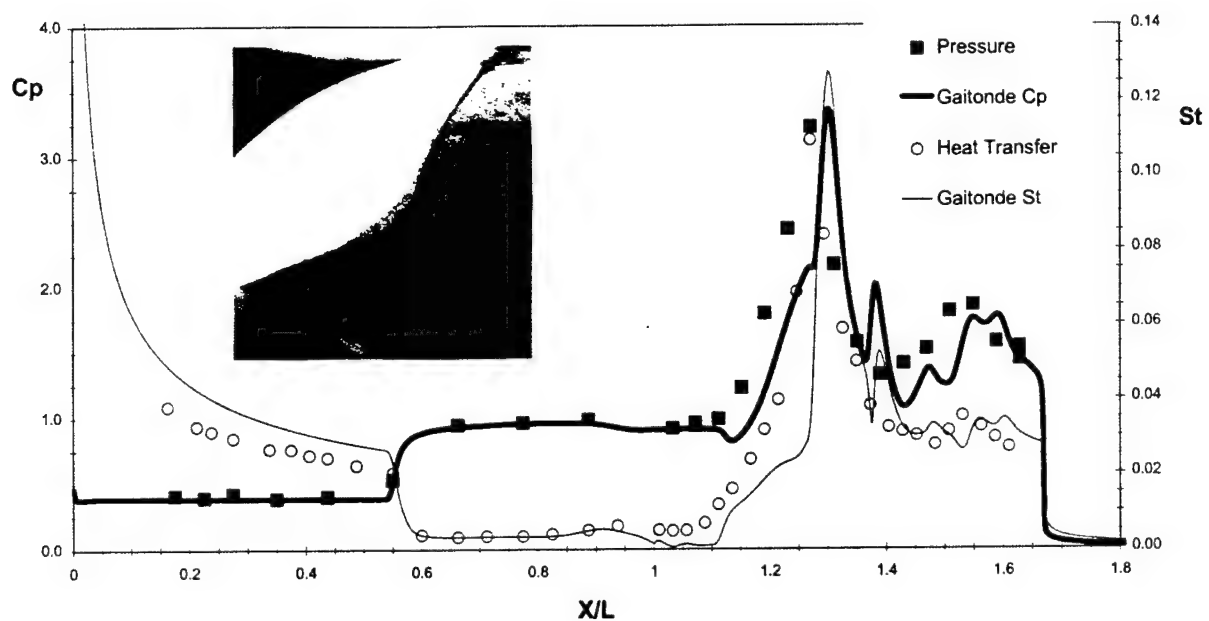
Figure 42   Pressure, Heat Transfer and Schlieren Photo
Run 28 (M = 10.49, Re#/ft = 5.83E+04) : Gaitonde
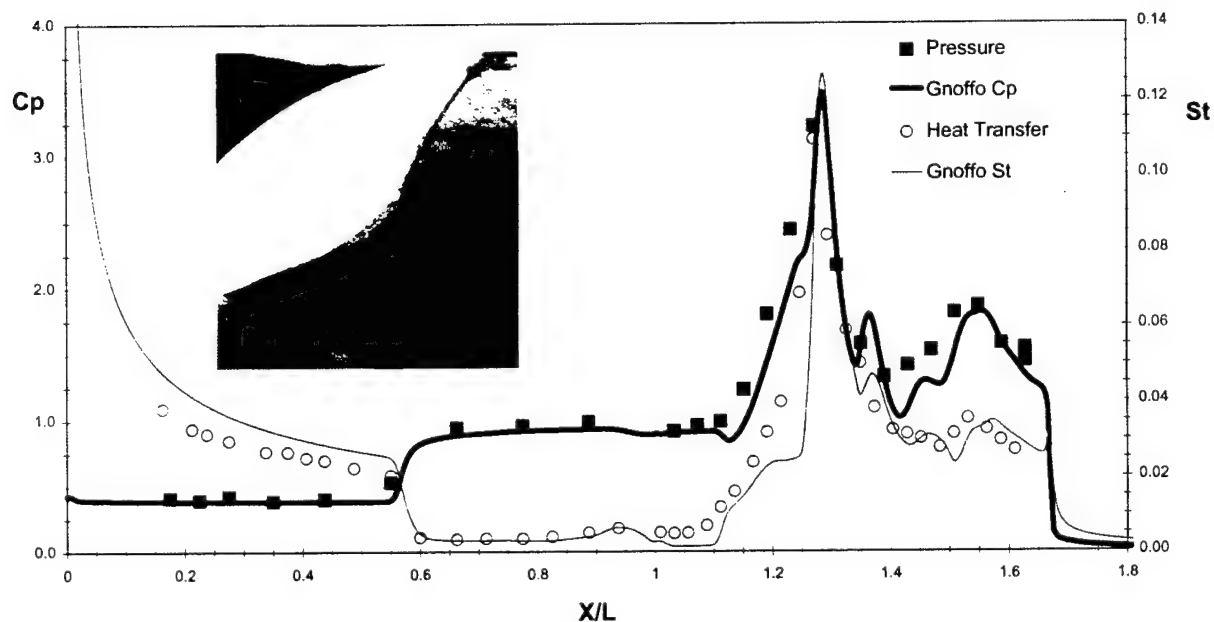
Figure 43   Pressure, Heat Transfer and Schlieren Photo
Run 28 (M = 10.49, Re#/ft = 5.83E+04) : Gnoffo
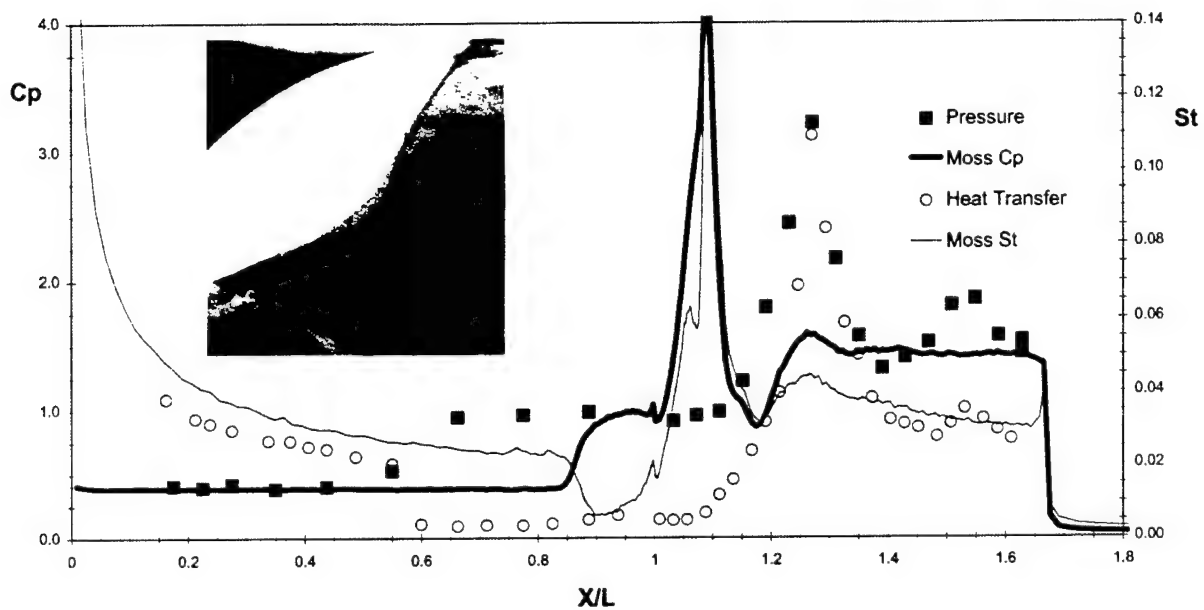
**Figure 44   Pressure, Heat Transfer and Schlieren Photo
Run 28 (M = 10.49, Re#/ft = 5.83E+04) : Moss**
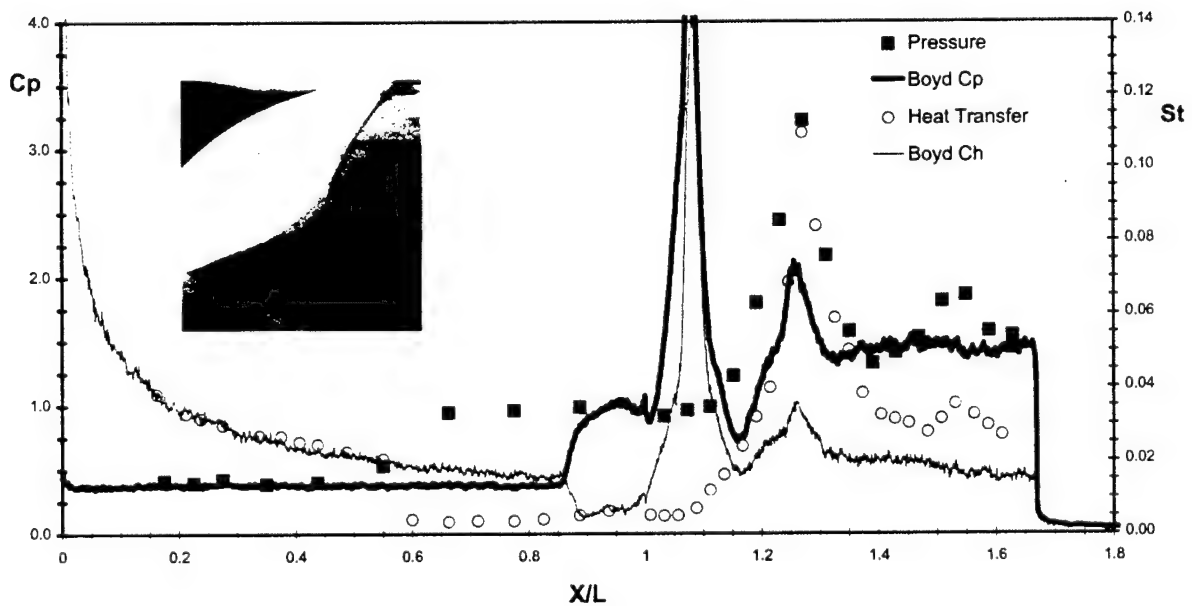
**Figure 45   Pressure, Heat Transfer and Schlieren Photo
Run 28 (M = 10.49, Re#/ft = 5.83E+04) : Boyd**
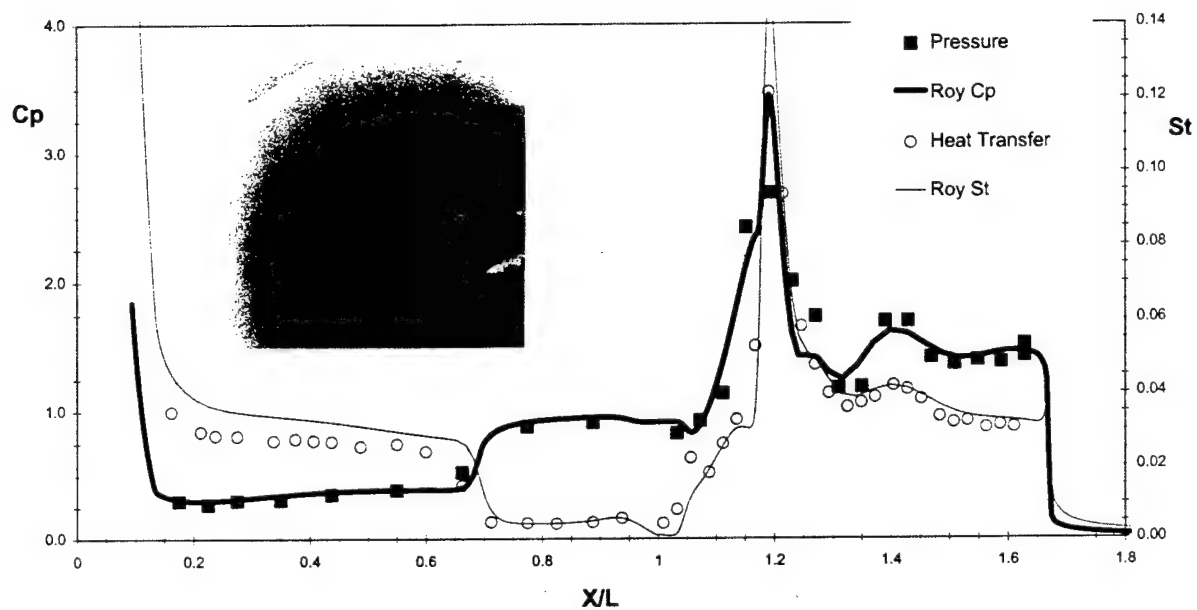
Figure 46   Pressure, Heat Transfer and Schlieren Photo
Run 31 (M = 12.4, Re#/ft = 6.08E+04) : Roy
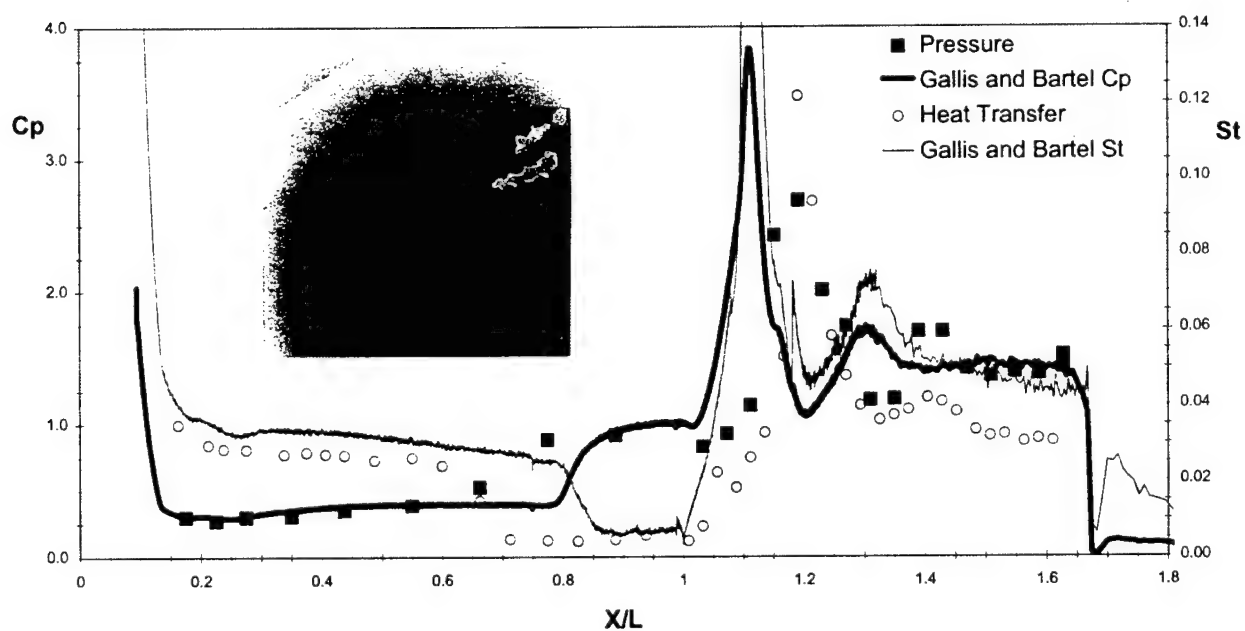
Figure 47   Pressure, Heat Transfer and Schlieren Photo
Run 31 (M = 12.4, Re#/ft = 6.08E+04) : Gallis and Bartel
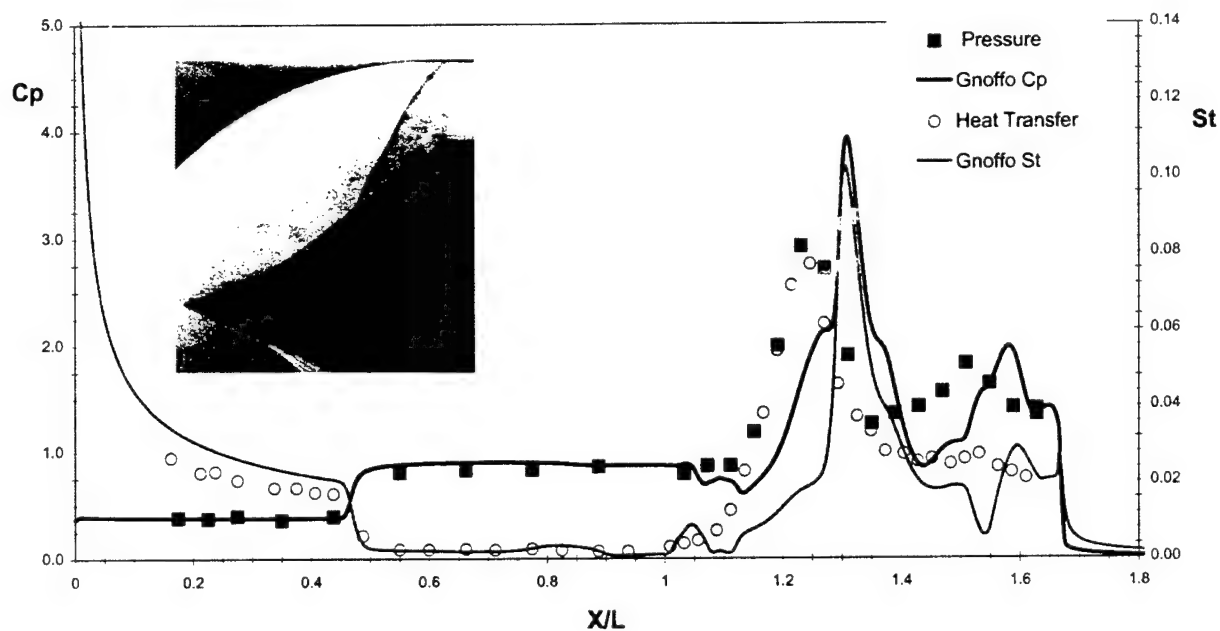
**Figure 48   Pressure, Heat Transfer and Schlieren Photo
Run 24 (M = 10.4, Re#/ft = 10.4E+04 : Gnoffo**
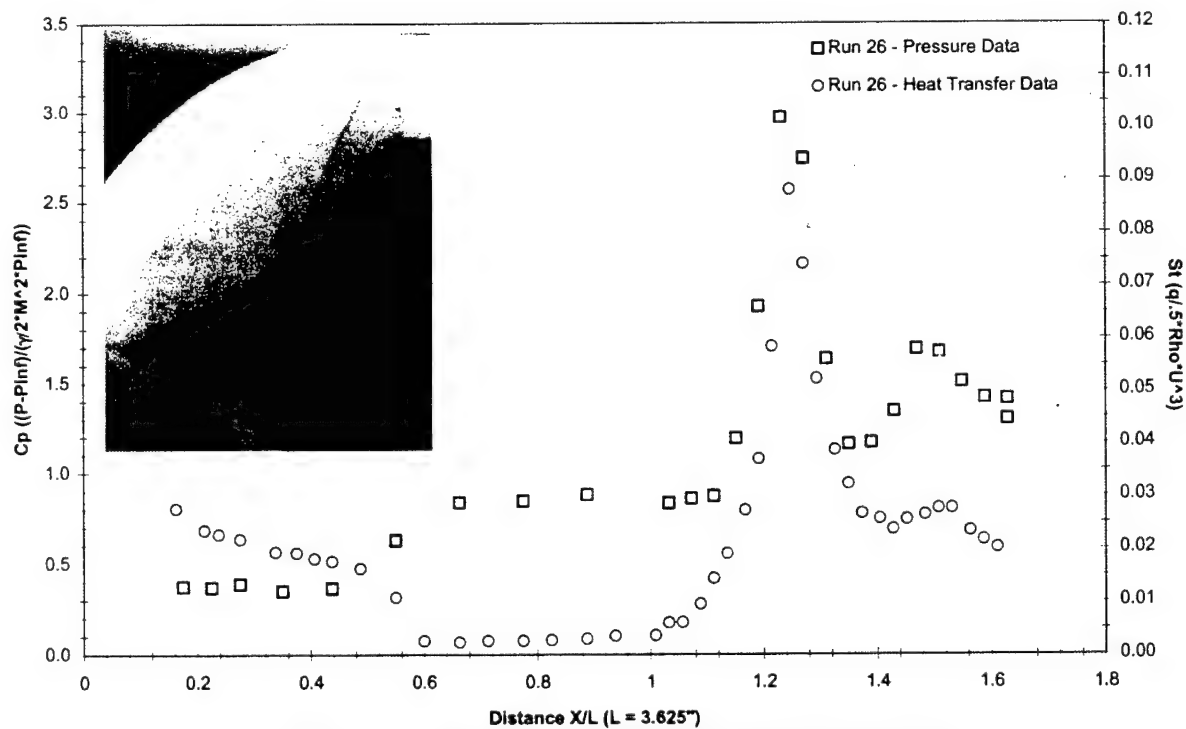
**Figure 49 Pressure, Heat Transfer and Schlieren Photograph
For Run 26 (M = 10.3, Re#/ft = 8E+04)**
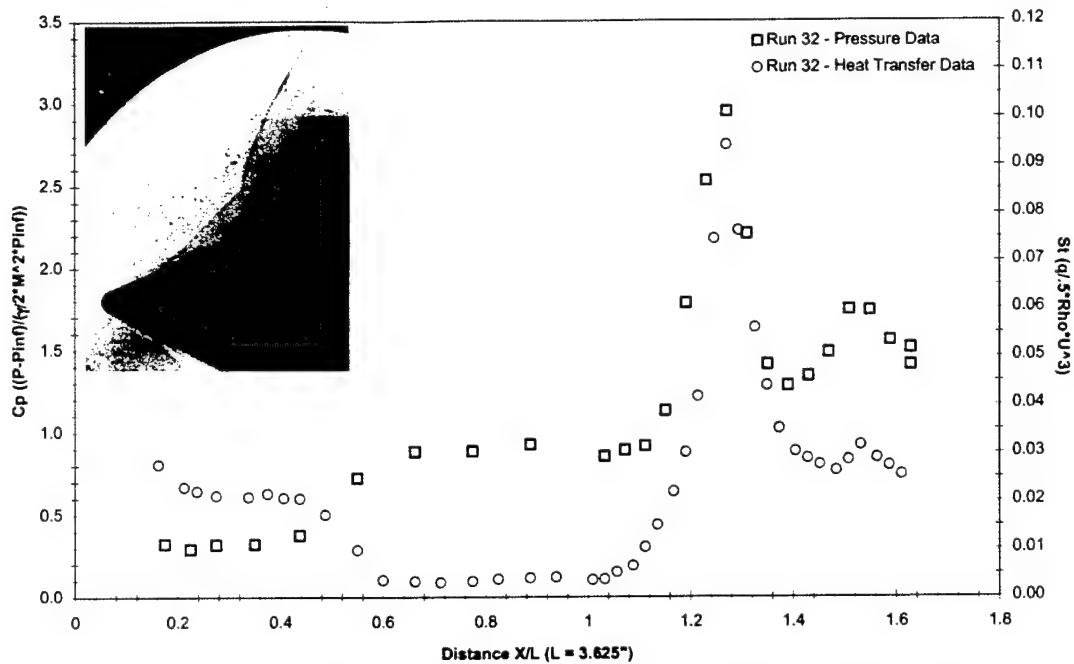
**Figure 50 Pressure, Heat Transfer, and Schlieren Photograph
For Run 32 (M = 10.4, Re#/ft = 6E+04)**
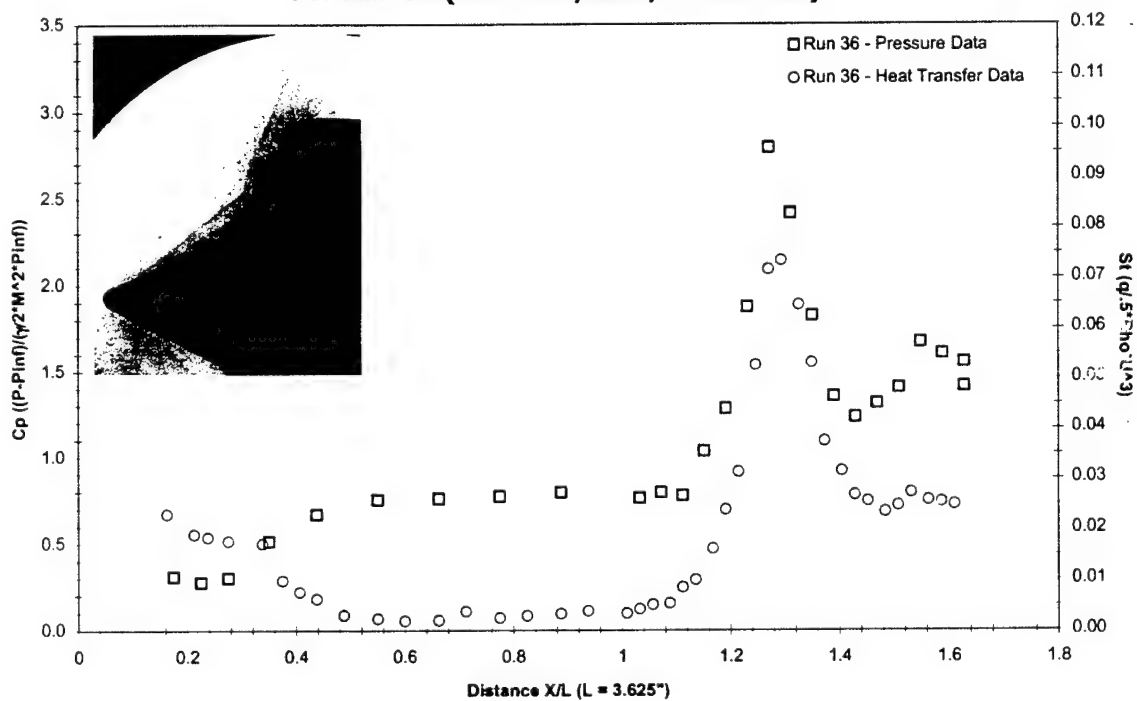
**Figure 51 Pressure, Heat Transfer, and Schlieren Photograph
For Run 36 (M = 10.3, Re#/ft = 8E+04)**
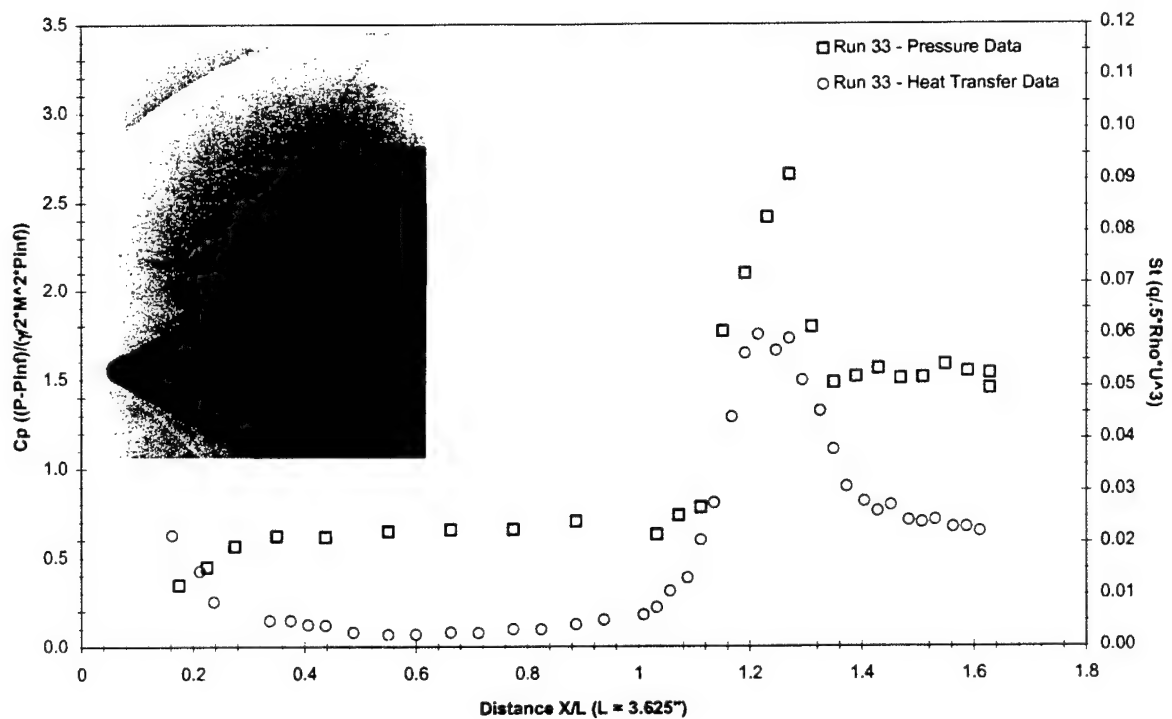
**Figure 52 Pressure, Heat Transfer, and Schlieren Photograph
For Run 33 (M = 10.3, Re#/ft = 9E+04)**
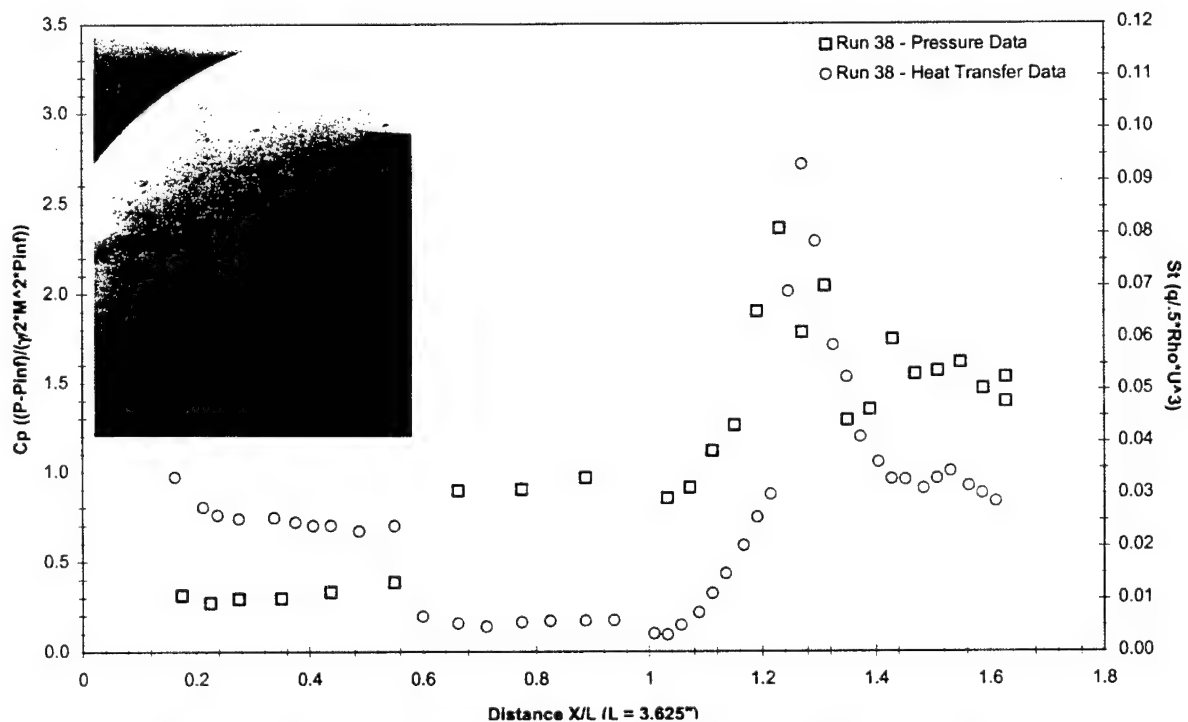
**Figure 53 Pressure, Heat Transfer, and Schlieren Photograph
For Run 38 (M = 12.4, Re#/ft = 6E+04)**
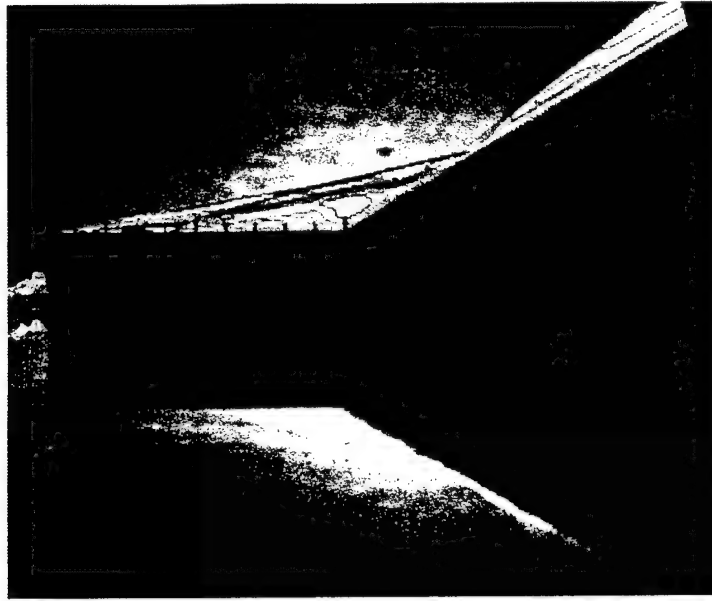
Figure 54   Run 8 Schlieren Photo with Density Contours of Gnoffo
(M = 12.3, Re#/ft = 12E+04)
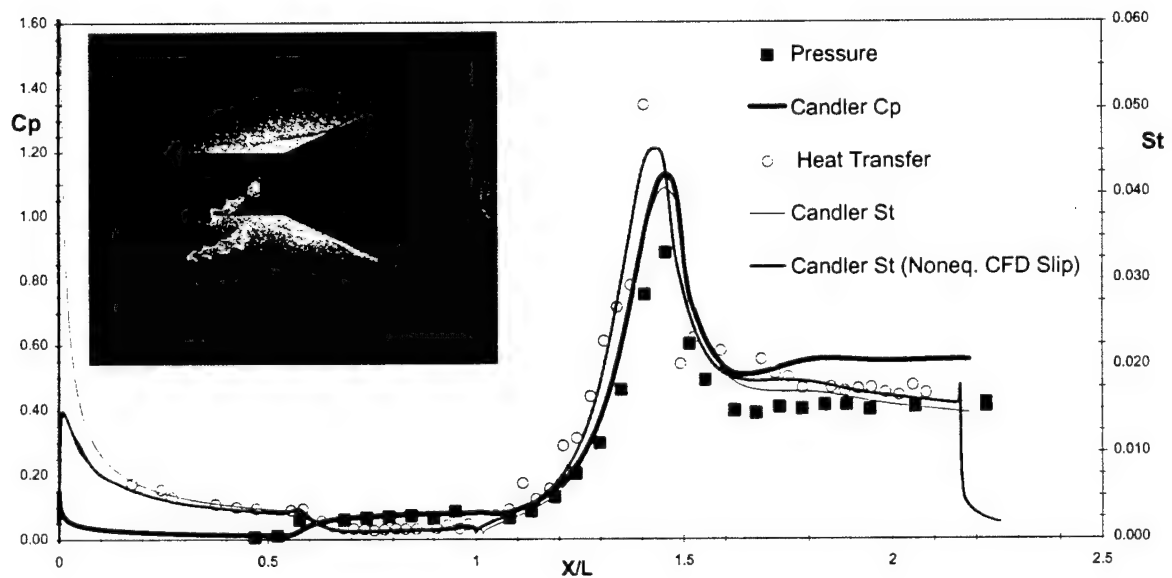
Figure 55   Pressure, Heat Transfer and Schlieren Photo Run 14
(M = 10.3, Re#/ft = 7.83E+04) : Candler
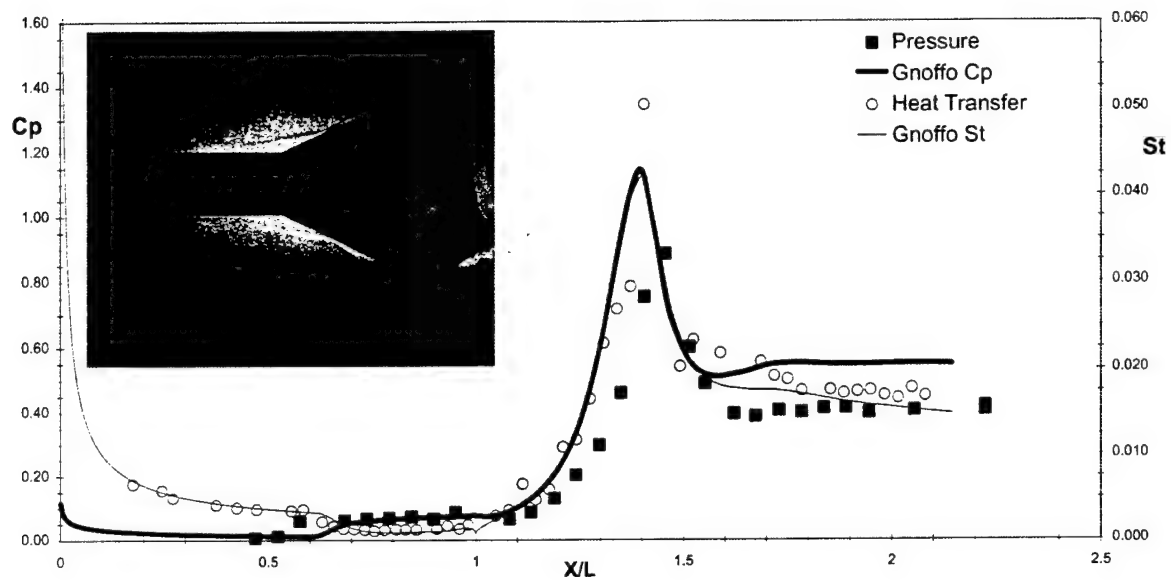
Figure 56   Pressure, Heat Transfer and Schlieren Photo Run 14
(M = 10.3, Re#/ft = 7.83E+04) : Gnoffo
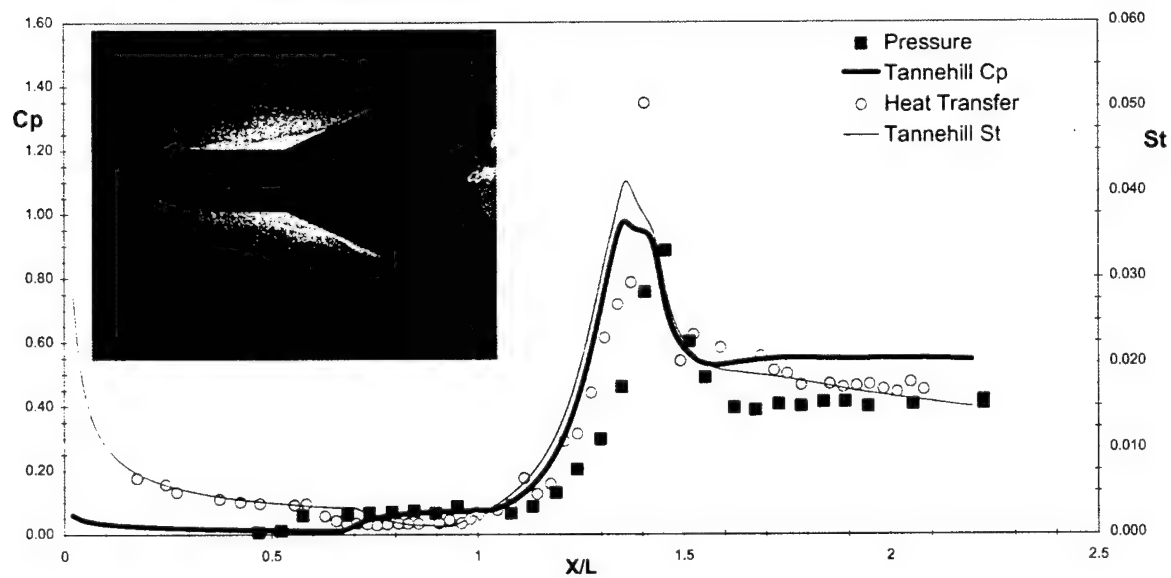
Figure 57   Pressure, Heat Transfer and Schlieren Photo Run 14
(M = 10.3, Re#/ft = 7.83E+04) : Tannehill

58
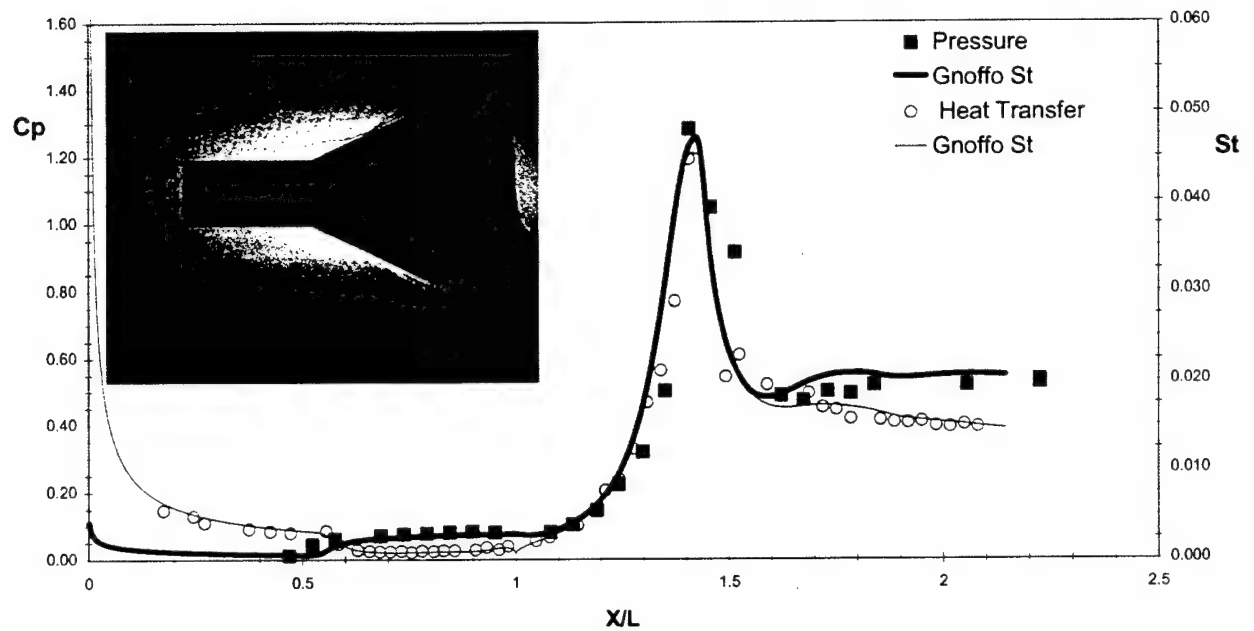
Figure 58   Pressure, Heat Transfer and Schlieren Photo
Run 9 (M = 12.48, Re#/ft = 10.9E+04) : Gnoffo
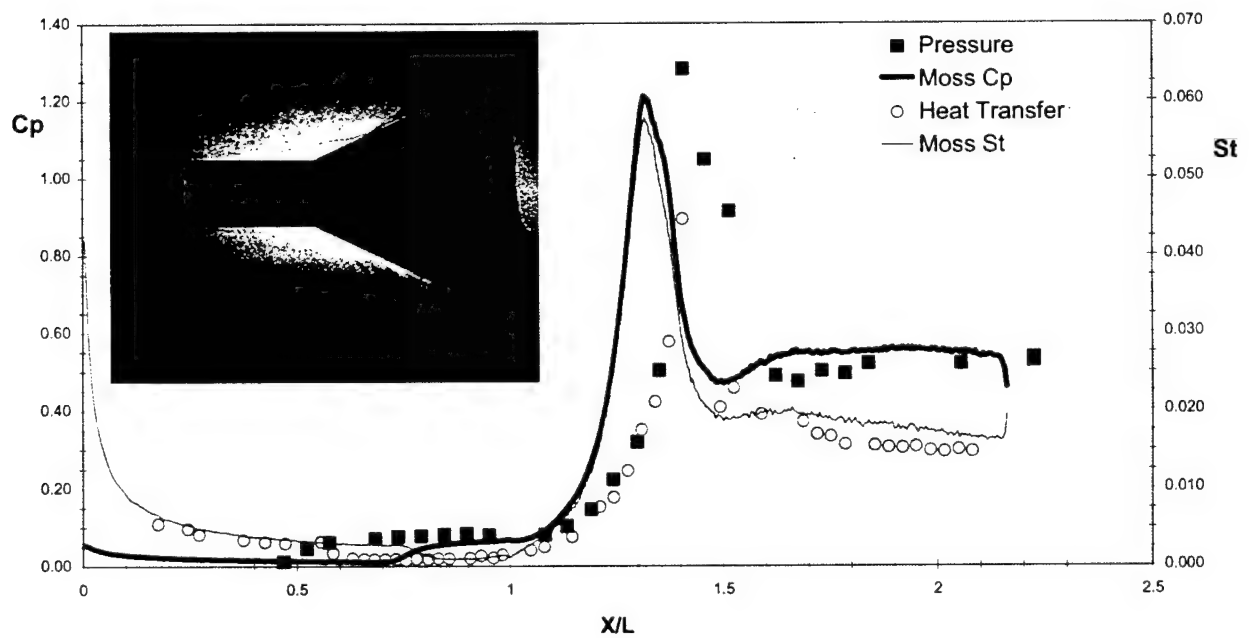
Figure 59   Pressure, Heat Transfer and Schlieren Photo
Run 9 (M = 12.48, Re#/ft = 10.9E+04) : Moss
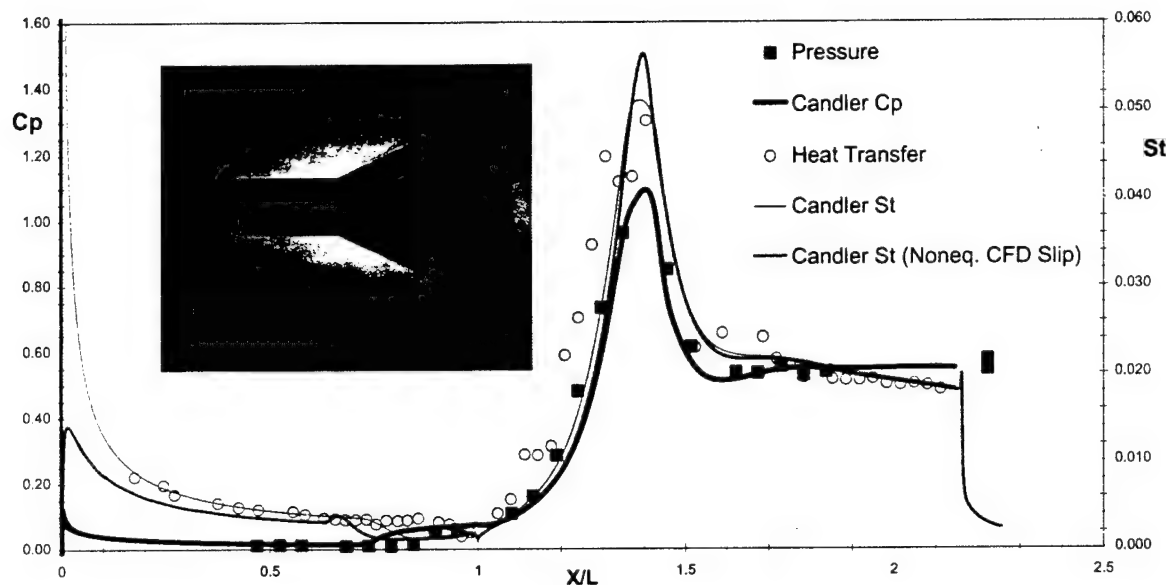
**Figure 60   Pressure, Heat Transfer and Schlieren Photo
Run 11 (M = 12.23, Re#/ft = 6.25E+04) : Candler**
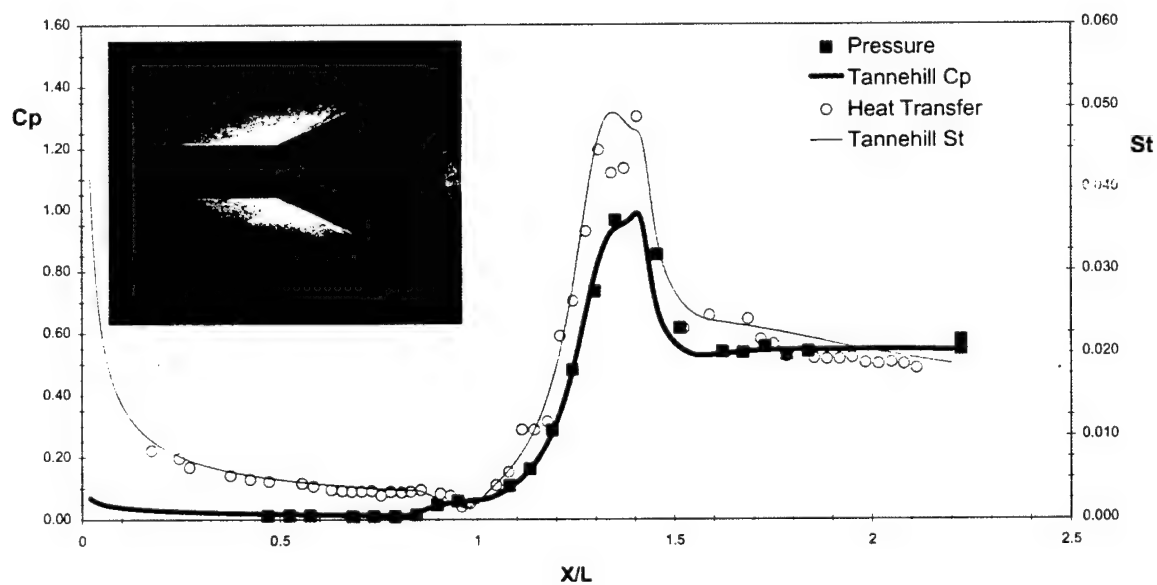
**Figure 61   Pressure, Heat Transfer and Schlieren Photo
Run 11 (M = 12.23, Re#/ft = 6.25E+04) : Tannehill**
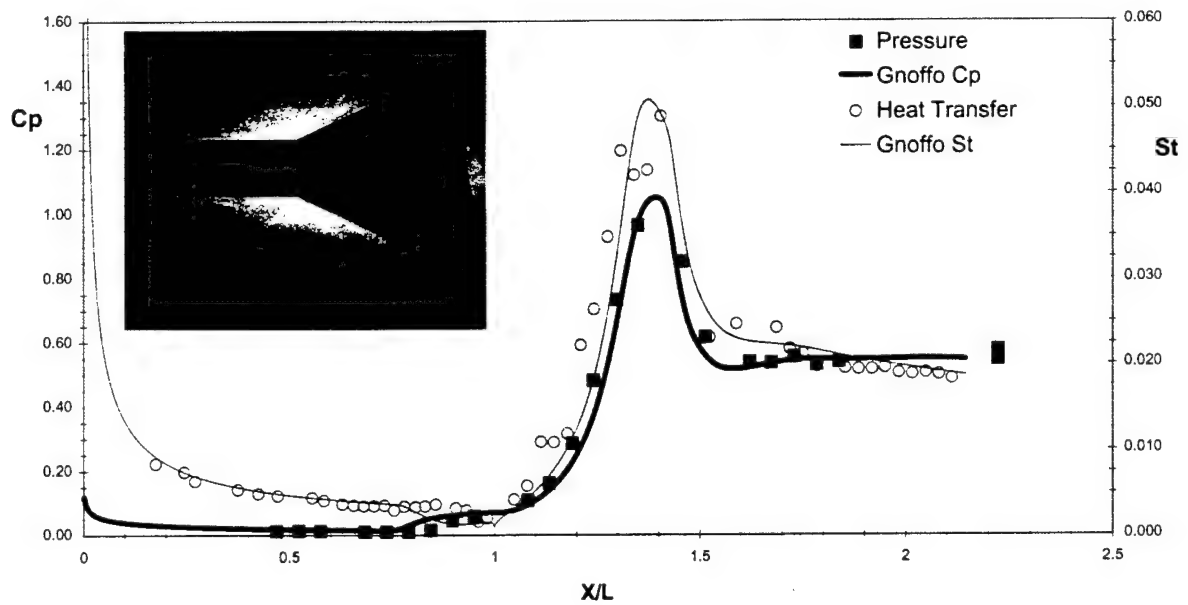
**Figure 62   Pressure, Heat Transfer and Schlieren Photo
Run 11 (M = 12.23, Re#/ft = 6.25E+04) : Gnoffo**
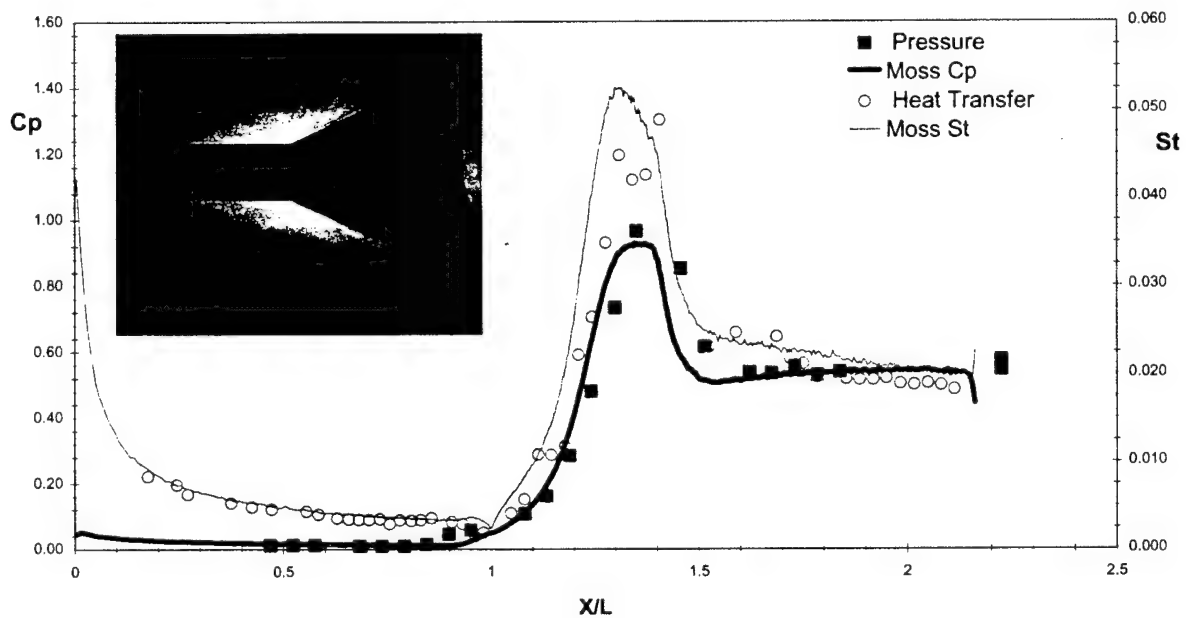
**Figure 63   Pressure, Heat Transfer and Schlieren Photo
Run 11 (M = 12.23, Re#/ft = 6.25E+04) : Moss**
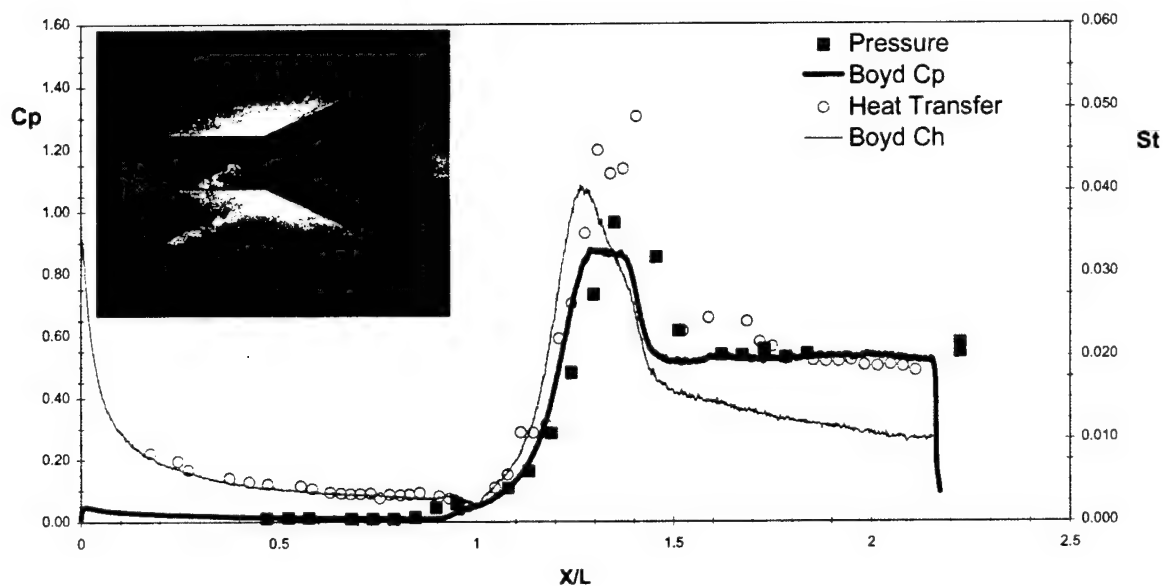
**Figure 64   Pressure, Heat Transfer and Schlieren Photo
Run 11 (M = 12.23, Re#/ft = 6.25E+04) : Boyd**
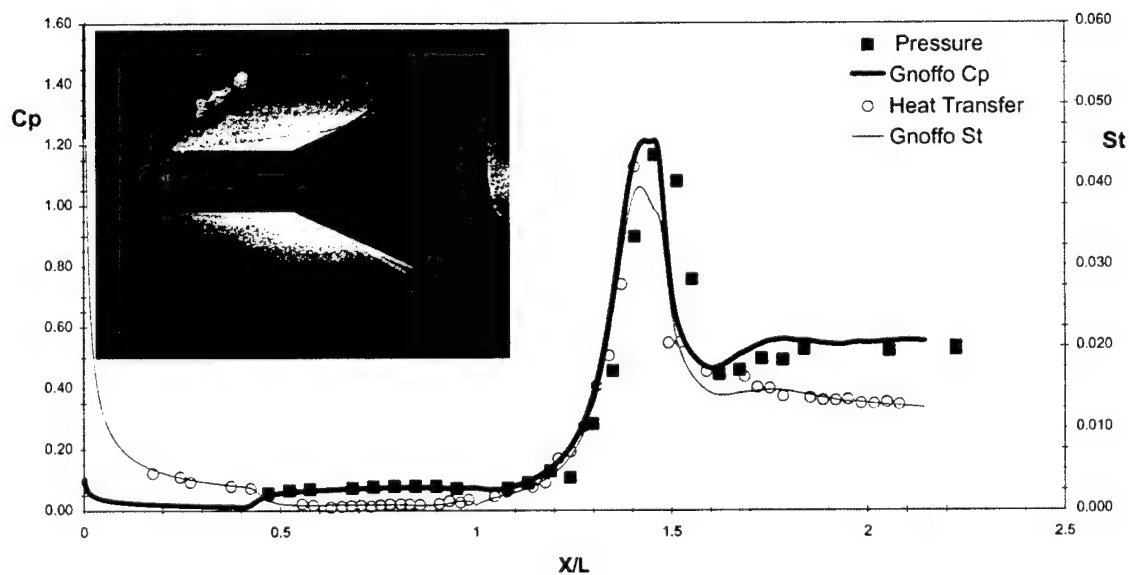
**Figure 65   Pressure, Heat Transfer and Schlieren Photo
Run 8 (M = 12.46, Re#/ft = 14.6E+04) : Gnoffo**

**Figure 66   Hollow Cylinder with Short Flare – Run 18
Composite picture showing Schileren image and
Density contour computed by Gnoffo**
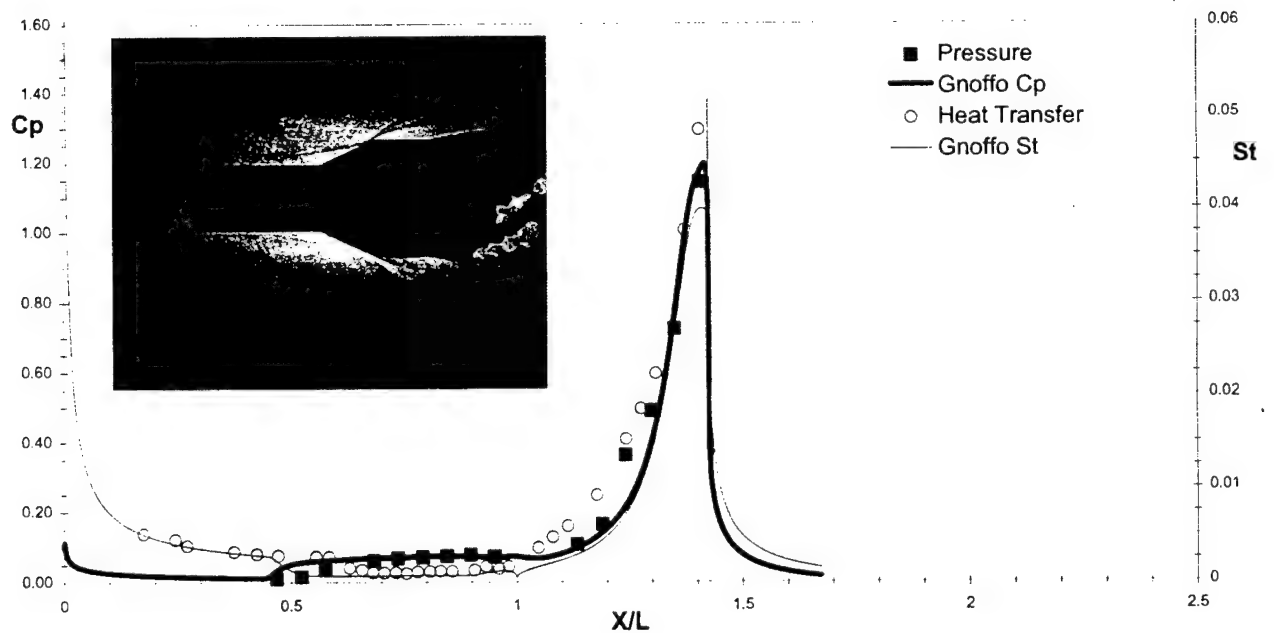
**Figure 67   Pressure and Heat Transfer
Run 18 (M = 12.44, Re#/ft = 14.3E+04) : Gnoffo**

Pressure, Heat Transfer and Schlieren Photo
Run 19 (M = 12.42, Re#/ft = 11E+04) : Moss
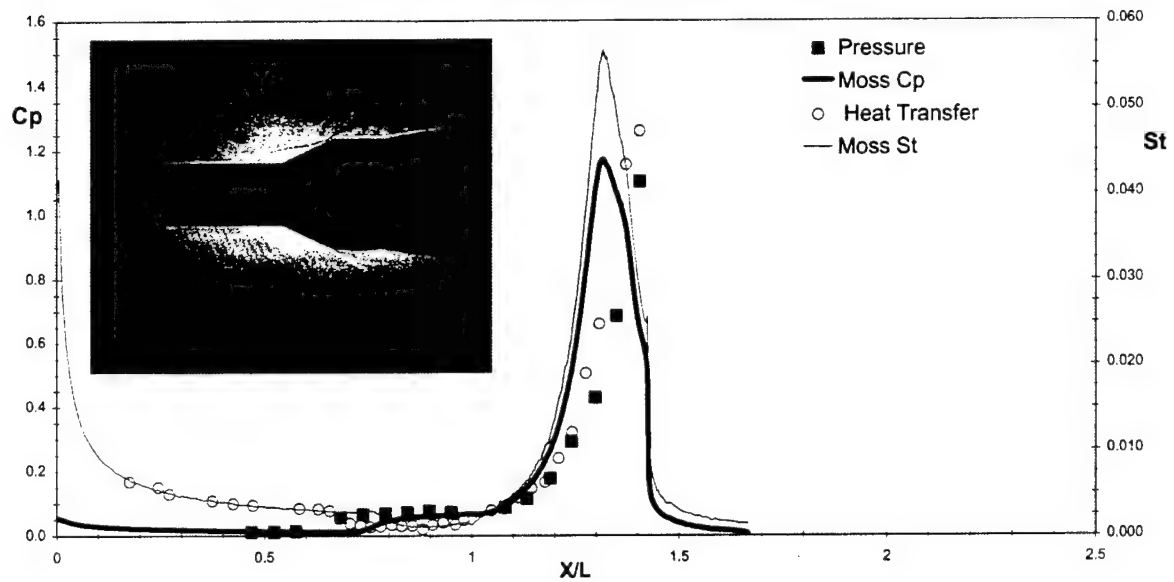
Figure 68   Pressure and Heat Transfer
Run 19 (M = 12.42, Re#/ft = 11.0E+04) : Moss
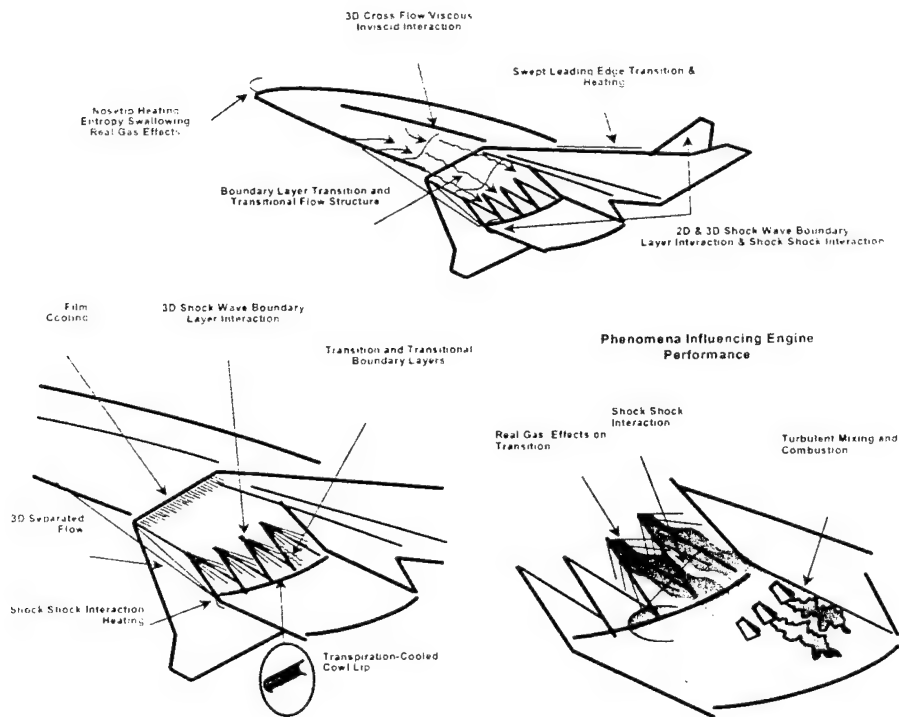
Figure 69 Key Phenomena Influencing Scramjet Performance

NASA HYPER-X

DARPA - ARRMD
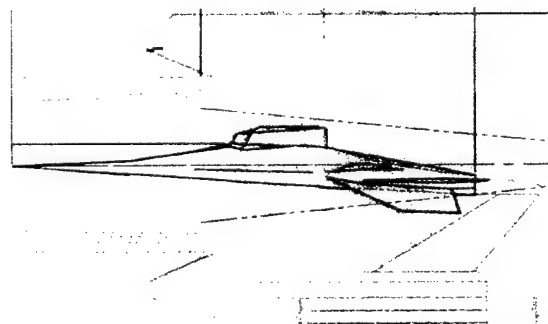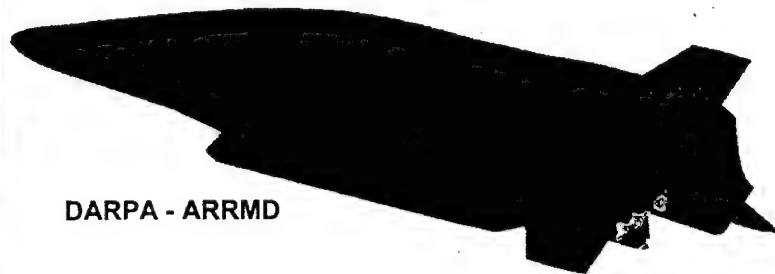
Full Scale HYPER-X in LENS One
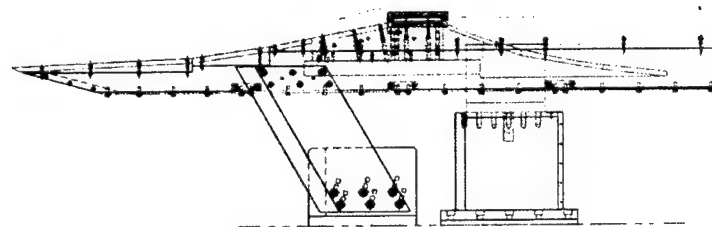
Generic Scramjet HYPER –X / ARRMD

Figure 70 Scramjet Studies in LENS I and II Facilities

Figure 71   NASP Studies at Calspan

SHOCK/SHOCK INTERACTION STUDIES
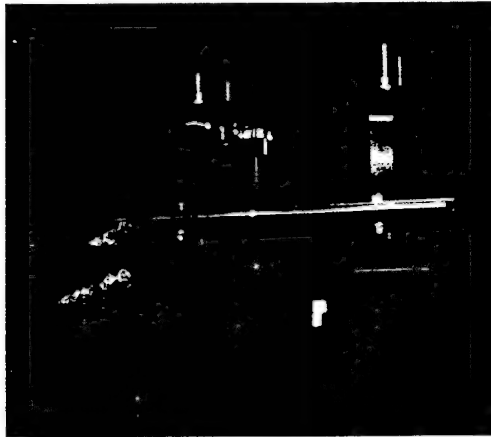
TRANSITION ON COMPRESSION
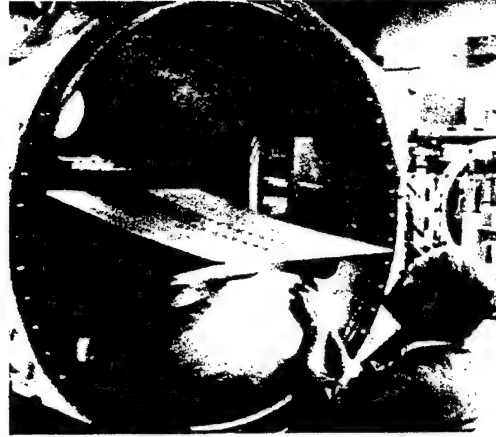
SHOCK INTERACTION ON FILM-COOLED SURFACE
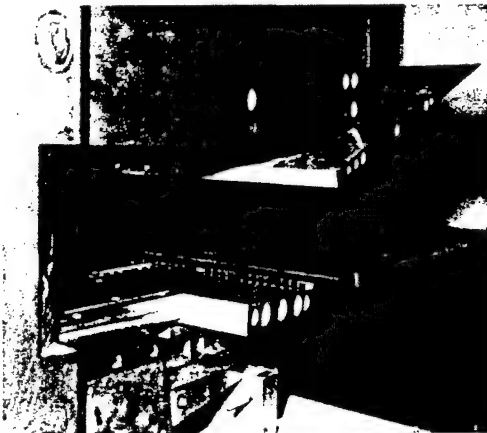
SHOCK INTERACTION ON TRANSPIRATION-COOLED SURFACE
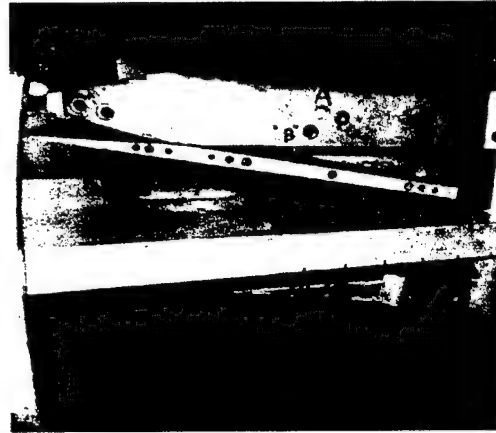
ATTACHMENT LINE TRANSITION
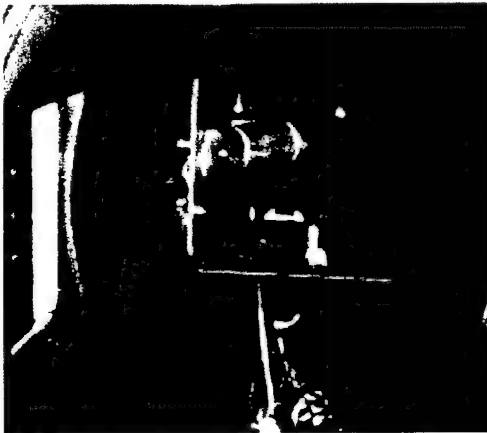
RELAMINARIZATION IN EXPANSION FLOW
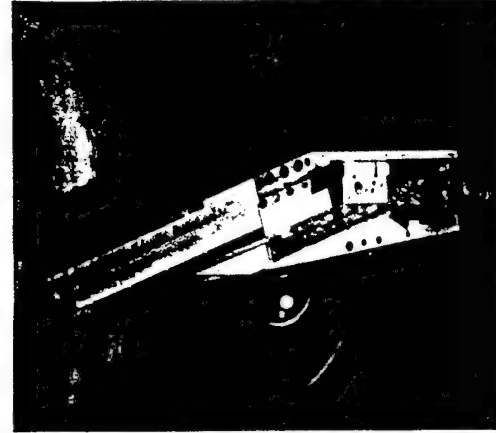
Figure 72 Studies of Fundamental Flow Phenomena for CFD Prediction/Validation for NASP Program

CONTOURED, PARALLEL–FLOW
FACILITY NOZZLE

SHOCK TUNNEL
DRIVEN TUBE

NOZZLE

COMBUSTOR

SHOCK

T_O

U_∞

T_a

P_O

P_a

INLET
RAMP

RESERVOIR
CONDITIONS

NOZZLE EXIT
PLANE CONDITIONS

COMBUSTOR
INLET CONDITIONS
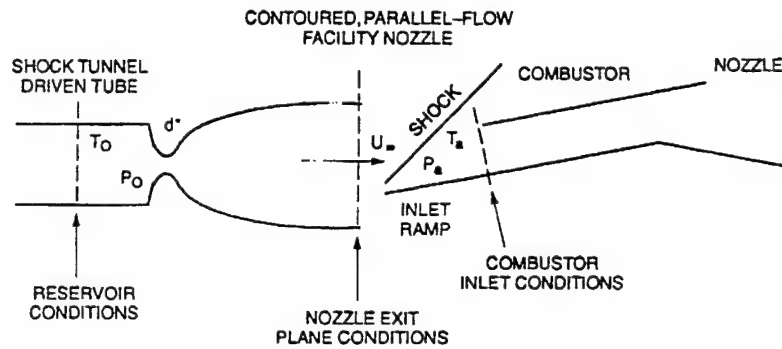
Figure 73 Flow Configuration for NASP Engine Testing
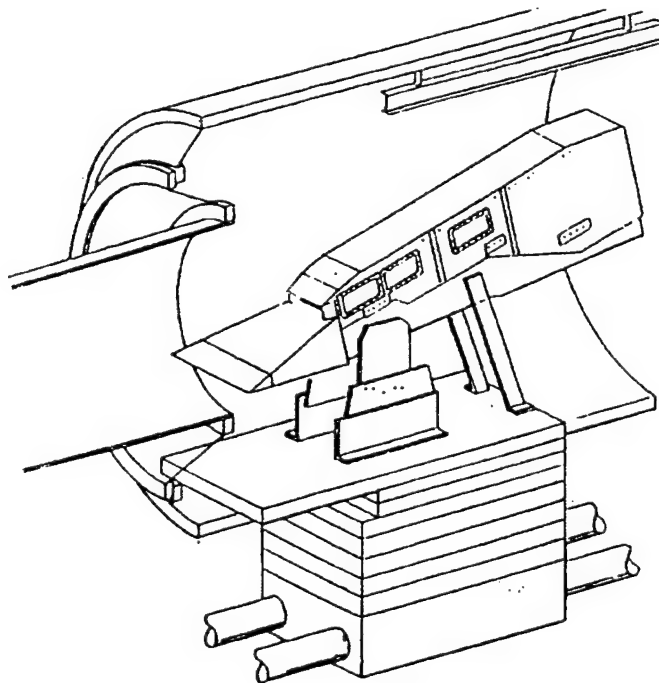
Figure 74 Schematic of the Combustor Model Mounted in the LENS Facility

68
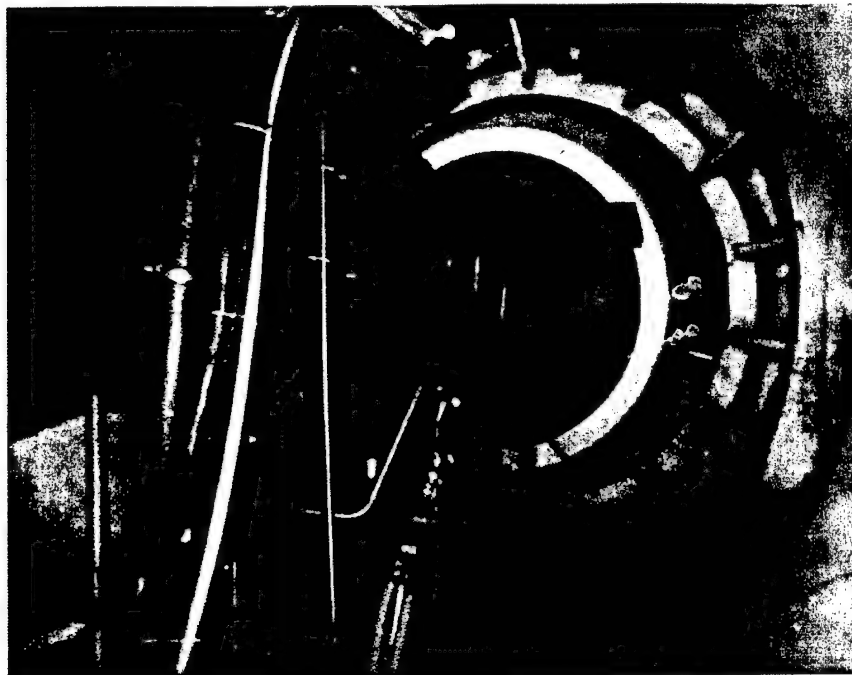
Figure 75   NASP Engine Installed in LENS Leg I Facility

Legend
△ Thin Film Heat Flux
□ Pressure (PCB)
◇ Coax T.C.

Cowl

Body
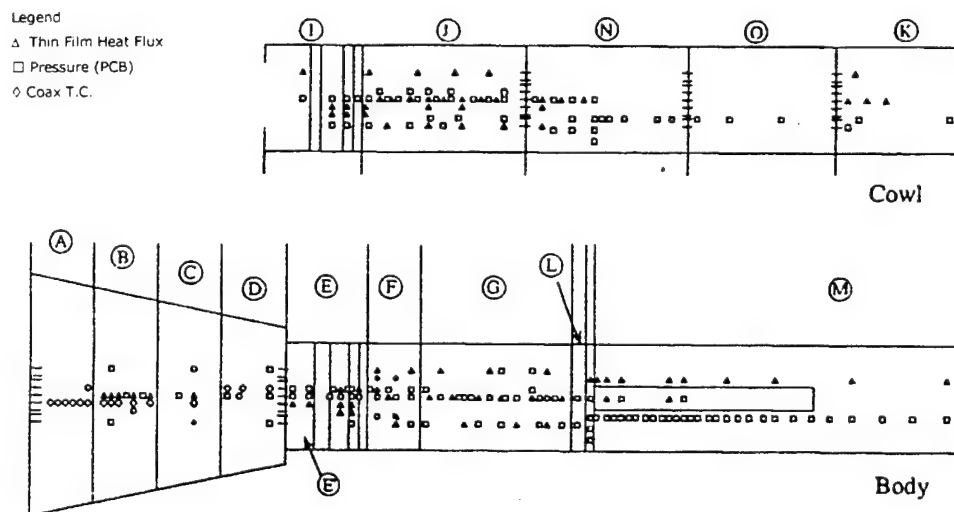
Figure 76 Instrumentation on NASP Configuration
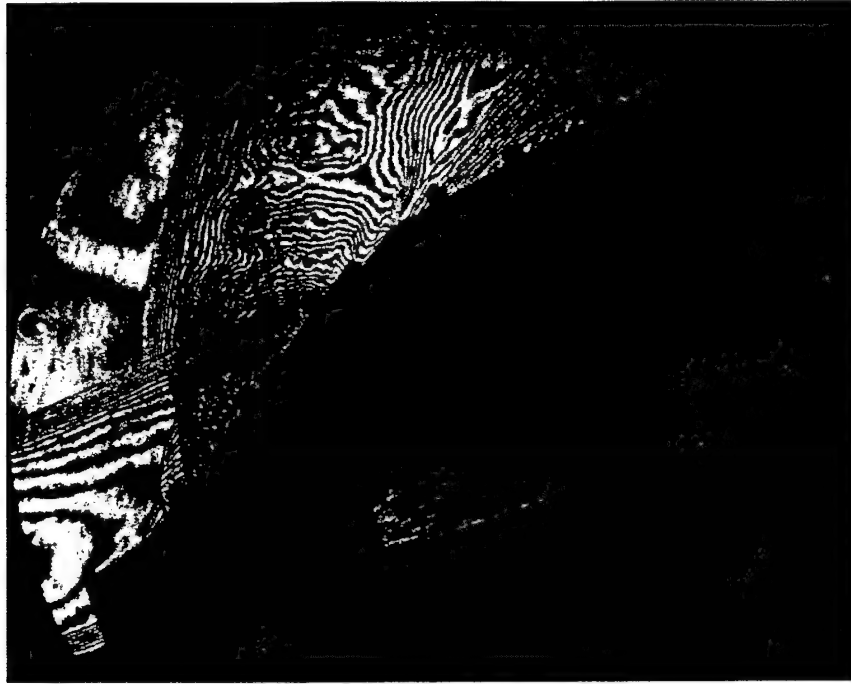
Figure 77 Holographic Interferogram of Supersonic Combustor Flowfield

(b) Heat Transfer
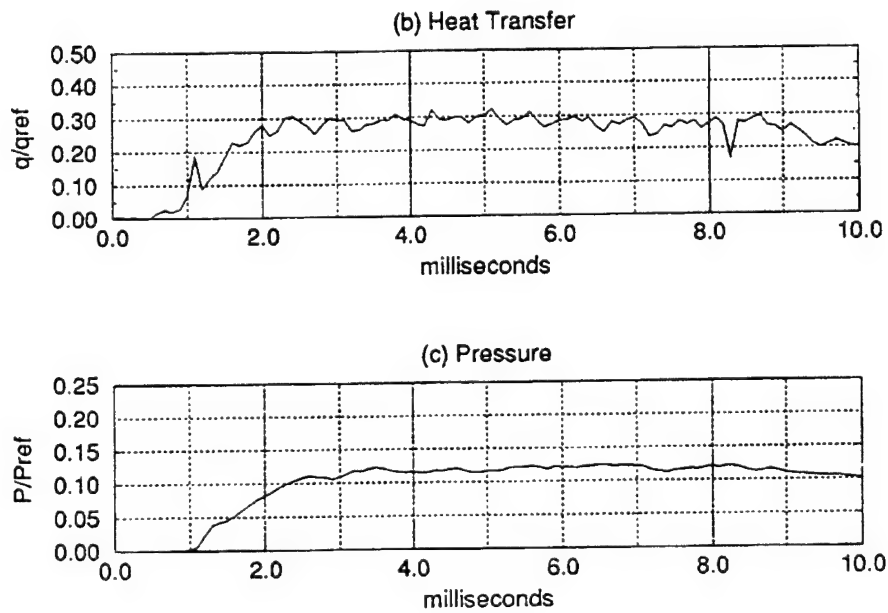
(c) Pressure

Figure 78 Typical Time Histories of Heat Transfer and Pressure for the Mach 12 Combustor Tests

70

Combustor Wall Pressure Profiles

Combustor
Wall Heat
Transfer
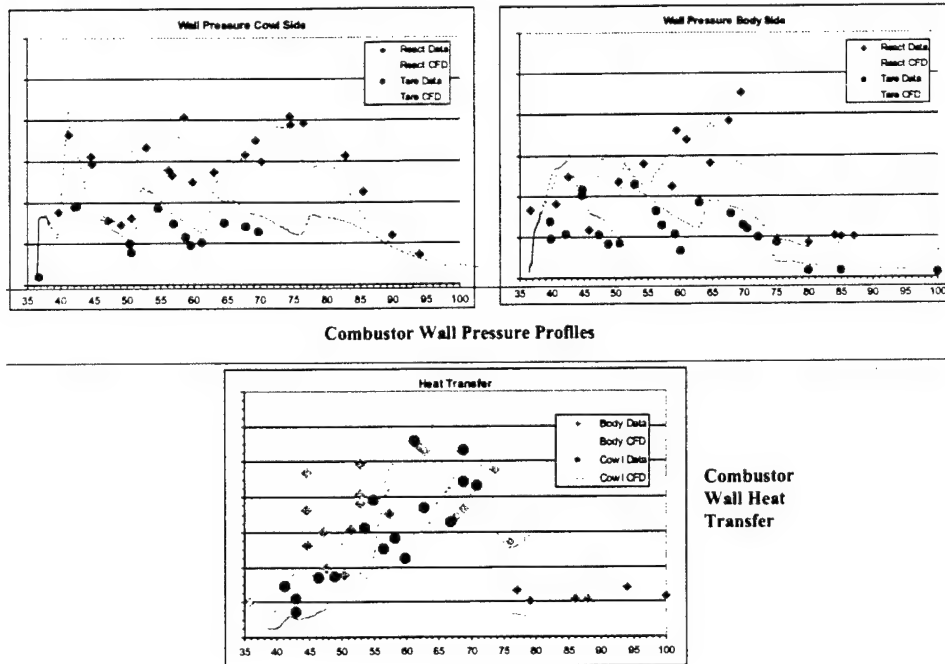
*Dash, S.M. et al, AIAA Paper 2000-0940.

Figure 79 Comparison between Predictions and Measurements of the Distribution of Heat Transfer and Pressure in the Combustor
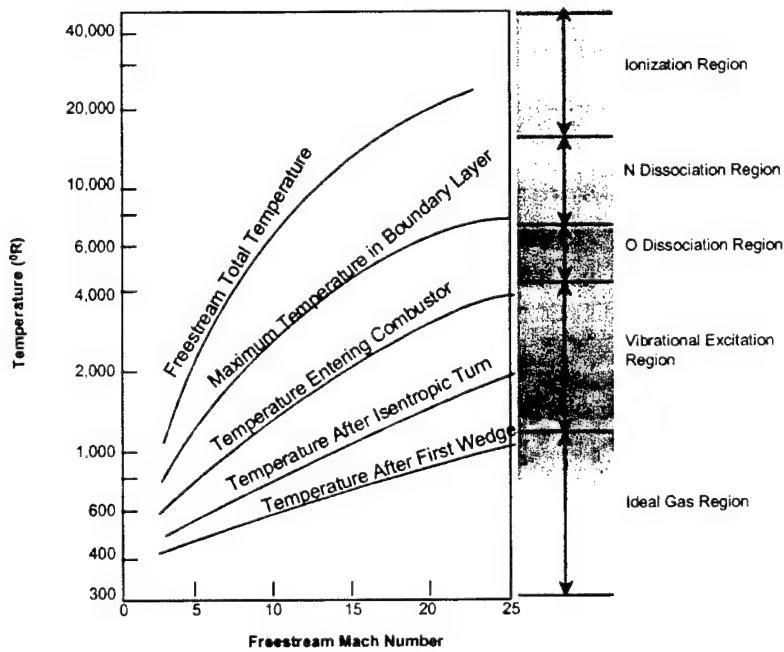
Figure 80 Typical Temperature in Air-Breathing Engine Inlets
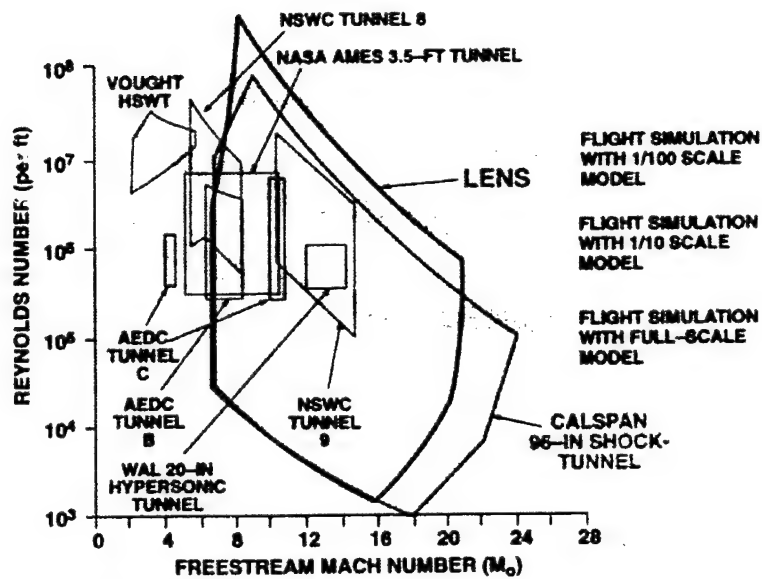
Figure 81 Mach Number/Reynolds Number Performance of LENS I Facility
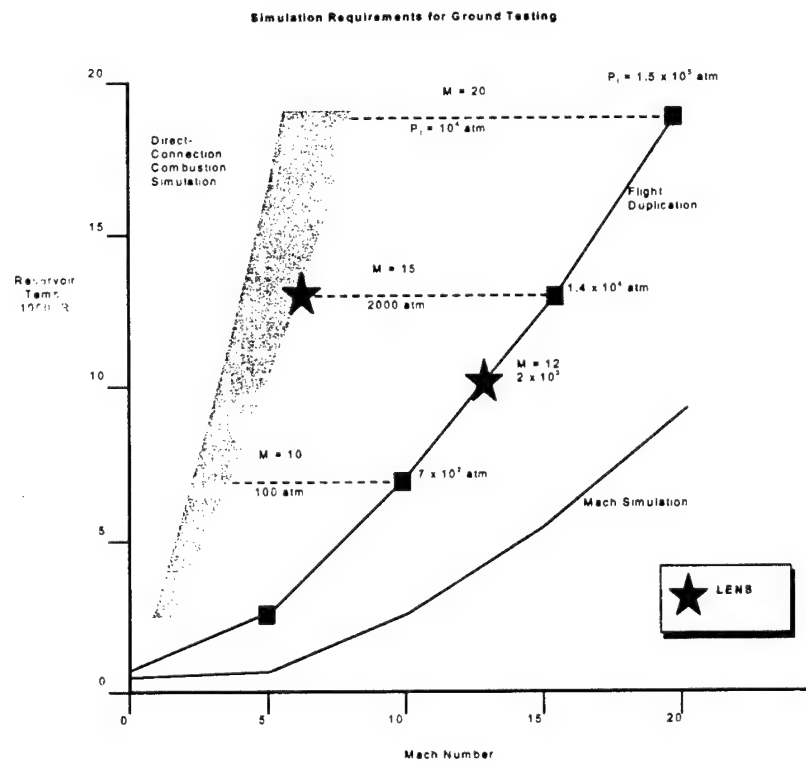
Figure 82 Capabilities of LENS Facility to Perform Combustor Studies at Mach Numbers from 8 to 15
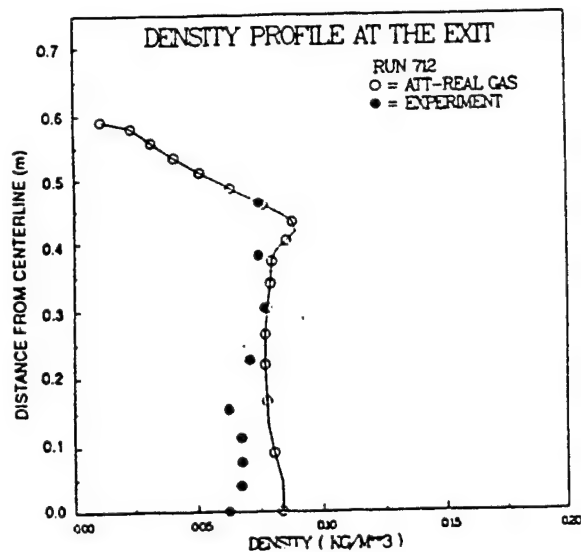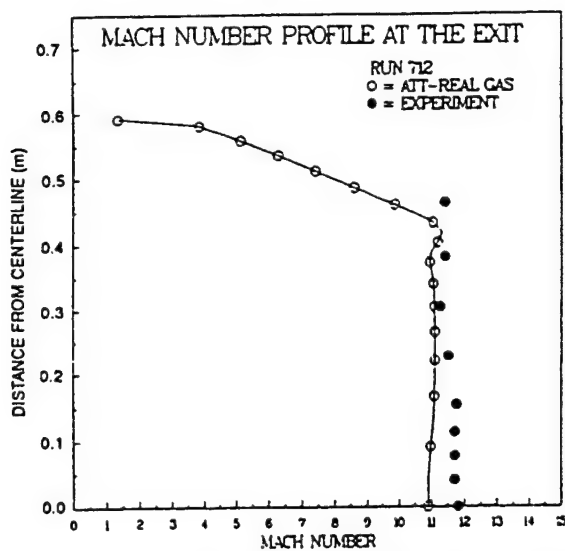
Figure 83   Exit Mach Number and Density Profiles of D-Nozzle

(c) D-Nozzle Cross Velocity

(f) D-Nozzle Exit Density
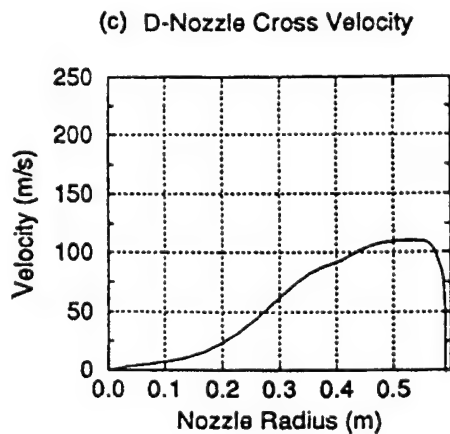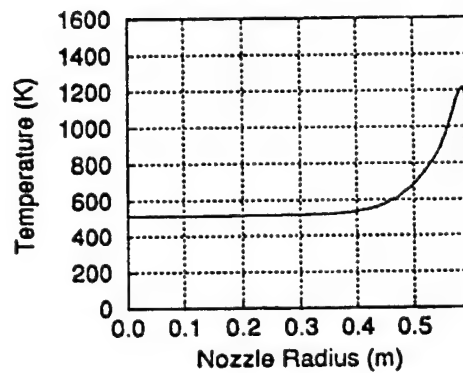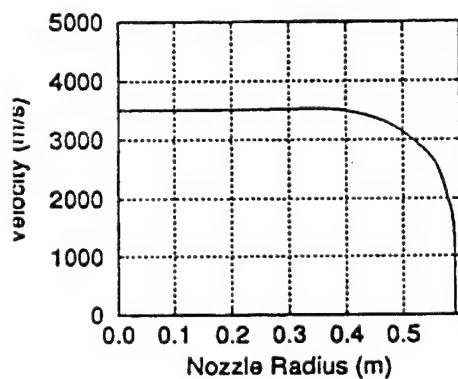
Figure 84   Nominal Freestream Conditions for the Mach 12 Combustion Tests

73
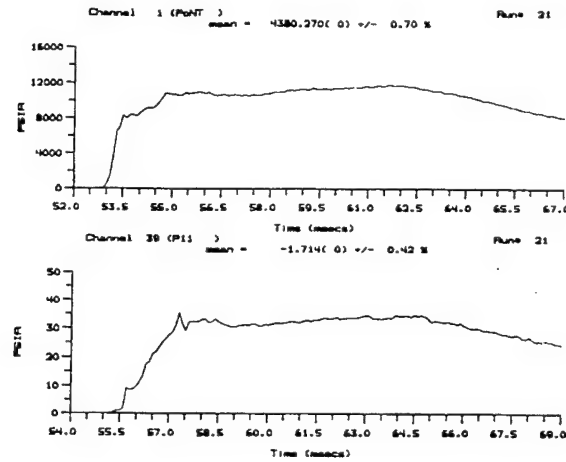
Figure 85 Reservoir and Test Section Pressure Measurements at Mach 8
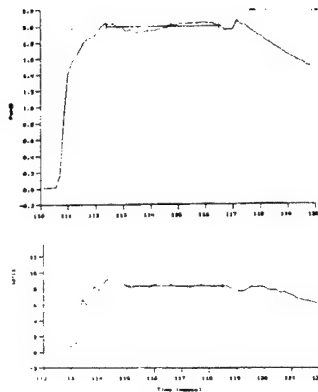
Figure 86 Reservoir and Static Pressure Measurements in LENS Leg I for 10,000 ft/sec at Mach 10
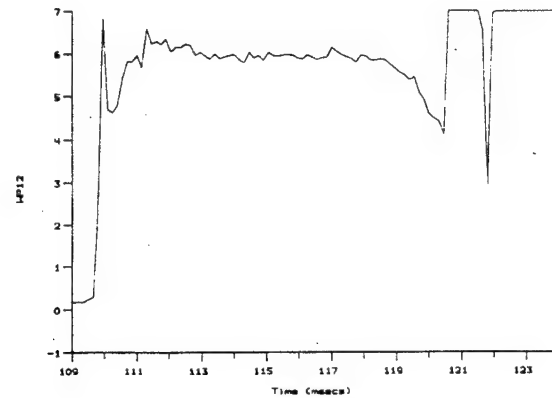
Figure 87   Static Pressure Measurements in LENS Leg I for 12,000 ft/sec at Mach 12
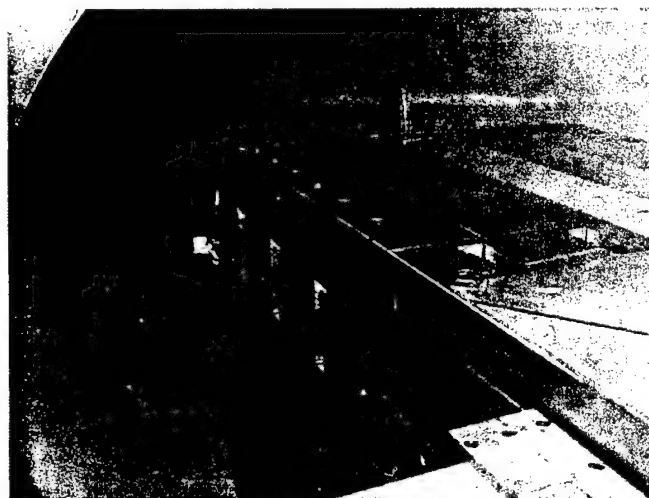
Figure 88 Model Configuration Used in Studies

74
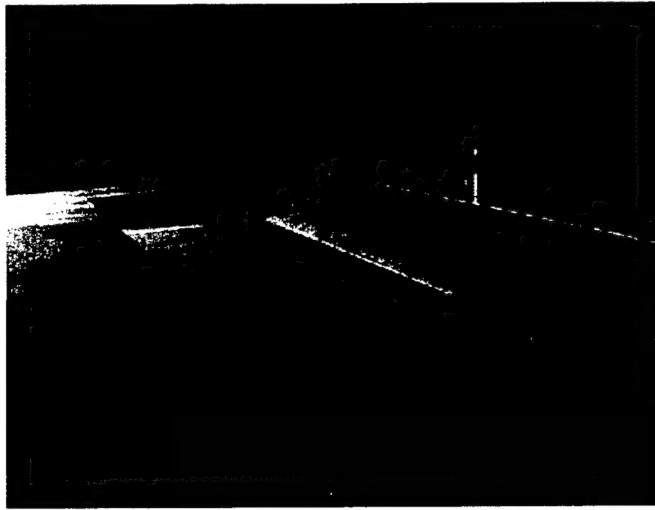
Figure 89 Cavity Configuration with Flush-Mounted Wall Injectors
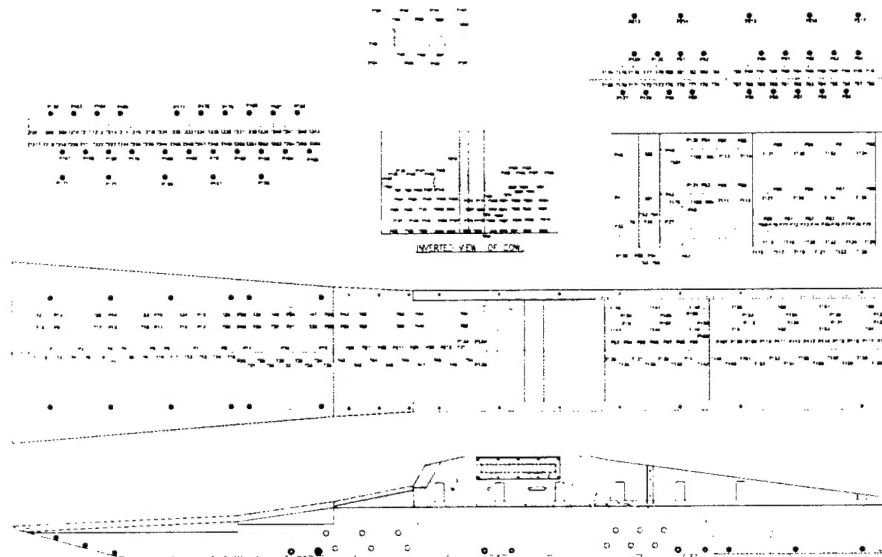
Figure 90 Instrumentation Layout on Generic Scramjet Engine

75
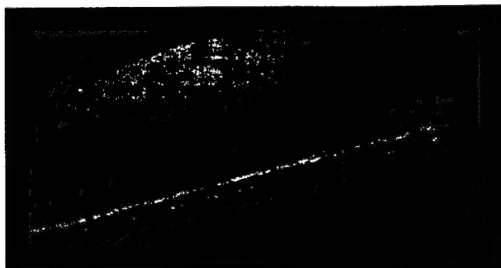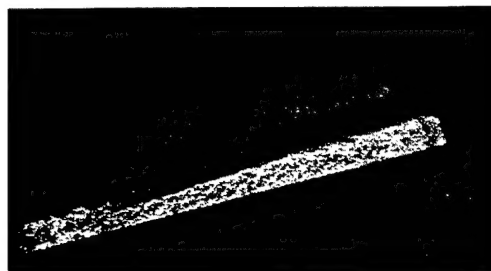
(a) Inlet Ramp Without Trips   *(b) Inlet Ramp With Trips*

Figure 91 Schlieren Photograph of Flow Into Scramjet Inlet
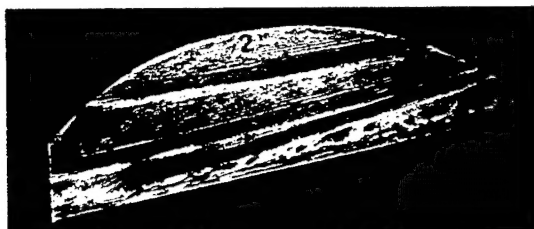
(a) Inlet Ramp Without Trips   *(b) Inlet Ramp With Trips*

Figure 92 Pulsed Holograph of Flow Into Scramjet Inlet
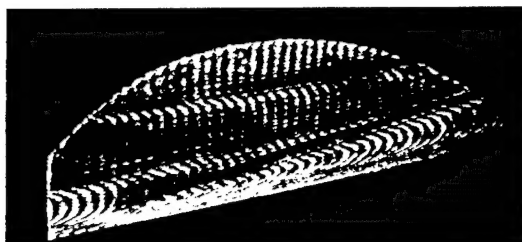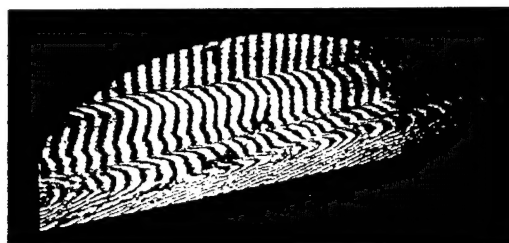
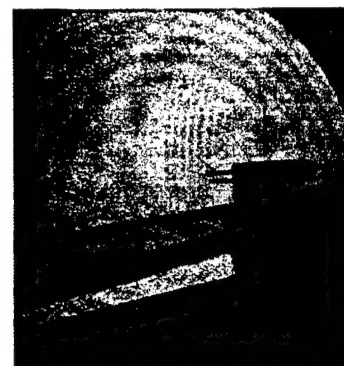

(a) Inlet Ramp Without Trips   *(b) Inlet Ramp With Trips*

Figure 93   Infinite Fringe Holograph of Flow Into Scramjet Inlet

(a) Run 53, q = 1,000 psf (no trips)   (b) Run 50, q = 1,350 psf (no trips)   (c) Run 52, q = 1,350 psf (Trips) (Note the increased thickness of boundary layer)

Figure 94 Schlieren Photographs for Inlet Profile Characterization

76
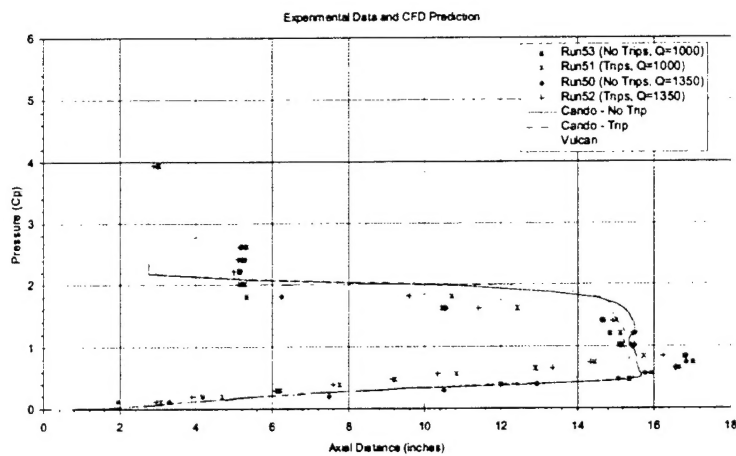
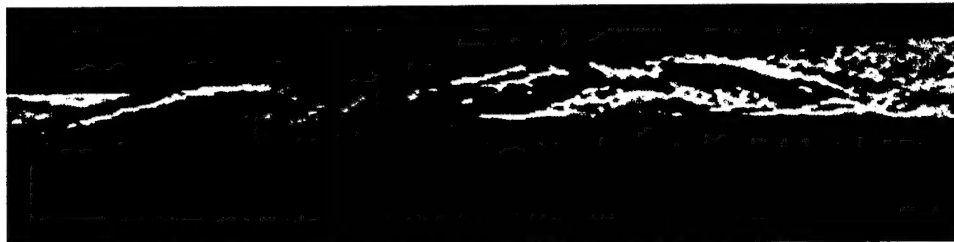**Figure 95 Comparison Between Navier-Stokes CFD Calculations and Experimental Data**

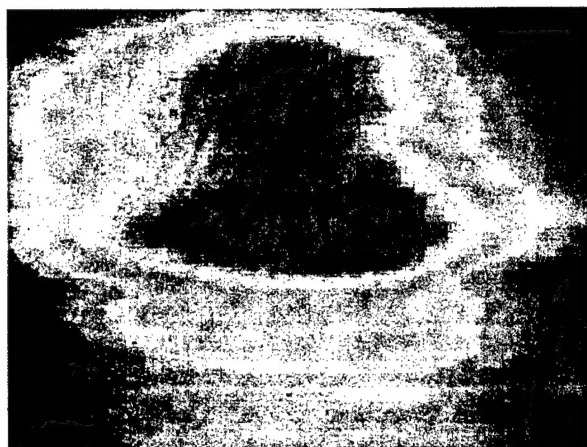**Figure 96 Schlieren Photograph of Flow Through Engine**

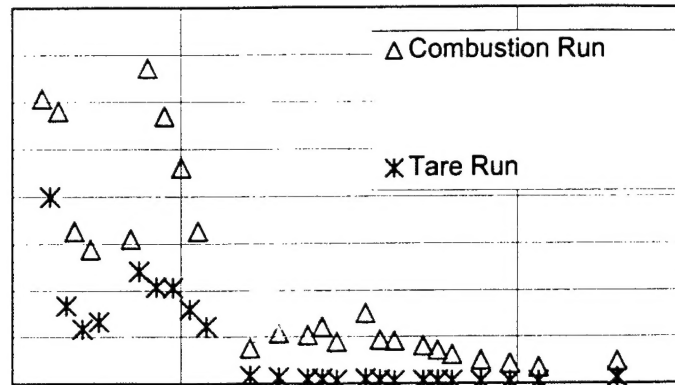**Figure 97   Infrared Photograph of Burning Around Injector**

77

Figure 98 Typical Distribution of Heat Transfer for the Combustion and Tare Runs through the Scramjet Engine
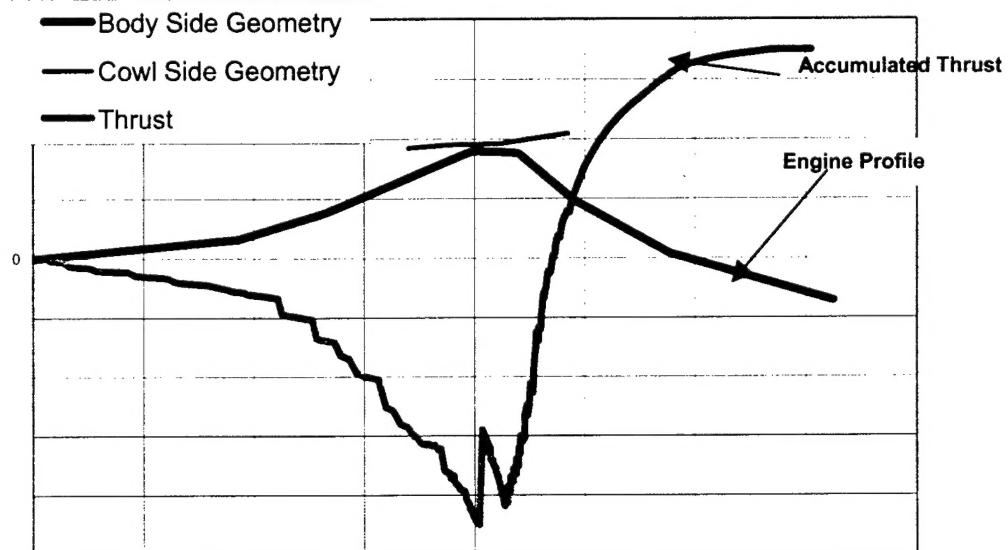

Figure 99 Pressure, Skin Friction Drag and Thrust for Scramjet Engine

78